GEORG-AUGUST-UNIVERSITÄT GÖTTINGEN

II. Physikalisches Institut

Performance Study of a Diamond Pixel Detector Prototype for Future ATLAS Upgrades Using Beam Test Data

von

Florian Köhler

Based on the upcoming luminosity upgrade of the LHC the innermost detector layer of the ATLAS experiment will have to withstand very high radiation fluences. For this harsh environment new sensor technologies are developed. Next to silicon concepts (planar pixels and 3D pixels) diamond is a favoured sensor candidate due to excellent intrinsic material properties. In this diploma thesis the performance of a single crystal diamond tracking detector is studied in beam test measurements. In addition to the study of resolution, cluster size, charge sharing, efficiency, noise and charge collection distance an extensive split-cluster analysis will resolve known inconsistencies in the charge spectra. With a special focus on radiation hardness testbeam results at different radiation fluences are compared.

GEORG-AUGUST-UNIVERSITÄT GÖTTINGEN

II. Physikalisches Institut

Performance Study of a Diamond Pixel Detector Prototype for Future ATLAS Upgrades Using Beam Test Data

von

Florian Köhler

Contents

Outline

One of the most exciting challenges of humankind is the understanding of nature at a fundamental level. In the last century physicists have started to develop an extremely successful theory of the fundamental interaction of elementary particles, which has been confirmed in a series of experiments to unprecedented precision. To strengthen and extend this standard model of particle physics a proton-proton collider, the Large Hadron Collider (LHC), has been built by the European Organisation for Nuclear Research (CERN).
The Standard Model and its recent challenges will be summarised in Chapter 1. In this context the LHC and its largest experiment, ATLAS (A Toroidal LHC ApparatuS), are briefly introduced.

In the next years the collision rate will be maximised at the LHC to even further increase the sensitivity to rare processes in the standard model or in new physics. After a final luminosity upgrade the ATLAS experiment will have to withstand very high radiation fluences[1] of up to 10^{16} n_{eq}/cm^2. For this reason, the present inner detector layers will have to be replaced by new detectors, which resist the harsh environment.
In Chapter 2 the current ATLAS upgrade plans are stated. The three most promising sensor developments (planar silicon, 3D silicon, planar diamond) are motivated in short.

In this diploma thesis a *single crystal Chemical Vapour Deposited* (scCVD) diamond detector prototype is studied, which is one of the very promising new sensor concepts. In contrast to *polycrystalline Chemical Vapour Deposited* (pCVD) diamonds, which have been studied in the last two decades by the RD42 collaboration at CERN, an scCVD diamond provides a homogeneous crystal lattice without any grain boundaries. As a result of the low intrinsic concentration of material defects scCVD diamonds are particularly qualified for tracking detectors in a high luminosity environment.
In Chapter 3 the electronic properties of diamond as well as the detection principle of a diamond tracking detector are summarised.

In Chapter 4 the studied scCVD diamond tracking detector CD181 is introduced, which is the first scCVD diamond tracking detector using ATLAS readout electronics. Next to its general design a special focus is placed on the description of the electronic readout.

In this diploma thesis data sets from several testbeam periods are analysed, which have been recorded in 2006-2008. During this period CD181 was irradiated twice with 24 GeV/c protons at the CERN PS.
In Chapter 5 the basic concept of a testbeam analysis is motivated. After introducing the Bonn-ATLAS-Telescope (BAT) the complete analysis chain is explained in detail.

Subsequently, the results of the testbeam analysis are presented in Chapter 6. By compar-

---

[1]Radiation damage in general is parametrised using 1MeV-neutron equivalent fluences, which are obtained by convoluting predicted energy spectra with displacement-damage functions [1].

ing the spatial resolutions, cluster sizes, charge sharing, charge spectra and charge collection distances of testbeam periods at different irradiation fluences a special focus is placed on the analysis of radiation hardness.
Furthermore an extensive split-cluster analysis resolves some known inconsistencies especially in the charge spectra.

Finally in Chapter 7 the most important results are summarised. Some particular characteristics are interpreted in a bigger context. In the end a short outlook is given.

1. LHC and ATLAS

In the beginning of this thesis a short introduction to particle physics and its recent challenges is given. Subsequently the Large Hadron Collider and the ATLAS experiment are briefly explained to clarify the current detector assembly. In the next Chapter the possible role of a diamond tracking detector in future ATLAS upgrades is presented.

1.1. Physical Motivations for Collider Experiments: the Standard Model and Beyond

The idea of the *Standard Model of Particle Physics* (SM) is the reduction of all observed processes in our universe to some fundamental processes between elementary particles (point-like objects without substructures) interacting via forces which are transmitted by particles. In our present standard model matter is formed by spin 1/2 particles, which are called fermions, and the fundamental forces (excluding gravity) are represented by spin 1 particles which are called bosons.

In general fermions are divided into six quarks and six leptons which are ordered in three generations. Most of the matter in our present universe can be described by three particles of the first

Figure 1.1.: Summary table of the standard model of particle physics; numbers come from [2]. The Higgs boson, which is essential for mass generation, is the only particle which has not been discovered yet.

generation: electrons as well as up and down quarks, which constitute the effective ingredients

of protons and neutrons. Particles of the second and third generation are much heavier and therefore unstable. Today these generations can be produced and exist for short times, almost exclusively in collider or fixed target experiments[1].

Each fermionic particle has a corresponding antiparticle with opposite electric charge: $\pm 2/3$ or $\mp 1/3$ for quarks and ± 1 for electrons, muons and taus whereas neutrinos and antineutrinos have zero charge. In addition quarks carry colour charge: red, green or blue.

Embedding special relativity and quantum mechanics, the fundamental interactions in the SM are described by quantum field theories (QFT) which are invariant under local gauge transformations[2]. The following fundamental forces are included in the SM:

1. **electromagnetic force:** This force is mediated by photons which couple to electrically charged particles. Since the photons are massless the force has an unlimited range. The corresponding QFT is called Quantum Electrodynamics (QED).

2. **weak force:** Mediated by massive Z and $W^{\pm}$ bosons, the weak force acts in a limited range between all fermions.

3. **strong force:** Eight massless coloured gluons couple as force carriers to colour charged fermions, the quarks. Also denoted as confinement, quarks exclusively exist in compound states (hadrons) consisting of three quarks (baryons) or two quarks (mesons). In addition gluons are responsible for the nuclear binding and some nuclear reactions. The corresponding QFT is called Quantum Chromodynamics (QCD).

The electromagnetic and weak force have been unified in a $SU(2) \times U(1)$ symmetry group which is the basis of the electroweak theory also called Glashow-Weinberg-Salam (GWS) theory [3, 4, 5]. Furthermore the strong force is described by an $SU(3)$ symmetry group [6, 7, 8].

Up to now, gravity is excluded from the SM since no complete quantum field theory has been developed yet, and collider experiments have not been sensitive to this extremely weak but long-distance force.

Despite the various successful tests of the SM predictions, the assumed mechanism, which generates the masses of all massive particles in the SM, has not been demonstrated yet.

For the mass generation in the SM a complex mechanism is required as canonical mass terms violate the fundamental local gauge symmetries. Originally dedicated to the massive gauge bosons $(Z, W^{\pm})$, the *Higgs-Mechanism*[3] has been developed to generate the masses of these bosons by electroweak spontaneous symmetry breaking [9]. For this purpose an additional scalar particle, the Higgs boson, is required. This specific mechanism has been extended to all other massive particles of the standard model.

Motivated by mathematical and physical elegance and simplicity (hierarchy problem[4], unification[5], spin symmetry), an attractive candidate for the extension of the standard model is

---

[1] Cosmic rays and other phenomena in astrophysics are neglected in this case.

[2] Local gauge symmetry denotes the invariance of the Lagrange density under local phase transformations. It is essential for the renormalisation of quantum field theories.

[3] The mechanism is named after its major inventor Peter Higgs.

[4] The hierarchy problem is caused by the huge difference between the assumed mass-scale of the Higgs boson of circa 100 GeV and the mass-scale of gravity (Planck scale) of circa 10^{19} GeV. Since the quantum corrections for the Higgs boson mass are quadratically divergent, the corrections are huge and require an unnatural fine-tuning to obtain the expected Higgs boson mass if the cutoff parameter is comparable to the Planck-scale. With SUSY, the quantum corrections naturally cancel.

[5] With SUSY, it is possible that the coupling constants of the SM meet at 10^{16} GeV. So the three forces of the SM could be unified at this energy scale.

broken *Supersymmetry* (SUSY) [10]. Under this transformation each SM fermion receives an identical partner, but with spin 1, while each SM boson obtains an identical partner, but with spin 1/2. This symmetry has to be broken with respect to the particle masses as the supersymmetric partners have not been discovered in the accessible mass ranges of the operating collider experiments. In addition, some SUSY models predict weakly interacting massive particles (WIMPs), which are good candidates for dark matter[6].

Primarily motivated by the search for the Higgs-Mechanism and SUSY but also by the search for other SM extensions and some more precise measurements of the SM, the Large Hadron Collider (LHC) has been built to discover new physics in a promising energy range (the TeV scale), which has not been accessible in any collider experiment before.

1.2. The Large Hadron Collider (LHC)

The Large Hadron Collider (LHC) is a proton-proton (Pb-Pb)[7] collider at the European Organisation for Nuclear Research (CERN) near Geneva. The complete machine is placed in a 27 km ringlike tunnel, 100 m below the surface crossing the border between Switzerland and France. Up to 2808 bunches of protons are grouped in two opposite circulating beams. The bunches are accelerated, so that each of the 10^{11} protons per bunch has an energy of 7 TeV. At four points
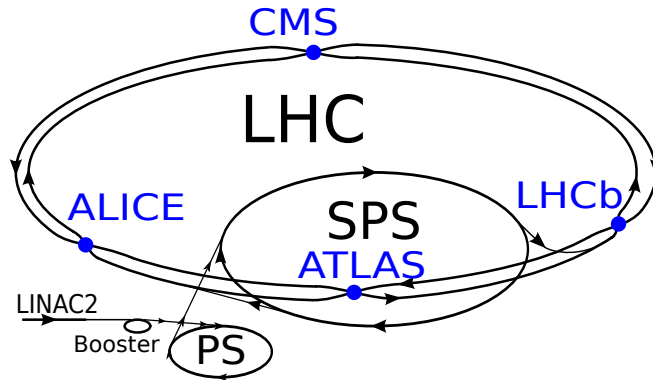
Figure 1.2.: Illustration of the Large Hadron Collider with its four experiments: ATLAS, CMS, ALICE, LHCb and its pre-accelerators: LINAC2, Booster, PS and SPS

in the tunnel the two beams intersect, and protons collide with a centre-of-mass energy up to 14 TeV.

The proton-proton collision rate is proportional to the proton-proton inelastic cross section σ_{inel}. The proportionality constant is called *instantaneous luminosity*. At collider experiments it is defined as:

$$\mathcal{L} := \frac{\mu n_b f_r}{\sigma_{inel}} \tag{1.1}$$

where f_r is the revolution frequency of the bunches, n_b the number of bunches per beam and μ the number of inelastic interactions per bunch crossing (BC). The integrated luminosity is

---

[6]In the last two decades it has been discovered in cosmology that the universe is made up of 74% dark energy, 22% dark matter and only 4% ordinary matter. Dark matter as well as dark energy has to be integrated in the SM [11].

[7]Alternatively the LHC can accelerate lead ions to energies in the range of 1000 TeV.

defined as: $\mathcal{L}_{int} := \int \mathcal{L}dt$. The LHC is designed for a peak luminosity[8] of 10^{34} cm^{-2}s^{-1}. With a bunch crossing rate of up to 40 MHz and circa 25 interactions per bunch crossing circa 10^9 interactions per second are expected.

As illustrated in Figure 1.2 the four collision points of the LHC are surrounded by huge experiments, respectively: ATLAS (A Toroidal LHC ApparatuS) and CMS (Compact Muon Solenoid) are multipurpose experiments. LHCb is dedicated to the analysis of b-physics with a special focus placed on CP-violation. With ALICE the quark-gluon plasma is explored which is produced in heavy ion collisions (lead ions).

From March 2010 until November 2010 circa 45 pb^{-1} data have been recorded with ATLAS at a centre-of-mass energy (E_{CM}) of 7 TeV and a peak luminosity of up to 2.1×10^{32} cm^{-2}s^{-1}.

1.3. A Toroidal LHC Apparatus (ATLAS)

Since the analysed diamond tracking detector is developed for future ATLAS upgrades, this multipurpose experiment is summarised in short [12, 13]. With a length of 44 m and a height of 25 m ATLAS is the largest experiment at the LHC. It covers the full physics potential of the LHC, e.g. the search for the Higgs-Mechanism, SUSY, heavy W and Z like bosons, extensive top quark studies and CP-violation in B-decays.

Illustrated in Figure 1.3 the experiment has a typical onion-shell structure: An inner detector (ID) consisting of a pixel detector, a silicon strip tracker (SCT) and a transition radiation straw tube tracker (TRT) provide precise measurements of the tracks of charged particles which are produced in the proton-proton collisions. Primary but also secondary vertices for b-tagging can be reconstructed. A solenoidal magnet generates a 2 T axial field which penetrates the complete inner detector and enables the determination of the momentum by measuring the track curvature.

The ID is surrounded by an electromagnetic and a hadronic calorimeter measuring the energy of electrons and photons as well as jets by the complete stopping of the particles.

The outer layers of the ATLAS experiment constitute the muon spectrometer where the momenta of the muons are determined once more via a huge toroidal magnetic field.

Limited by the storage capacities, the original event rate of about 1 GHz has to be reduced to a storage rate of 200 Hz by selecting only physically interesting events. This enormous data reduction is achieved by a three level trigger system.

---

[8]Peak luminosity corresponds to the maximal instantaneous luminosity (in the beginning of each run).
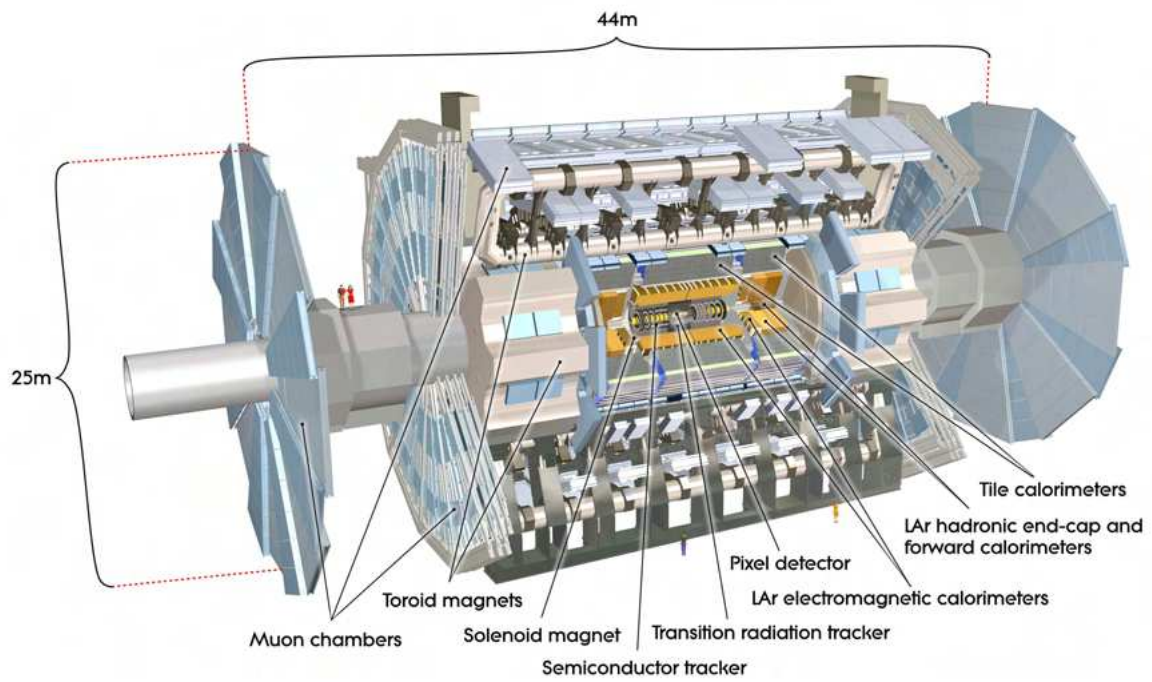
Figure 1.3.: Schematic view of ATLAS illustrating the various subdetectors and magnets [13].

2. Motivations for New Tracking Detector Concepts

In this Chapter the basic motivation for a diamond tracking detector is illustrated. Upgrade plans which include precise performance requirements are introduced.

2.1. Basic Motivation for New Tracking Detector Concepts

Especially for new heavy particles the production cross section decreases with E_{CM}^{-2} [14]. To be sensitive to these rare events and to reduce measurement errors, a large event statistic is essential. For this purpose the integrated luminosity has to be maximised by increasing the instantaneous luminosity and by increasing the runtime. At the LHC, the instantaneous luminosity is increased in different phases which are summarised in Table 2.1. With increasing

time period:	peak luminosity: $[\mathrm{cm}^{-2}\mathrm{sec}^{-1}]$
2010	$0 - 2.2 \times 10^{32}$
2011-2016	$2.2 \times 10^{32} - 1 \times 10^{34}$
phase 1 upgrade (2016-2020)	2×10^{34}
phase 2 upgrade (> 2020)	$(\geq 1 \times 10^{35})$

Table 2.1.: Plans for the peak luminosity at ATLAS [15].

integrated luminosity radiation damages in the sensor material and the readout electronic of the detector diminish the functionality of the detector, see Section 3.3. For this reason, radiation hardness is a fundamental requirement for future LHC detector upgrades.

2.2. ATLAS Upgrade Plans: IBL and Future Plans for HL-LHC

Since with a smaller distance to the collision point the particle flux increases, the subdetector with the highest radiation damage is the innermost layer of the ATLAS pixel detector. To ensure complete operational capability of the tracking detector, an insertable B-layer[1] (IBL) [16] will be added to the present pixel detector in 2016 as a fourth layer, which will at least compensate the diminished functionality of the present innermost layer. It will be located between a new beam pipe and the current inner pixel layer at a radius of 3.7 cm and therefore has to resist an even higher particle flux.

The sensor material has to fulfil the following performance requirements, even after a fluence of 5×10^{15} $\mathrm{n_{eq}/cm^2}$:

---

[1] *B-layer* stands for *bottom quark layer* as the innermost layer is essential for the reconstruction of secondary vertices, which are characteristic for the decay of bottom quarks.

1. a hit efficiency of $> 97\%$ in the active area for a single MIP[2],

2. an r-ϕ resolution[3] of $< 10~\mu$m for a MIP at a 2T B-field and a particle incidence of $15°$,

3. a z resolution[4] of 72 μm for a MIP,

4. a maximal bias voltage of 1000 V.

Three sensor technologies are tested for IBL:

1. **planar pixel:** In comparison to other sensor technologies planar pixels, based on silicon, are cheap in production, and a lot of experience has been gained with them in the current ATLAS pixel detector. Instead of using n^+ pixels in n-type bulk material (n-in-n), an n-in-p design is aimed for to avoid type-inversion of the bulk material. At the moment thin layers of $< 250~\mu m$ are studied which show better charge collection after irradiation. Various planar pixel options are listed in [16].

2. **3D-pixel:** In contrast to planar pixels the electrodes are driven into the silicon bulk, so that the distance between p and n-electrodes is smaller than the bulk thickness. While the signal is still generated over the full bulk thickness, a lower depletion voltage is necessary to collect the complete charge. In addition, the readout is faster as the travel distance is shorter. Recent results are presented in [17].

3. **pCVD diamond[5] pixel:** Diamond provides excellent intrinsic material characteristics for a radiation hard tracking detector. These properties are explained in detail and are compared to silicon in Section 3.4.
   In high energy physics experiments, pCVD diamonds have already been used as beam condition monitors at BaBar, CDF and all four LHC experiments [18, 19].

Using scCVD[6] (single crystal CVD) instead of pCVD (polycrystalline CVD) diamonds as sensor material, the next generation of diamond detectors is studied in this diploma thesis.

In a larger context scCVD diamond tracking detector technology is interesting for the phase 2 upgrade in 2020, also called High Luminosity LHC (HL-LHC) or Super LHC (SLHC). For this upgrade the complete inner detector will be replaced.

---

[2]A MIP is a minimal ionising particle, see Section 3.2.2.

[3]The r-ϕ plane is perpendicularly orientated to the beampipe.

[4]The z-coordinate is parallel to the beampipe.

[5]Polycrystalline chemical vapour deposited (pCVD) diamond is a synthetic diamond. The production methods and its specific properties will be introduced in detail in Section 4.2.

[6]Single crystal CVD diamonds will also be introduced in Section 4.2.

3. Fundamental Physical Processes in a Diamond Tracking Detector

In this Chapter, all physically relevant processes of a diamond tracking detector are introduced. In the first Section, the electronic properties of a diamond are summarised. The electronic band structure is introduced to define diamond as an insulator. Including the effect of charge trapping, the electrical conductivity is developed from the basic ideas of the Drude Model. In the beginning of Section 3.2, the general operation principle of a tracking detector is briefly summarised, getting an overview about the various physical processes. Subsequently, the individual processes of the signal formation like energy deposition and charge collection will be explained in detail. An additional Section 3.3 about irradiation defects and their quantification by the damage coefficient is inserted. In the last Section 3.4 general material properties of diamond are compared with silicon. It exposes the superior performance of diamond concerning radiation hardness.

3.1. Electronic Properties of Diamond

An extensive description of the electronic properties of diamond is given in [20] where the phenomena are rigorously motivated by the quantum mechanics of solids. The most important electronic properties are summarised here.

3.1.1. Electronic Band Structure

A free carbon atom consists of two core electrons ($1s^2$) and four valence electrons ($2s^2$ and $2p^2$). The orbitals of the core electrons will not be studied explicitly since they do not directly contribute to the electrical conductivity in a carbon solid. In many solid models core electrons and atomic nuclei are combined to atomic cores, which form an effective potential.

In a diamond, an allotrope of a carbon solid, N carbon atoms are grouped in a diamond crystal lattice by forming tetrahedral and overlapping sp^3 hybrid orbitals with the 4N valence electrons, see Figure 3.1(a). During the formation of the crystal lattice the degeneracy of the 4N discrete states is removed, and in a simplified model two quasi-continuous energy bands are formed. The band with the higher potential is called *conduction band*; the other band is called *valence band*. They are separated by the band gap, see Figure 3.1(b). The electron energy E of the various bands depends on the direction of the electron wave vector. The band gap energy is defined as the energy difference between the lowest energy of the conduction band and the highest energy of the valence band with respect to the wave vector. Diamond shows an *indirect band gap* with an energy difference of $E_g = 5.48$ eV since these two energy extrema depend on different wave vectors.

Constrained by the occupancy of the two bands and the width of the band gap, solids are classified in three categories: 1. In a *conductor* the valence band and the conduction band energetically overlap, and/or the conduction band is partially filled with electrons. 2. An *insulator* has a large band gap of some electron Volts. Here the valence band is completely filled with electrons, whereas the conduction band is also empty at higher temperatures. 3.

(a)

(b)
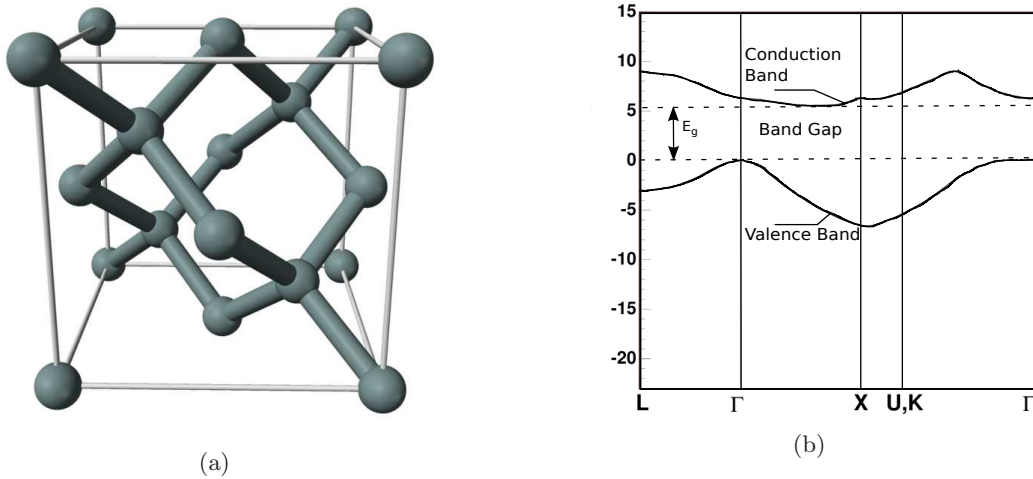
Figure 3.1.: (a) Diamond crystal lattice composed of overlapping sp^3 hybrid orbitals, (b) electronic band structure of diamond: electron energy levels along a path of wave vectors in the Brioullin zone. The upper graph represents the lowest energy branch of the conduction band, and the lower graph represents the highest energy branch of the valence band [20].

A *semiconductor* resembles an insulator with a smaller band gap so that electrons from the valence band can reach the conduction band by thermal energy. The vacant electron states in the valence band are called holes. In an intrinsic semiconductor the density of electrons in the conduction band and the density of holes in the valence band are equal; this density is called the *intrinsic charge carrier density n_i*.

Calculated via Fermi statistics at room temperature diamond has an intrinsic charge carrier density of 10^{-29} cm^{-3} and silicon of 10^9 cm^{-3} [20]. At room temperature, the intrinsic charge carrier density is therefore negligible and diamond is classified as an insulator.

3.1.2. A Simple Model of Electrical Conductivity

In an intrinsic semiconductor the pair of an electron in the conduction band and the corresponding hole in the valence band are defined as *intrinsic charge carriers*, also called free charge carriers. Both, the electrons in the conduction band and the holes in the valence band, can move in their particular bands.

Applying an external electric field, a force $\vec{F} = -e\vec{E}$ acts on the electrons as well as on the holes which start to accelerate in opposite directions. Scattering processes counteract this acceleration. Today three different scattering processes are considered: 1. In most cases scattering is understood as the interaction of the charge carrier with a phonon[1]. 2. Carrier-carrier scattering occur rarely and will be ignored. 3. Charge centre scattering[2] does not occur in a perfect crystal lattice and therefore is initially ignored.

The relaxation time τ_e for an electron or τ_h for a hole corresponds to the time between two electron or hole scattering events. Two independent equations of motion can be set up for electrons

---

[1] Short definition of phonons: Phonons are quantised lattice vibrations.

[2] Charge centres are additional energy levels within the band gap due to a defect in the crystal lattice, see Section 3.1.2

and for holes in a perfect solid:

$$m^*_{(e/h)} \left(\partial_t \vec{v}_{(e/h)} + \frac{\vec{v}_{(e/h)}}{\tau_{(e/h)}} \right) = -e\vec{E} \tag{3.1}$$

where $v_{(e/h)}$ is the charge carrier velocity which is also called drift velocity. $m^*_{e/h}$ corresponds to the effective mass[3]. In 1900 this differential equation has already been set up by Drude [21, 22] in a model of hard scattering between electrons and atomic cores motivated by the classical kinetic gas theory (Drude Model). These equations of motions can be solved by constant drift velocities:

$$\vec{v}_{(e/h)} = \frac{e\tau_{(e/h)}}{m^*_{(e/h)}} \vec{E} = \mu_{(e/h)} \vec{E}. \tag{3.3}$$

The tensor quantities $\mu_{(e/h)} := e\tau_{(e/h)}/m^*_{(e/h)}$ are called electron/hole mobility.

Intrinsic current density: In an intrinsic semiconductor the electron and hole densities are identical: $n_e = n_h =: n_i$ and the intrinsic current density can be defined:

$$\vec{j} := \vec{j}_e + \vec{j}_h := en_e\vec{v}_e + en_h\vec{v}_h = en_i(\mu_e + \mu_h)\vec{E} = en_i\mu\vec{E} = \sigma\vec{E} \quad \text{(Ohm's law)} \tag{3.4}$$

where $\mu := \mu_e + \mu_h$ is called mobility sum and $\sigma := en_i\mu$ corresponds to the electrical conductivity. In first instance, the intrinsic current density increases linearly with the electric field. In reality a maximal current density exists due to a maximal drift velocity $\vec{v}_{sat}$ if the drift velocity converges to the velocity of thermal equilibrium v_{th}. In this saturated state which occurs from a certain electric field strength ($\vec{E}_{sat}$) on the mobility is inversely proportional to the electric field.

After introducing the basic model of electrical conductivity the model has to be extended to consider charge centres due to defects as well as excess charge carriers, which are essential for the signal formation in a diamond since practically no intrinsic charge carriers exist.

First Model Extension: Presence of Charge Traps

While an intrinsic semiconductor possesses only intrinsic charge carriers in the valence and conduction band a real semiconductor exhibits lattice defects which exist by nature, radiation damage or artificial doping. These defects generate additional energy bands within the band gap where charge carriers can be trapped. In the first part of this Section, point defects are briefly illustrated. In the second part trapping mechanisms for electrons are introduced. Similar mechanisms exist also for holes; they can be introduced in an analogous manner.

---

[3]Definition of the effective mass of an electron in the conduction band: the dispersion relation for an electron $\vec{v}_e = \frac{\partial E(\vec{k})}{\hbar \partial \vec{k}}$ can be approximated at the minimal energy $E(\vec{k})_{\vec{k}=0}$ of the conduction band using a second order approximation for the energy: $E(\vec{k}) = E(0) + \frac{1}{2}\left(\frac{d^2E}{d\vec{k}^2}\right)_{\vec{k}=0}\vec{k}^2$. It follows:

$$\vec{v}_e \approx \left(\frac{d^2E}{d\vec{k}^2}\right)_{\vec{k}=0} \frac{\vec{k}}{\hbar} =: \frac{\hbar\vec{k}}{m^*_e}. \tag{3.2}$$

The effective mass is therefore defined as a second-order tensor. In an isotropic solid the tensor can be diagonalised with equal diagonal elements. In a simplification, this scalar quantity is often also called effective mass.

The effective mass of a hole can be defined in the same way using an energy approximation around the maximum of the valence band.

Point Defects in Diamond:
Some solid characteristics like electrical and thermal conductivity, colour, luminescence as well as radiation hardness highly depend on the concentration of point defects. In Figure 3.2 four
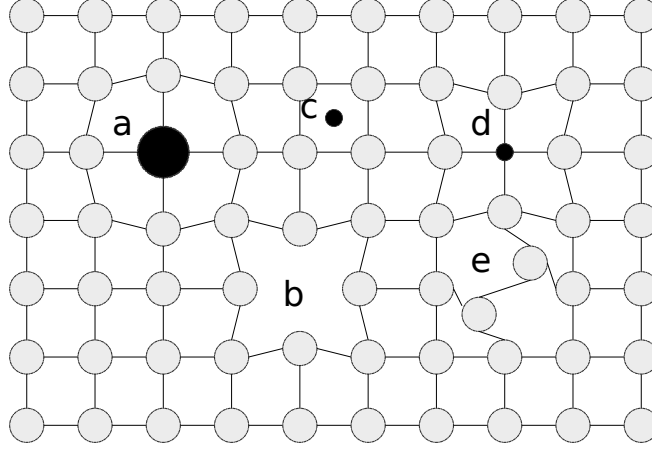
Figure 3.2.: Point defects: (a) foreign substitutional atom (e.g. N,P), (b) vacancy, (c) foreign interstitial atom (e.g. H, Li), (d) foreign substitutional atom (e.g. B), (e) self interstitial.

different point defects are illustrated: foreign substitutional and foreign interstitial atoms, self interstitials and vacancies. These defects establish new energy levels within the band gap and can work as trapping centres, which influence the lifetime of the charge carrier. The lifetime in general is correlated to the concentration of defects n_{def}[23]:

$$\tau_{def} = \frac{1}{v_{th}\sigma_{def}n_{def}} \tag{3.5}$$

where v_{th} is the thermal velocity of the charge carriers and σ_{def} is the cross-section of point defects.

Impact on the model of electrical conductivity:
In a first approach two types of additional energy levels are considered:

1. Active Electron Trapping States (AETS) with a concentration of N_{AETS} at an energy E_{AETS} are located within the band gap near the conduction band. These levels are called active as electrons can be trapped and detrapped. Since thermal energy has to be spent for detrapping, this process is diminished by a Boltzmann factor ($e^{-(E_{CB}-E_{AETS})/k_BT}$). A concentration of n_{AETS} states is actually filled with electrons.

2. Deep Electron Trapping States (DETS) are positioned near to the middle of the band gap (concentration: N_{DETS}, energy: E_{DETS}). Electrons can be trapped in these states. A large Boltzmann factor suppresses detrapping, which is therefore negligible. In this case the trapping is also denoted as recombination. A concentration of n_{DETS} states is actually filled with electrons.

In Figure 3.3, the extended electronic band structure is illustrated. The average trapping time
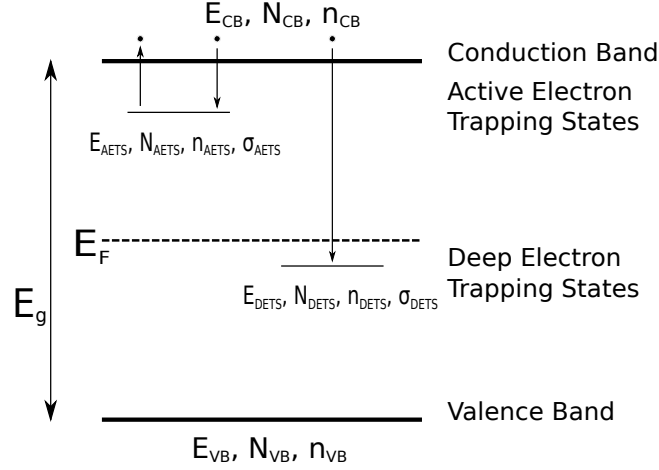
Figure 3.3.: Electronic band structure extension: Crystal defects establish new energy levels in the band gap like Active Electron Trapping States (AETS) and Deep Electron Trapping States (DETS). Analogue states exist for holes which have not been inserted in the plot.

of these states depends on the concentration of electrons in these states, the cross-section and the thermal velocity:

$$\tau_{\text{trapping}}^{\text{AETS}} = \frac{1}{(N_{\text{AETS}} - n_{\text{AETS}})v_{\text{th}}\sigma_{\text{AETS}}} \quad \text{and} \quad \tau_{\text{recombination}}^{\text{DETS}} = \frac{1}{(N_{\text{DETS}} - n_{\text{DETS}})v_{\text{th}}\sigma_{\text{DETS}}} \quad (3.6)$$

The detrapping rate for AETSs is given by:

$$\tau_{\text{detrapping}}^{\text{AETS}} = \frac{e^{-(E_{\text{CB}} - E_{\text{AETS}})/k_{\text{B}}T}}{N_{\text{CB}}v_{\text{th}}\sigma_{\text{AETS}}}. \quad (3.7)$$

As shown in [20] two first-order, non-linear, coupled differential equations follow by setting up infinitesimal rate equations:

$$\frac{dn_{\text{CB}}}{dt} = -\frac{dn_{\text{AETS}}}{dt} - \frac{n_{\text{CB}}}{\tau_{\text{recombination}}^{\text{DETS}}} \quad \text{and} \quad (3.8)$$

$$\frac{dn_{\text{AETS}}}{dt} = -\frac{n_{\text{AETS}}}{\tau_{\text{detrapping}}^{\text{AETS}}} + \frac{n_{\text{CB}}}{\tau_{\text{trapping}}^{\text{AETS}}}. \quad (3.9)$$

Since it is impossible to decouple these differential equations no analytical solution exists. A common quasi-equilibrium approximation ($\frac{dn_{\text{CB}}}{dt} \ll \frac{n_{\text{CB}}}{\tau_{\text{recombination}}^{\text{DETS}}}$) is made to solve these equations. Equation 3.8 simplifies:

$$\frac{dn_{\text{AETS}}}{dt} \approx -\frac{n_{\text{CB}}}{\tau_{\text{recombination}}^{\text{DETS}}}. \quad (3.10)$$

The solution:

$$n_{\text{CB}} = n_{\text{AETS}} \frac{\tau_{\text{e}}^{\text{trap}}}{\tau_{\text{detrapping}}^{\text{AETS}}} \quad (3.11)$$

includes the Matthiessen rule:

$$\frac{1}{\tau_{\mathrm{e}}^{\mathrm{trap}}} := \frac{1}{\tau_{\mathrm{trapping}}^{\mathrm{AETS}}} + \frac{1}{\tau_{\mathrm{recombination}}^{\mathrm{DETS}}}. \tag{3.12}$$

Analogue calculations can be applied to the holes.

<u>Carrier drift length</u>: Finally the carrier drift length is defined as:

$$
\begin{aligned}
s \quad &:= \quad s_e + s_h := \tau_e^{trap}|\vec{v}_e| + \tau_h^{trap}|\vec{v}_h| \tag{3.13}\\
&= \quad |\tau\mu\vec{E}| \tag{3.14}
\end{aligned}
$$

with

$$\tau := \frac{\tau_{\mathrm{e}}^{\mathrm{trap}}\mu_{\mathrm{e}} + \tau_{\mathrm{h}}^{\mathrm{trap}}\mu_{\mathrm{h}}}{\mu}. \tag{3.15}$$

Concerning a material layer of thickness D (orientated in z-direction) the average carrier drift in z direction is defined as:

$$\bar{s} := \frac{1}{D}\int_0^D s(z)dz = \frac{\mu E}{D}\int_0^D \tau(z)dz := \mu E\bar{\tau} \tag{3.16}$$

where $\bar{\tau}$ is the average lifetime over the layer thickness. In this equation it is assumed that the electric field is constant and parallel to the z direction, and the carrier drift length only depends on z.

Second Model Extension: Charge Carrier Excitation

For the electric conductivity of diamond the excitation of electrons in the valence band to the conduction band is necessary since diamond is an insulator and consequently has no intrinsic charge carriers. Excess charge carriers can be generated by ionisation where a charged particle with sufficient energy interacts with the electrons in the valence band.

3.2. Signal Formation in a Diamond Tracking Detector

Based on the introduced electronic mechanisms the operational principles of a tracking detector are developed. After a general overview the individual processes like energy deposition and charge collection will be described in detail.

3.2.1. Fundamental Concept of a Diamond Tracking Detector

The basic operational principles are similar for almost every tracking detector: A charged particle traverses a sensor layer and ionises the sensor material along the track. Applying an electric field the excess charge carriers (as well as the intrinsic charge carriers) of the sensor material will be collected on the electrodes. By a segmentation of these electrodes in pixels or strips the position of the track can be determined.

In Figure 3.4 a scheme of a diamond tracking detector is shown. The electric field is applied between the backplane and the pixels. The collected charge on the pixels will be read out by the front-end which is connected to the sensor layer via bump bonds. The complete readout process of the front-end will be described in detail in Section 4.3.1.
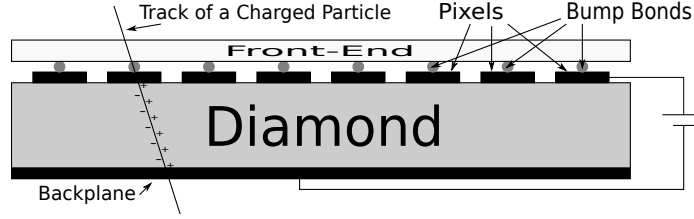
Figure 3.4.: Schematic view of a diamond tracking detector which is traversed by a charged
track.

In contrast to silicon, which is a semiconductor, for diamond as an insulator doping of the sensor
material and depletion during operation is not necessary since practically no intrinsic charge
carriers exist. In comparison to other solid tracking detectors a diamond tracking detector thus
has the simplest operation mode.

3.2.2. Energy Deposition

A charged particle which traverses a material deposits energy in various processes: 1. in inelastic
collisions with the electrons of the material, 2. in elastic collisions with the atomic nuclei of the
material, 3. via Bremsstrahlung, 4. via Cerenkov radiation and 5. in nuclear reactions. For
particles with masses significantly larger than the electron mass and sufficient kinetic energy, the
first process dominates and causes ionisation. For $\beta\gamma > 500$ radiative losses by Bremsstrahlung
prevail. In the $\beta\gamma$ range of 0.1 to 500 the average rate of ionisation loss for a charged particle
in matter, also called stopping power, was first calculated quantum mechanically by Bethe and
Bloch[4] [2]:

$$-\frac{1}{\rho}\left\langle\frac{dE}{dx}\right\rangle = K\frac{Z}{A}\frac{z^2}{\beta^2}\left[\ln\left(\frac{2m_ec^2\beta^2\gamma^2W_{max}}{I^2}\right) - 2\beta^2 - \frac{\delta(\beta\gamma)}{2}\right] \tag{3.17}$$

where $\delta(\beta\gamma)$ is a density correction which reduces the stopping power at large $\beta\gamma$. In Table 3.1
all used parameters are listed.

Material dependence only occurs in the ratio Z/A, which is roughly 1/2 for most materials, and
in the effective ionisation potential (I), which only contributes logarithmically.

In Figure 3.5(a) $< dE/(\rho dx) >$ is plotted as a function of $\beta\gamma$. For $\beta\gamma < 0.1$ the model of Bethe
and Bloch is not valid any longer since the charged particle looses energy by other processes
than ionisation, e.g. nuclear reactions.

In detector physics scenarios are calculated, in which the traversing particle deposits minimal
energy and therefore produces a minimal signal. In this case the particles are called *minimal
ionising particles* (MIPs). They have a stopping power of circa 1.5 MeVcm^2/g and are also a
good approximation for more energetic particles as the stopping power slowly rises with increas-
ing $\beta\gamma$.

So far the *average* rate of ionisation loss has been studied. Focusing on the deposited energy
distribution in a thin sensor layer many traversing particles deposit a rather small amount of
energy and only a few particles deposit the maximal possible kinetic energy W_{max} in scattering
processes. This asymmetric energy distribution was first described by Landau [25]. In Figure
3.5(b) some Landau distributions are plotted for a MIP passing silicon layers of three different

---

[4]The Bethe Bloch formula is only valid in the approximation: $M^2 \gg m_e^2 + 2m_eE$.

E	energy of the traversing particle
M	mass of the traversing particle
z	charge of the traversing particle,
K	$= 2\pi N_A r_e^2 m_e c^2 = 0.1535 \ \text{MeVcm}^2/\text{g}$
N_A	Avogadro constant ($= 6.0221 \times 10^{23} \ \text{mol}^{-1}$)
r_e	classical electron radius ($= e^2/(4\pi\epsilon_0 m_e c^2) = 2.8179 \times 10^{-15} \ \text{m}$)
m_e	electron mass ($= 0.511 \ \text{MeV/c}$)
ϵ_0	permittivity of free space ($8.8542 \times 10^{12} \ \text{F/m}$)
c	speed of light ($2.9980 \times 10^8 \ \text{m/s}$)
ρ	mass density of the medium
Z	atomic number of the medium
A	atomic weight of the medium
β	$:= v/c$ velocity of the traversing particle
I	effective ionisation potential averaged over all electrons
δ	density correction
W_{max}	maximal energy transfer in a single collision
γ	$= \dfrac{1}{\sqrt{1-v^2/c^2}}$

Table 3.1.: List of parameters used in Equation 3.17.

(a)

(b)
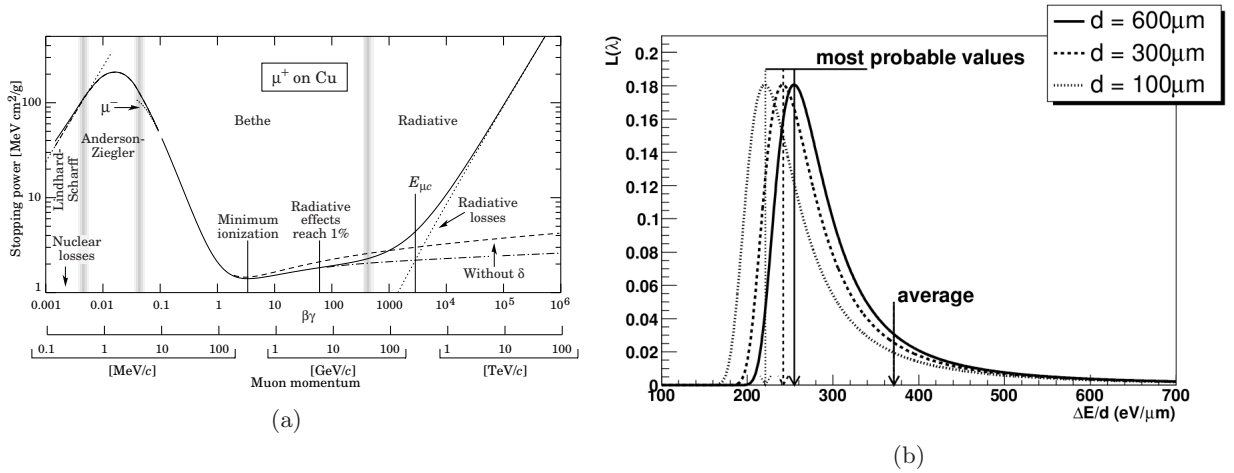
Figure 3.5.: (a) The stopping power for positive muons in copper is plotted as a function of $\beta\gamma$ [2]. Vertical bands indicate the region described by the Bethe-Bloch formula. (b) Modelling the energy distribution in a thin sensor layer Landau distributions are shown for three different silicon sensor thicknesses [24].

thicknesses. As illustrated the most probable value (MPV) significantly changes with the thickness of the sensor material whereas the mean value is basically the same for all three thicknesses. In place of a Landau distribution a convolution of a Landau and a Gaussian distribution can be used, which shifts the MPV and reduces the asymmetry of the Landau distribution. This convolution, which is also called *Langau*, is motivated by the consideration of resonances in the higher moments of the collision cross-section [26].

3.2.3. Signal Generation on the Pixels

Two transport mechanisms are important for the signal generation in a solid detector. Next to the charge carrier drift in an electric field, which has been explained in Section 3.1, diffusion is a relevant transport mechanism. Diffusion can be described as a thermally stimulated random-walk of charge carriers due to a charge carrier concentration gradient, which results in a Gaussian spread of the charge carriers. It can be characterised by the σ of the Gauss distribution:

$$\sigma = \sqrt{Dt} \tag{3.18}$$

where t is the time during which diffusion occurs, and D is the material dependent diffusion constant. A simple estimation of diffusion in an scCVD diamond tracking detector will be calculated in Section 6.3.3.

Instead of the intuitive picture of the signal generation by the collection of the excess charge carriers themselves a charge signal is induced on the pixels directly after the creation of the excess charge carriers. Generated by a moving excess charge q the induced signal current I on the pixels can be described by the Ramo Theorem [27]:

$$I_{ind} = -q\vec{v}\vec{E}_w \tag{3.19}$$

where $\vec{v}$ is the velocity of the excess charge carrier and $\vec{E}_w$ is the weighting field, which is defined by the electric field and the position of the excess charge carrier. If a parallel plate capacitor is considered: $\vec{E}_w = \vec{E}/U_{ext}$.

The Ramo Theorem has to be applied separately for electrons and holes. The total collected charge on a pixel corresponds to the integrated induced current of the electrons as well as of the holes, which depends on the charge collection distance, see next Section.

In Figure 3.6 the weighting field of a segmented sensor is illustrated. Since the field lines of the weighting field concentrate near the pixel, most charge is induced if the excess charge carrier is close to the pixel, which is called *small pixel effect*. Due to this effect the induced charge of charge carriers which are trapped away from the pixel is negligible. As shown in Figure 3.6 (case 2) charges next to the studied pixel can transverse the sensor, crossing the weighting field in different directions, so that in total no charge is induced.

3.3. Radiation Damage

Radiation hardness is a fundamental material requirement for a tracking detector closest to the collision point as it must endure the highest particle flux. If solid state tracking detectors are damaged by irradiation, the leakage current and therefore also the noise increase. In addition the charge collection is reduced by trapping, and a smaller signal is generated.

In the beginning of this Section the impact of irradiation is summarised. In the following two Subsections the quantification of radiation damage via charge collection distance and a damage coefficient are explained. Finally pumping is motivated as a method to diminish the initial concentration of traps.

3.3.1. Effects Caused by Irradiation

The irradiation of a solid by (charged) particles induces two types of effects [20]:
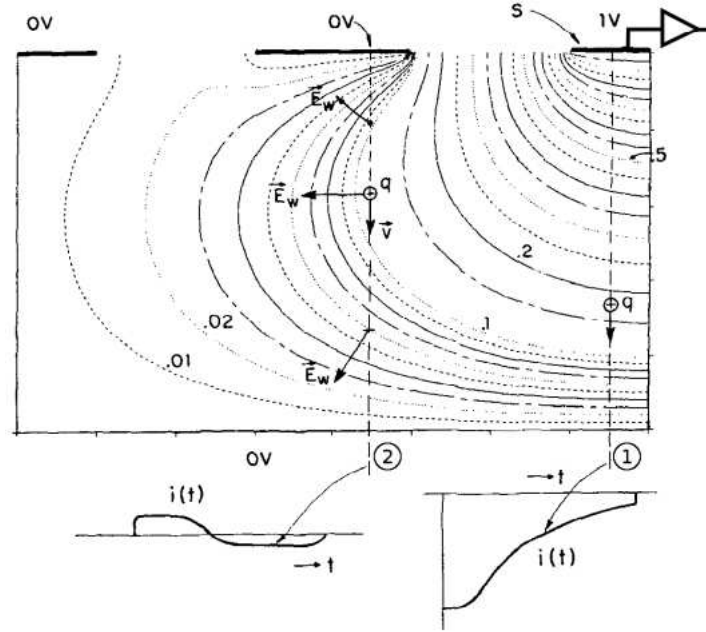
Figure 3.6.: Illustration of the weighting field of a pixel. In (1) most charge is induced when the excess charge carrier is close to the pixel. In (2) the weighting field is passed next to the studied pixel; in total no charge is induced as the weighting field is crossed in different directions [28].

1. **Ionisation:** As a charged particle traverses the solid electron/hole pairs are generated, which are separated by an external electric field. They can leave the solid via electronic contacts or are trapped at trapping centres. The latter effect is used in the pumping procedure, see Section 3.3.4.

2. **Crystal point defects:** If a particle enters the solid, energy can be transferred to the crystal lattice in a way, that atoms can get knocked from their lattice sites. These atoms are called primary knock on atoms (PKAs). A PKA leaves its lattice site and produces a vacancy. It might cause secondary knock on atoms (SKA) or stop at a free lattice site or interstitial lattice site. These point defects can recombine (beneficial annealing). If also SKAs leave their lattice sites and produce interstitials the defect is called a cluster defect. All these crystal defects occur in the bulk of the diamond due to non-ionising energy loss (NIEL) or radiation.

3.3.2. Charge Collection Distance

Charge Collection Distance (CCD) is defined as:

$$\text{CCD} := \frac{Q_{\text{collected}}}{Q_{\text{ionised}}} \, D = \frac{Q_{\text{collected}}}{36 \text{ e}/\mu\text{m}} \tag{3.20}$$

where $Q_{\text{collected}}$ is the measured charge at the pixels, Q_{ionised} is the original charge generated by ionisation and D is the sensor thickness. The value $36 \text{ e}/\mu\text{m}$ is empirically found [29, 30].
The charge collection distance can be associated with the average carrier drift length $\bar{s}$ (see

Equation 3.16) if CCD is smaller than the sensor thickness. It follows:

$$\mathrm{CCD} = (\tau_{\mathrm{e}}^{\mathrm{trap}}\mu_{\mathrm{e}} + \tau_{\mathrm{h}}^{\mathrm{trap}}\mu_{\mathrm{h}})\mathrm{E} = \tau\mu\mathrm{E}. \tag{3.21}$$

3.3.3. Damage Curve

It is observed that the concentration of radiation induced point defects is proportional to the radiation fluence ϕ[5]:

$$\phi \propto \mathrm{n_{def}} = \frac{1}{\mathrm{v_{th}}\sigma_{\mathrm{def}}\tau_{\mathrm{def}}}. \tag{3.22}$$

Therefore the original charge carrier lifetime τ_0 is additionally limited by these radiation induced defects τ_{def}. These two lifetimes can be summed to an actual lifetime τ via Matthiessen's rule. A linear relation follows between the lifetime rate $(1/\tau)$ and the radiation fluence ϕ [31]:

$$\frac{1}{\tau} = \frac{1}{\tau_0} + \frac{1}{\tau_{def}} = \frac{1}{\tau_0} + \beta\phi \tag{3.23}$$

where τ_0 corresponds to the lifetime before irradiation. The factor β depends on the radiation hardness. With Equation 3.21 it follows [23, 32]:

$$\frac{1}{CCD} = \frac{1}{CCD_0} + \frac{\beta\phi}{\mu E} \tag{3.24}$$

where CCD_0 is the charge collection before irradiation. Finally the CCD can be described via radiation fluence and CCD_0:

$$CCD = \frac{CCD_0}{1 + k\phi CCD_0} \tag{3.25}$$

where $k := \frac{\beta}{\mu E}$ is called the damage coefficient. Considering a saturated electric field, k is only sensitive to β since: $\mu \propto E^{-1}$, see Section 3.1.2.

A consistency check for the analysis of the damage coefficient would be the study of the increase of the leakage current due to a fluence ϕ [31]:

$$\Delta I = \frac{qn_iV\phi}{k} \tag{3.26}$$

where q is the electronic charge, V is the sensor volume and n_i the intrinsic carrier density.

3.3.4. Pumping

During the pumping procedure the diamond is irradiated with an intensive beam of charged particle, e.g. at CERN sensors are irradiated with 24 GeV/c protons generated by the PS (Proton Synchrotron).

In this process, deep electron trapping states in the diamond are passivated by capturing charge carriers. In contrast to these deep electron trapping states, active electron trapping states stay active at room temperature since they trap the charge carrier only for a short period, see Section 3.1.2. If CVD diamonds are kept at room temperature in the dark[6], the pumped state can last for months. To pump CVD diamonds a fluence of circa 10^{10} minimum ionising particles per cm^2 is sufficient [33].

---

[5]Definition of radiation fluence: In general it corresponds to the number of radiation particles per sensor area. Often it is normalised to the fluence of 1-MeV neutrons.

[6]Darkness is required as the diamond is not UV transparent.

3.4. Material Characteristics of Diamond and Silicon

In Table 3.2 various material properties are listed, which will be discussed with a special focus on radiation hardness.

Diamond (as an allotrope of carbon) and silicon are elements of the fourth main-group of the periodic table. Both solids show sp^3 hybridisation and are arranged in a diamond crystal structure.

With a nearest neighbour distance of 1.54^{-10} m diamond has the highest atomic number density of 1.77×10^{-23} cm^{-3} of any material. The cohesive energy[7] is almost twice as large as for silicon. This dense structure and strong bonding is the reason for the extreme radiation hardness.

Due to the large band gap of $E_g = 5.47$ eV the intrinsic charge carrier density is negligible and diamond is characterised as an insulator, whereas silicon has a small band gap of $E_g = 1.12$ eV and therefore is classified as a semiconductor. To reduce the intrinsic carrier density of a silicon tracking detector, the sensor must be depleted. In contrast, diamond can operate as a simple solid ionisation chamber without doping and negligible leakage current.

Because of the small dielectric constant and thus a small pixel capacitance, the noise of a diamond sensor is small. Due to the large band gap, the amount of excess charge carriers and thus the signal size are significantly smaller for diamond than for silicon.

In comparison to other materials, diamond has huge electron and hole mobilities: 1800 cm^{2}V^{-1}sec^{-1} and 1200 cm^{2}V^{-1}sec^{-1} respectively. A fast signal readout which is in the order of a few nanoseconds is possible, see Section 6.3.3.

Finally, diamond has an extremely large thermal conductivity in comparison to silicon. It can operate at room temperature with no thermal runaway problems.

---

[7]The cohesive energy is required to disassemble atoms in a solid.

properties:	diamond	silicon
atomic number Z	6	14
atomic weight A	12.01	28.09
atomic density ρ_n $[\times 10^{22}$ cm$^{-3}]$	17.7	4.96
mass density ρ [g cm^{-3}]	3.52	2.33
crystal structure	diamond	diamond
lattice constant a $[\times 10^{-10}$m]	3.57	5.43
nearest neighbour distance $[\times 10^{-10}$ m]	1.54	2.35
cohesive energy [eV/atom]	7.37	4.63
compressibility $[\times 10^{-11}$ m^{2}N$^{-1}]$	0.226	1.012
melting point [°C]	4100	1420
thermal conductivity σ_T [W cm^{-1} K^{-1}]	20	1.27
electron diffusion coefficient [cm^2 sec^{-1}]	47	38
hole diffusion coefficient [cm^2 sec^{-1}]	31	13
dielectric constant ϵ	5.7	11.9
band gap E$_g$ [eV]	5.48	1.12
E$_{pair}$ [eV]	13	3.6
intrinsic carrier density [cm^{-3}]	$< 10^{-29}$	1×10^9
resistivity [Ω cm]	$> 10^{13}$	2.3×10^5
electron mobility μ_e [cm^2 V^{-1} sec^{-1}]	1800	1350
hole mobility μ_p [cm^2 V^{-1} sec^{-1}]	1200	480
E$_{breakdown}$ [V cm^{-1}]	10^7	3×10^5
E$_{saturation}$ [V cm^{-1}]	$> 4 \times 10^4$	2×10^4
v$_{saturation}$ $[\times 10^7$ cm^1 sec$^{-1}]$	2.2	0.82

Table 3.2.: Physical properties of diamond and silicon [29, 20, 34].

4. Diamond Tracking Detectors for ATLAS

In this Chapter, the studied scCVD diamond tracking detector, CD181, is introduced, and its readout electronics, the front-end-I3, is explained. In the beginning the production methods of synthetic diamonds are summarised and the difference between pCVD and scCVD diamond is clarified.

4.1. Synthetic Diamonds

Diamond is a crystal which exists in nature but can also be produced artificially under certain conditions. Synthetic diamonds can be formed in two ways [35]:

1. **High Temperature High Pressure (HTHP)** Synthesis: Imitating the natural process graphite is converted into diamond under conditions at which diamond is the thermodynamically favoured phase ($> 1000\,^\circ$C, $> 10^7$ kPa).

2. **Chemical Vapour Deposition (CVD):** In a non-equilibrium process where diamond is metastable with respect to graphite diamond is synthesised from a hydrocarbon gas at lower temperature ($600 - 1000$ $^\circ$C) and lower pressure (10 kPa). The gas mixture consists of carbon, hydrogen and oxygen, where hydrogen dominates $99 : 1$.
   In a hot filament CVD reactor carbon deposits as graphite as well as diamond on a heated substrate. The faster deposited graphite is removed in an etching process with hydrogen. In addition hydrogen stabilises the deposited structure.

4.2. Polycrystalline (p) CVD and Single Crystal (sc) CVD Diamond

In a CVD process diamond can be produced in two qualities [35]:

1. **pCVD diamond:** Considering the cheaper method the substrate consists of individual diamond grains. In the beginning of the growth process diamond is deposited at various locations on the substrate with different lattice orientations. During the CVD process the individual condensation crystals grow together forming a polycrystalline (p) structure with grain boundaries. These defects cause charge trapping, and a signal deformation as signal charge is partially conducted along the boundaries.

2. **scCVD diamond:** A single crystal (sc) structure is produced if the substrate itself consists of a diamond with uniform lattice orientation. In contrast to pCVD diamond, scCVD diamond has no systematic incorporated defects. Less trapping and a more precise signal formation are expected.

4.3. First scCVD Diamond Tracking Detector Based on Front-End-I3

At CERN diamond tracking detectors are developed for high luminosity experiments at LHC in the RD42 collaboration. Within this collaboration the first scCVD diamond tracking detector, CD181, was developed in 2006, which uses the current ATLAS pixel readout electronics, the front-end-I3. In this thesis its performance is studied at different fluences.

The scCVD diamond itself has been produced by the CVD-diamond manufacturer "elementsix"[1]. It has a thickness of 395 μm and covers an area of roughly 1×1 cm^2. Due to the particular
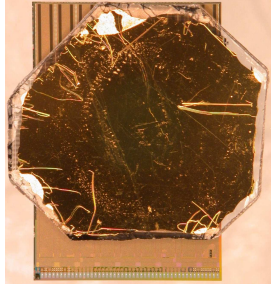
Figure 4.1.: CD181 bump bonded to a front-end-I3 [36].

outline of the diamond the front-end is not covered completely as shown in Figure 4.1.
In the following the front-end and the readout mechanism are explained.

4.3.1. Pixel Layout

The readout electrodes placed on one side of the sensor material are segmented in rectangular pixels with a general size of 400×50 μm^2. Each pixel electrode is connected to a pixel-cell on the front-end chip by a solder bump[2] (PbSn). One front-end chip reads out 2880 pixels which
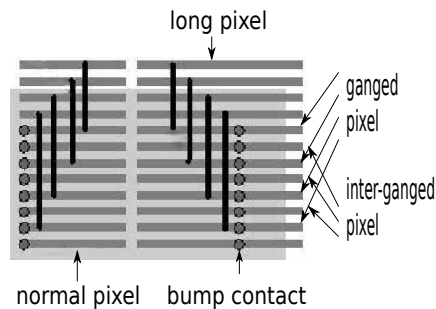
Figure 4.2.: Top right corner of a sensor which is connected to a single front-end-I3. The four different pixel types are plotted. The black lines indicate traces connecting two ganged pixels.

are grouped in 18 columns and 160 rows. To ensure the full coverage of the sensor also between the neighboured front-end chips[3], pixels are enlarged or connected in the border region between

---

[1]www.e6.com, former: "De Beers Industrial Diamonds".
[2]Produced by IZM, Institut für Zuverlässigkeit und Mikrointegration in Berlin.
[3]In the ATLAS pixel detector 8×2 front-end chips readout one sensor layer.

two front-end chips. As indicated in Figure 4.2 the outer columns (column: 0 and 17) consist of *long pixels* with a size of $600 \times 50 \mu$m; within the upper front-end region pixels are *ganged*, e.g. the pixels in row: 159/155, 158/153, 157/151, 156/149 are ganged and readout together. The bridged pixels in row 150, 152 and 154 are called *inter-ganged*. As mentioned in Section 6.0.3 all these special pixel types (long, ganged, inter-ganged) are masked out in this thesis because of low hit occupancy.

Each pixel-cell on the front-end chip manages the readout processes which will be explained in the next Section.

4.3.2. Operating Mode of an ATLAS Pixel Front-End Chip

The front-end chip is responsible for the digitisation and buffering of hit information until a trigger initiates further readout. In the common operation mode the front-end operates synchronously with the ATLAS beam clock, time intervals are counted as multiples of the LHC bunch crossing rate of 40 MHz (25 ns). These multiples are called bunch crossing units (BC). In Figure 4.3 a schematic overview of a front-end pixel-cell is plotted.

The charge signal, generated by a traversing charged particle, enters the charge sensitive preamplifier via the bump bond. Here a feedback scheme can compensate leakage currents, which
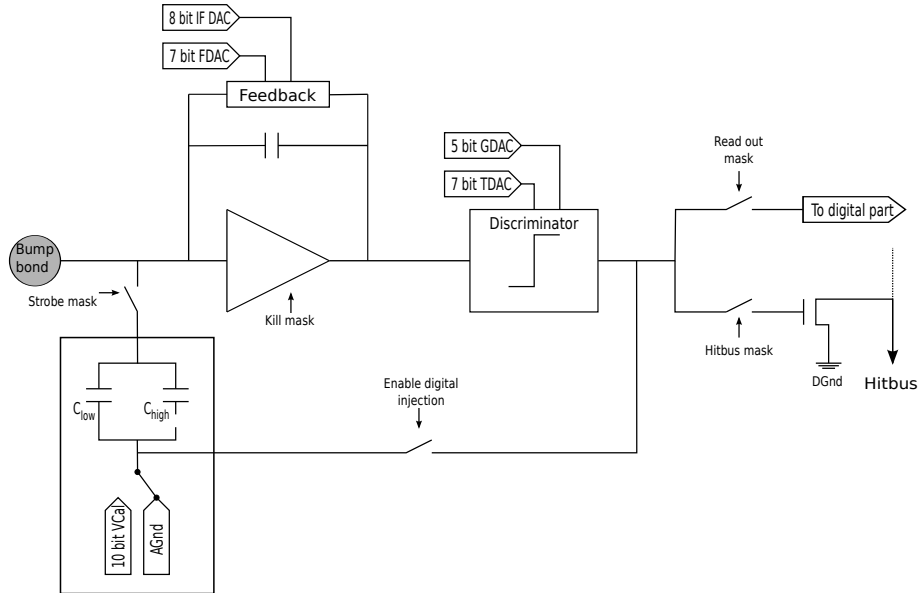
Figure 4.3.: Scheme of a pixel-cell on the front-end-I3 chip [37].

is not shown in the plot. The signal charge is collected on a feedback capacitance which is continuously discharged by an adjustable current source, so that the baseline is reproduced in the order of a micro second.

Each amplifier can be disabled, so that noisy sensor pixels, which for example are caused by shorts in the readout electronic, cannot evoke buffer-overflows, which can result in the loss of real hits.

A second amplifier collaborates with a differential discriminator, so that the pixels are readout in zero-suppressed mode. The discriminator threshold can be adjusted in the range from 1500 to 5000 electrons.

After an exponential rise the signal always peaks at the same time independent of the amount

of collected charge. Caused by the finite rise time smaller charge signals cross the threshold later than hits with bigger deposited charge. Hits with low charge are measured later since the discriminator output is sampled once every 25 ns. This effect of measuring simultaneously
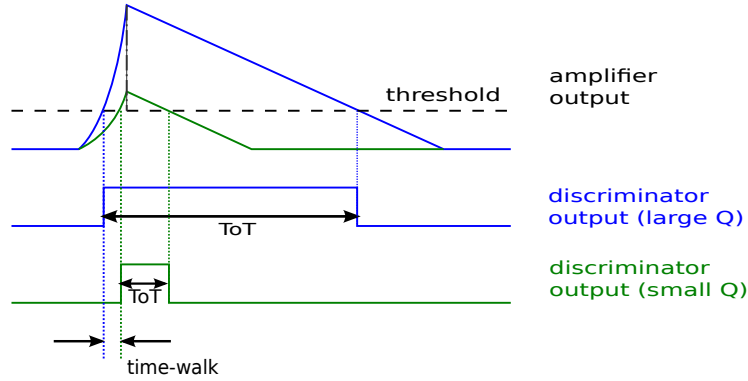
Figure 4.4.: Illustration of the zero-suppressed readout mode and time walk. Two simultaneously generated signals with different signal sizes and their ToTs are plotted [24].

generated hits with different amount of charges at different times is called *time walk* and is illustrated in Figure 4.4.

The discriminator threshold value is adjusted via two DACs, a global DAC (GDAC) and an individual trim DAC (TDAC) per pixel-cell to reduce pixel to pixel threshold variations. The constant discharge and thus the regeneration of the baseline is controlled via a global IF DAC and an individual feedback DAC (FDAC).

The time over threshold (ToT), which is the time between the leading and the trailing edge of the discriminator signal, has a fixed correlation to the deposited charge. A ToT-charge calibration curve allows the measurement of deposited charge, see Section 6.5.1.

After an electronic request the hit pixel-cells finally transfer pixel ID, bunch crossing ID and ToT to the subsequent readout system on the bottom of the chip which constantly scans pixel-cells for hits. Hit information is stored in an end of column (EoC) buffer. Each buffer manages two columns (320 pixels) and has a depth of 64 hits.

Controlled Charge Injection: To test the pixel-cells and to accomplish the ToT-charge calibration a well defined charge can be injected via two capacities: $C_{low} = 7.29$ fF and $C_{high} = 41.386$ fF. They are charged by the calibration voltage V_{cal} generated by the Vcal-DAC. The amount of charge is defined by $Q_{inj} = C_{low/high}\Delta V$. The slope of V_{cal} with increasing DACs is 0.9 mV/DAC, which corresponds to 41.54 e for C_{low} and 235.91 e for C_{high} per VCal-DAC step[4].

---

[4]A test capacity exist on each front-end chip and can be measured. The dispersion of the capacitor values per chip is 1.5% for C_{low} and 2.3% for C_{high} [24]

5. Testbeam Analysis Chain

5.1. General Concept of a Testbeam Analysis

To study the physical performance of a tracking detector, a substantial amount of precisely measured particle passages through the detector has to be recorded. For this purpose particles of well known energy, direction, intensity and particle sort are provided by a **testbeam**. To reconstruct the individual trajectories of the particles during the passage through the detector a reference system, a **beam telescope**, is set up around the Device Under Test, also called **DUT**. In general the telescope consists of some very precise detector planes which are positioned in front and behind the DUT. With the space points from this reference system the particle trajectory can be reconstructed. So the intersection point of the particle track in the DUT can be predicted. That way essential characteristics of a tracking detector like position resolution, efficiency, noise
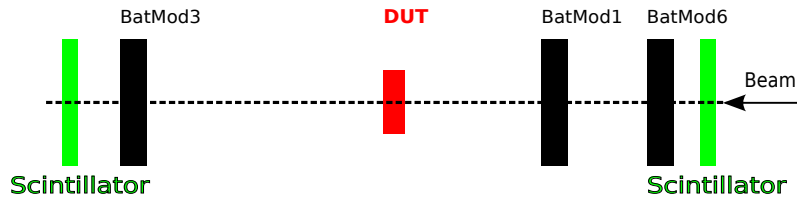
Figure 5.1.: Testbeam assembly: Black rectangles display the three telescope planes of the Bonn-ATLAS-Telescope, the DUT is drawn as a red rectangle, the scintillators are indicated in green and the path of the beam is indicated as a dotted line.

and charge sharing can be studied.

To trigger the readout of the DUT and the telescope, a fast coincidence signal of two scintillators is required. They are placed in front and behind the telescope. The telescope and DUT data, which belong to one trigger, are merged and stored together as one **event**. Succeeding events with the same adjustment are considered as a **run**. Originally, a typical run contained 25000 events (October 2006). Due to later observed desynchronisation problems[1], the run size was scaled down to 5000 events (July 2008) to reset the trigger IDs of the devices in shorter time intervals.

In addition to the intrinsic precision of the telescope the track reconstruction is limited by multiple scattering occurring in the telescope planes, the DUT and the air in between. As multiple scattering is inversely proportional to the particle energy, a high energetic beam is preferred. For this reason all data of this diploma thesis has been recorded at the ATLAS pixel testbeam assembly in the SPS North area at CERN, bld. 887. Generated by the SPS protons the H6 beam line provides 100 GeV pions as testbeam particles.

As a reference frame, the Bonn-ATLAS-Telescope was used, which will be introduced in the next Section.

---

[1]Desynchronisation denotes a trigger-timing problem amongst the readout devices (telescope planes and DUT) and will be explained and analysed in Section 5.3.1

5.2. Bonn-ATLAS-Telescope (BAT)

5.2.1. Assembly and Working Mode

In all testbeam periods the Bonn-ATLAS-Telescope (BAT) [38] was used as a reference system to reconstruct the particle trajectories. Originally it consisted of four double sided silicon microstrip sensors from Hamamatsu (part number: S6934). One telescope plane, which is also called BAT-Module (or BatMod), is shown in Figure 5.2. In this analysis only three modules: BatMod1, BatMod3, BatMod6 are used as the fourth module (BatMod2) is noisy and has been excluded in most of the testbeam periods. A scheme of the setup of the BAT is plotted in Figure 5.1.

To get two dimensional space information the strip electrodes on both sides of the 300 μm thick sensor layer are arranged perpendicularly to each other. One side of the sensor is made by p-implants and the other by n-implants; they are called p-side and n-side. Both sides are segmented in 640 parallel strips with a pitch of 50 μm and a length of 32 mm. The strips on each side are readout via five VA2 front-end ICs; each VA2 provides 128 low noise and low power charge sensitive preamplifier-shaper circuits, a serial analog output and additional calibra-

Figure 5.2.: Photo of a BAT-Module. [38]

tion features. The analog output is translated in a 12 bit digital signal measured in analog-to-digital units (ADUs).

To reduce the data taking, to minimise storage and the system dead time, the Bonn-ATLAS-Telescope works in a zero-suppressed readout mode. For this reason the telescope planes are not readout completely if an event is triggered. Only the strips which pass an adjusted signal threshold and in addition the two neighbouring strips on both sides are readout. In this way the complete collected charge is recorded as usually the deposited charge of one particle passage is not spread over more than three strips.

5.2.2. Preprocessing of the Telescope Raw Data

The pure Bonn-ATLAS-Telescope output signal of a strip which is digitised by an ADC (Analog-Digital-Converter) consists of three components:

$$\text{output signal} = \text{pedestal} + \text{noise} + \text{signal charge}. \tag{5.1}$$

Signal charge corresponds to the deposited charge generated by a passing testbeam particle. *Pedestal* is a strip specific fixed offset which comes from the sensor leakage current and the readout electronics. *Noise* corresponds to the fluctuation of this fixed offset value.

Since in zero suppressed mode it is nearly impossible to determine pedestal and noise, these signal contributions are measured in a special calibration routine before every run and in absence of signal charge. In this routine the output signal is sampled one hundred times for each strip. The mean value of this distribution corresponds to the pedestal and the RMS value to the noise. In a usual run this strip specific pedestal value is automatically subtracted from the output signal. In Figure 5.3 pedestal and noise for BatMod1 of run 1830 (November 2007) are shown. In first order the pedestal fluctuates randomly from strip to strip. A systematic variation per VA2 readout chip seems to exist (First VA2 chip manages strip 0-127, the second chip manages strip

(a)

(b)

(c)

(d)
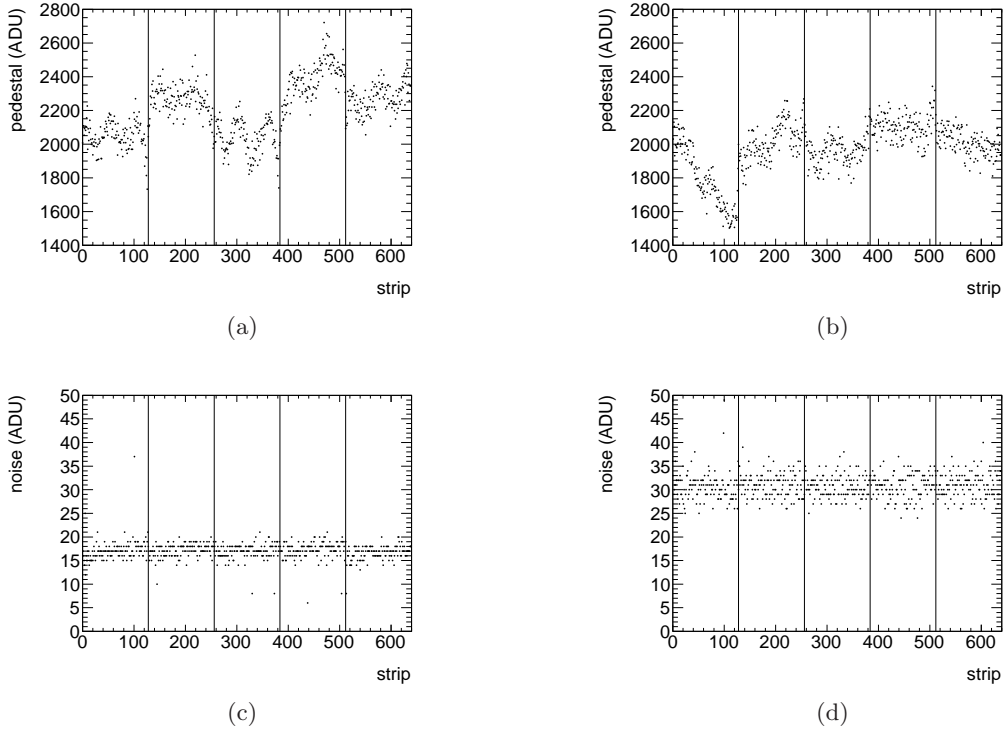
Figure 5.3.: (a) Pedestal of p-side, (b) pedestal of n-side, (c) noise of p-side, (d) noise of n-side for BatMod1. The division between the strips and the five VA2s is sketched by vertical lines (data: run 1830, November 2007).

128-255 and so on). In general, the pedestal on the n-side is circa 200 ADUs smaller than on the p-side. For unknown reasons the noise for p-side is between 14 and 20 ADUs and for n-side between 26 and 36 ADUs.

A typical threshold value for both sides is 128 ADUs. So the signal to noise ratio in these strips is bigger than $6.4\,\sigma$ for p-side and $3.5\,\sigma$ for n-side.

To illustrate the charge distribution in events with one strip over threshold at n-side and p-side, the normalised strip signal spectra for the strip over threshold and the two neighbour strips on both sides are plotted in Figure 5.4. The spectra of the outer strips are fitted with a Gauss distribution. As the fit is approximately centred around zero, the signal of these strips is dominated by noise. For this reason the collected charge is not spread over more than three strips as it was stated in the last Section.

5.2.3. Cluster Size and Cluster Multiplicity

For the BAT, a cluster is defined as the accumulation of all adjacent strips over threshold and the two neighbouring strips below threshold on both sides. In Figure 5.5 the number of readout strips per event is shown for the p-side and the n-side of BatMod1 (run 1830, November 2007). In approximately 60% of all events exactly one particle traverses the module, which produces a cluster of five or six strips on p and n-side. In these clusters one or two strips per side are over threshold. The peaks at 10-11 or 15-16 readout strips indicate the passage of two or three particles per trigger. Fortunately, in most of the events only one particle traverses the module.
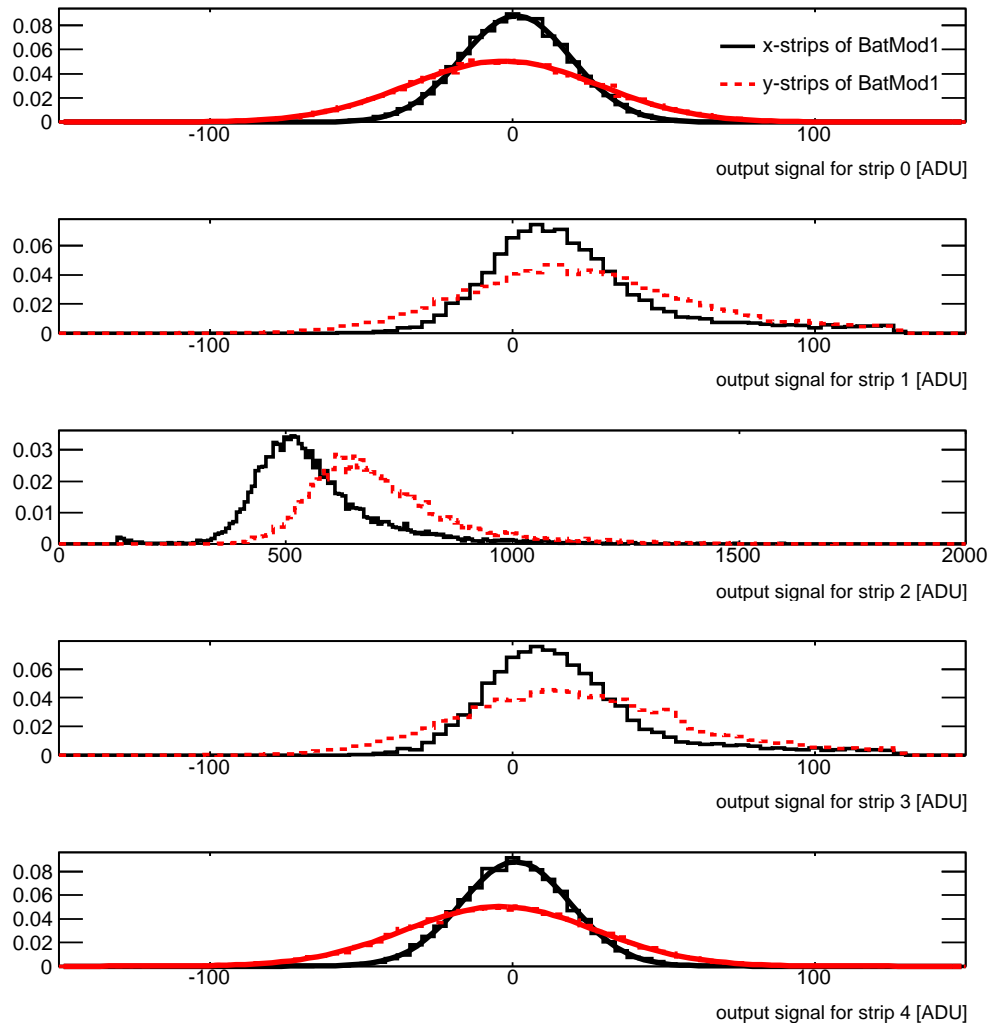
Figure 5.4.: Normalised telescope signal spectra of the five readout strips in events with only one strip over threshold (strip 2). For the outer strips (strip 0 and strip 4) the fitted Gauss distributions are also plotted (data: BatMod1, run 1830, November 2007).

To avoid readout ambiguities, which are illustrated in Figure 5.6, only events with one particle passage in all three BatMods (only events with five or six readout strips in each BatMod and on both sensor sides) are studied in this analysis. It is by far the tightest cut in the complete testbeam analysis chain. For example: in run 1830 only 35.5% of all 25050 events have exactly one cluster in each BAT module.

5.3. Overview: Data Processing

Before the complex steps in the analysis chain are explained in detail, an overview is given. Roughly the data processing can be separated in three independent parts:

1. **Preprocessing of the Telescope Data:**
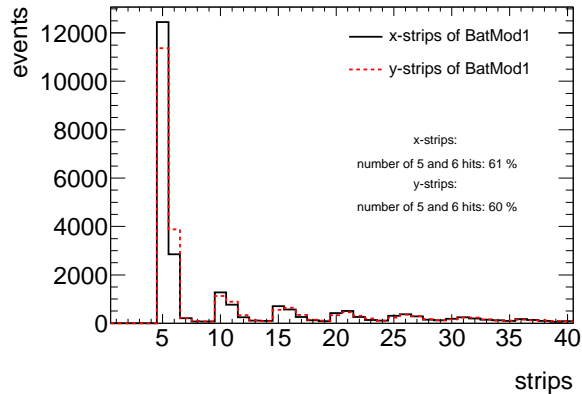
Figure 5.5.: Number of readout x- and y-strips per event in BatMod1 (data: run 1830, November 2007).
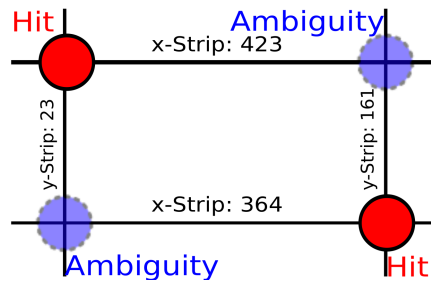
Figure 5.6.: Readout ambiguities: Four hit strips of a telescope plane are sketched for an event with two particle trajectories. Red circles indicate the actual hit positions. Based on the readout it is impossible to reconstruct whether the red circles or the blue circles represent the actual hit position.

As already explained in Section 5.2.2 the pedestal and noise of the telescope is determined in the beginning of each run. Then the determined pedestal is automatically subtracted from the output signal.

2. **Orientation, Synchronisation and Data Conversion:**
   After elaborated considerations the Eudet-Software (EuTelescope) was chosen for the central data-processing steps: clustering, alignment, track fitting. To prepare the Bonn-ATLAS-Telescope raw data for EuTelescope three steps are necessary:

   a) **Standardised Orientation:** As for the different testbeam periods the telescope planes and the DUT are rotated and flipped in different ways, the orientation is standardised for all testbeam periods: the telescope planes as well as the DUT are located in x-y-directions. So the z-direction is parallel to the beam. The DUT is always orientated in the way, so that the long pixel direction corresponds to the x-direction and the short pixel direction to the y-direction.

   b) **Synchronisation:** In some testbeam periods the data is strongly desynchronised. To solve this malfunction a specially designed synchronisation program has been written

and will be explained in Section 5.3.1.

   c) **Data conversion:** Finally the data is dumped in a root NTuple, which is compatible with the BAT-Eudet-Converter, see 5.3.2.

3. **Clustering, Alignment and Track Fitting with EuTelescope:**
EuTelescope is a software framework with a substantial collection of analysis routines especially designed for the Eudet-Telescope, which from this year on is used in the ATLAS testbeam community for IBL. Originally it was designed for the tracking detector development of ILC[2]. At the moment EuTelescope is adapted to the special sensor geometry for ATLAS tracking detector upgrades. For this thesis a couple of basic EuTelescope routines (also called processors) are used. Some fundamental modifications had to be done as in contrast to the Bonn-ATLAS-Telescope the Eudet-Telescope is segmented in pixels and not in strips. In the following, the main analysis steps, accomplished with the adjusted Eudet-Software, are summarised:

   a) **BAT-Converter Processor:** The prepared Bonn-ATLAS-Telescope data is converted in a specific format (Section: 5.3.3).

   b) **Clustering Processor:** Individual pixels or strips are combined to clusters (Section: 5.3.4).

   c) **HitMaker:** The hit position within a cluster is determined. Optionally an eta-correction can be applied. The cluster positions are transformed from a local coordinate system to a global coordinate system (Section: 5.3.5).

   d) **Alignment Processors**: Telescope and DUT are aligned successively (Section: 5.3.6).

   e) **Fitter**: The particle trajectory is reconstructed via a global fit through the telescope planes (Section: 5.3.7).

   f) **NTuple-Dumper:** Finally all important information is dumped in a root NTuple for the actual analysis.

4. **Real Testbeam Analysis:** Various analysis aspects will be presented and discussed in Chapter 6.

5.3.1. Synchronisation Procedure

Each telescope plane and DUT manages its own trigger-ID which is basically a counter incremented after receiving a trigger. The triggered output data of the different devices with the same trigger-ID are merged and stored together as one event.

Caused by complex timing problems in the readout hardware in a few events this incrementation is refused in a telescope plane or DUT. From this event on the device is delayed by one (trigger-)Δ-ID in comparison to the other devices and called desynchronised. In a synchronisation procedure this malfunction is corrected.

To illustrate the absolute importance of synchronisation the correlation between the seed-x-strips[3] of BatMod1 and BatMod6 is shown before and after synchronisation in Figure 5.7(a) and 5.7(b).

---

[2]ILC: The International Linear Collider is a potential successor of the LHC. On a straight distance of 31 km electrons and positrons are accelerated to a centre-of-mass energy of 500 GeV.

[3]The seed is the strip (or pixel) with the highest amount of deposited charge.
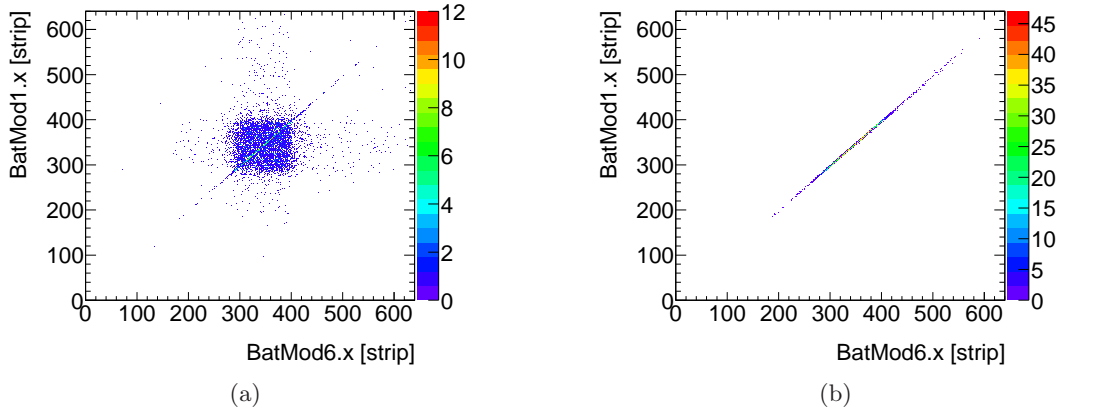
Figure 5.7.: (a) Correlation between the seed x-strips of BatMod6 and BatMod1 before the synchronisation procedure and (b) after the synchronisation procedure (data: run 1830, November 2007).

Synchronisation can be tested via different sensitive quantities: correlations or unbiased residuals. In this thesis the telescope planes and the DUT are synchronised via unbiased (and unaligned) residuals as it is a rather intuitive method. In Figure 5.8 the concept of an unbiased
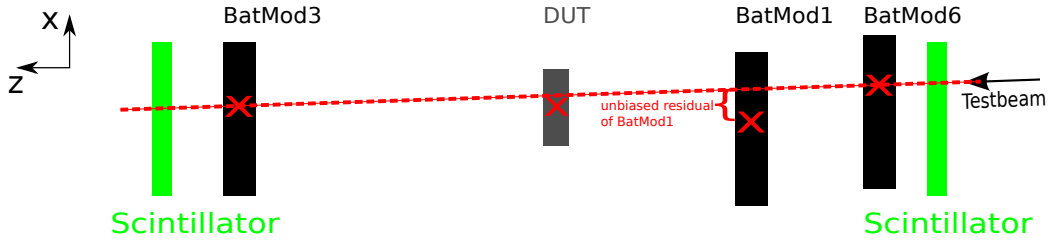
Figure 5.8.: Example of an unbiased x-residual of BatMod1: an unaligned telescope and DUT setup is shown. The measured hit positions are indicated with red crosses. The unbiased residual of BatMod1 is the distance between the hit in BatMod1 and the straight line, which is defined by the hits in BatMod3 and BatMod6.

x-residual of BatMod1 is illustrated. It is the distance between the seed x-strip of BatMod1 and the intersection of BatMod1 and the straight line which passes the seed x-strips in the other two planes (BatMod3 and BatMod6). At this time the BatMods are not aligned yet.

In Figure 5.9(a) the sensitivity of the unbiased residual with respect to desynchronisation is illustrated. The unbiased residual of BatMod1 is shown as a function of the original event number. In event 2768 a desynchronisation occurs, and the unbiased residuals of the succeeding events strongly fluctuate. To decide whether BatMod1 itself, BatMod3 or BatMod6 is desynchronised the unbiased residuals for the other two planes have to be studied. An event is regarded as synchronised if all six unbiased residuals of all three telescope planes (and x- and y-directions) pass run and plane specific tolerance cuts. In detail, the unbiased residual distributions of the first 500 (or less) synchronised events are fitted with a Gaussian distribution, and a 6σ wide tolerance range is defined around the Gaussian mean value. As an example, the unbiased x-residual distribution of the first 500 events of BatMod1 is shown in Figure 5.9(b).

(a)   (b)
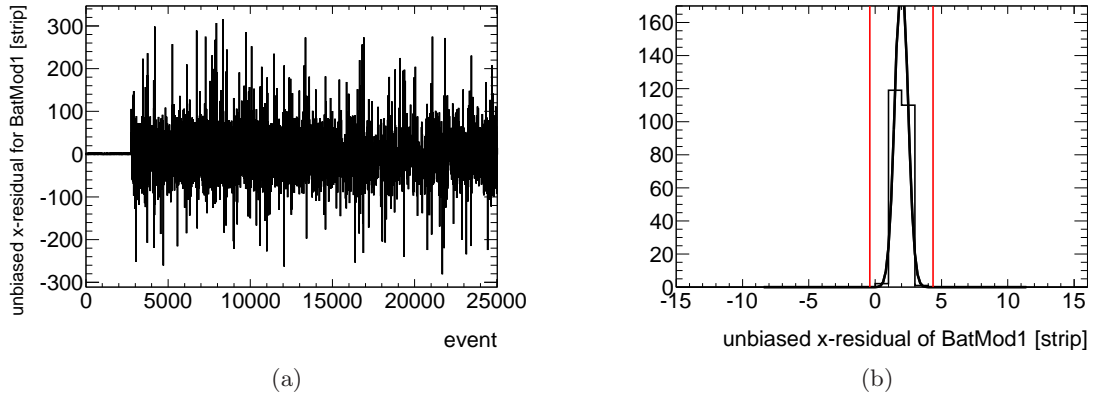
Figure 5.9.: (a) The unaligned and unbiased residuals of the x-strips of BatMod1 are plotted as a function of the original event number. (b) The unaligned and unbiased residual distribution of the x-strips of BatMod1 is illustrated for the first 500 synchronised events. The tolerance interval is indicated in red (data: run1830, November 2007).

An event is synchronised if the unbiased residuals of all three modules pass the specific tolerance ranges. Otherwise the event is desynchronised and the trigger-IDs of all modules will be shifted systematically until the synchronisation criterion is fulfilled. To minimise CPU power a maximal shift of five Δ-IDs for one module in comparison to the other two modules is allowed. In Figure 5.10 the final Δ-IDs of BatMod3 are plotted as a function of the synchronised event number. After the synchronisation of the telescope the DUT is synchronised in the same way.
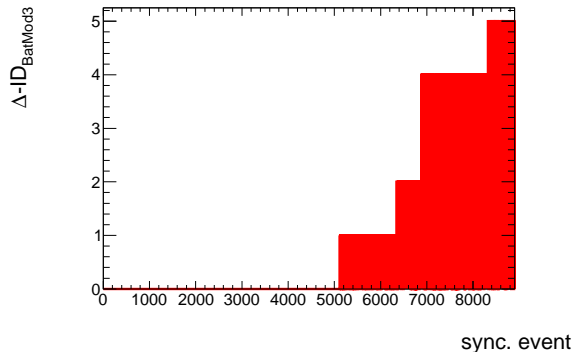
Figure 5.10.: Shift of the trigger-Δ-ID (Δ-ID) is plotted as a function of the synchronised event number for BatMod3 (data: run1830, November 2007).

5.3.2. Data Preparation for Conversion

To preprocess the data for EuTelescope for each readout pixel, the x- and y-position of the DUT and the proper ToT value are dumped in ROOT NTuples together with a device ID (for DUT: 10). The same four values are required for the telescope planes.

As the common EuTelescope software is only able to handle pixel detectors and no strip detectors, some EuTelescope-Processors had to be modified for the telescope data. Keeping the software changes minimal but at the same time providing the full access to the complete strip information, the four possible cluster types of the Bonn-ATLAS-Telescope (5×5, 5×6, 6×5 and 6×6 strips) will be delivered in the following semi-pixel-format.

For the telescope clusters the x- and y-positions of each strip intersection and the device ID are dumped in the same way as for the DUT (device ID for BatMod6: 0, for BatMod1: 1 for BatMod3: 2). The strip ToT will be dumped in a fixed correlation to the x- and y- positions. As

	x0	x1	x2	x3	x4	x5
y0	ToT of x0	ToT of x1	ToT of x2	ToT of x3	ToT of x4	ToT of x5
y1	-998	-999	-999	-999	-999	-999
y2	ToT of y0	ToT of y1	ToT of y2	ToT of y3	ToT of y4	-999
y3	-999	-999	-999	-999	-999	-999
y4	-999	-999	-999	-999	-999	-999

Figure 5.11.: Example for the handling of strip ToT information in a 6×5 telescope-cluster.

an example the fixed pattern for a 6×5 cluster is shown in Figure 5.11. The ToT information of the x-strips is saved in the first row (so in (x0,y0),(x1,y0),(x2,y0),(x3,y0),(x4,y0),(x5,y0). The ToT information of the y-strips is saved in the third row (and also in the fourth row for 5×6 clusters). Except "pixel" (x0,y1), which is filled with -998 for orientation and consistency checks, the rest of the "pixels" are filled with a default value -999.

5.3.3. BAT-Eudet Converter

A specially developed processor, the BAT-Eudet Converter, translates all pixel information (x-, y-position, ToT, device ID) of one run from a provided root NTuple in an LCIO format. LCIO (Linear Collider I/O) is the common framework and event data model for linear collider detector studies as the EUDET telescope was designed for ILC detector development.

5.3.4. Clustering Algorithm

In the EUTelClusteringProcessor the common clustering algorithm for zero suppressed data, the SparseCluster algorithm, is chosen. Direct neighbour pixels but also diagonally connected pixels are defined as clusters. As expected this algorithm defines exactly one cluster with the expected size of 5×5, 5×6, 6×5 or 6×6 strips in every telescope plane. The cluster sizes and cluster multiplicities in the DUT will be discussed in Section 6.3.

5.3.5. HitMaker

To reconstruct the x-y-position of the particle track in the telescope planes or the DUT the charge distribution within a cluster can be used in three different ways:

1. The easiest but also least precise way is the definition of the centre of the seed pixel as the hit position.

2. Another more precise option is the determination of the charge centre of gravity (CoG), which is the charge weighted average position.
   Caused by diffusion and an inhomogeneous electric field, the deposited charge within a cluster is not homogeneously distributed. The relation between charge sharing and actual hit position is not linear. Therefore the centre of the seed pixel is favoured when the hit position is reconstructed with the CoG-algorithm. This effect is illustrated in Figure 5.12. The physical charge distribution is plotted against the pixel position. As a simple model of a non-linear charge distribution a Gauss distribution is used. The actual hit position corresponds to the centre of the Gauss distribution. The measured charge per pixel is shown in red. Based on this distribution the CoG position is calculated. A significant discrepancy between CoG position and actual hit position occurs.
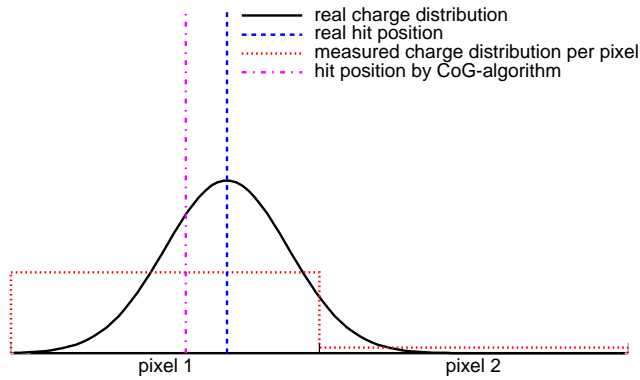
Figure 5.12.: Illustration of the discrepancy between the CoG position (vertical dotted pink line) and the real hit position (vertical dotted blue line).

3. To solve this non-linear discrepancy between the CoG and the actual hit position correction functions can be applied to the charge sharing information. One possibility is the eta-algorithm. Instead of using the whole cluster information, only the charge information of the seed pixel and the pixel with the second biggest charge is used. The eta-function is calculated for these clusters:

$$\eta = \frac{Q_{left}}{Q_{left} + Q_{right}}. \tag{5.2}$$

Q_{left} is the charge of the left pixel/strip, Q_{right} the charge of the right pixel/strip. The probability density $\rho_\eta(\eta)$ is calculated. The correction function $X(\eta)$ is supposed to map

η, so that the probability density is flat: $\rho_X(x) = 1$ and the conditions $X(\eta = 0) = 1$ and $X(\eta = 1) = 0$ are fulfilled. With respect to the normalisation condition of a probability density it follows:

$$1 = \int_0^1 \rho_\eta(\eta')d\eta' = \int_{x(\eta=0)}^{x(\eta=1)} \rho_\eta(\eta'(x')) \left|\frac{d\eta'}{dx'}\right| dx' = \int_1^0 \underbrace{\rho_X(x')}_{=1} dx' = -\int_0^1 dx' \quad (5.3)$$

$$\Rightarrow -1 = \left|\frac{d\eta'}{dx'}\right| \rho_\eta(\eta'(x')). \qquad (5.4)$$

$$(5.5)$$

The correction function is then:

$$X(\eta) = 1 - \int_0^\eta \rho_\eta(\eta')d\eta' = \int_\eta^1 \rho_\eta(\eta')d\eta'. \qquad (5.6)$$

$X(\eta) \in [0, 1]$ corresponds to the corrected hit position, where $X(\eta) = 0$ is the centre of the left pixel/strip and $X(\eta) = 1$ is the centre of the right pixel/strip.

In Figure 5.13 the eta-correction for a telescope plane is analysed. The probability density of eta $\rho_\eta(\eta)$ is shown in Figure 5.13(a). If $\eta \to 0$, almost all charge is deposited in the right strip; if $\eta \to 1$, almost all charge is deposited in the left strip. Since the telescope clusters have a size of at least 5×5 strips, there is always a seed strip and a neighbour strip with the second biggest charge. Unfortunately for a few events the charge of the neighbour strip with the second biggest charge is negative (because of pedestal subtraction). This cluster is interpreted as a single hit cluster with no charge sharing and has to be included in the probability density of η. It contributes half to the first and half to the last bin. In Figure 5.13(c) the eta-function is plotted in x- and y- direction. In Figure 5.13(d) the reconstructed hit position after eta-correction is shown. In comparison to Figure 5.13(c) the hits are reconstructed almost perfectly homogeneously. For the telescope plane the eta-correction performs great since there is almost always a neighbour strip with positive charge.

Figure 5.14 illustrates the performance of the eta-algorithm at the DUT. As only pixels over threshold are readout, many clusters are 1-hit-clusters[4] (cluster with only one pixel). In this case eta cannot be calculated. Especially in x-direction the cluster size is mainly one as the pixel is eight times larger (400 μm) than in y-direction. To fulfil the basic assumption that the pixel is homogeneously illuminated, these 1-hit-clusters have to be added to the eta-function as mentioned above: they contribute half to the first and half to the last bin of the eta-distribution. Caused by these 1-hit-clusters some pixel regions cannot be resolved as it is shown in Figure 5.14(f). Still this eta correction leads to a better resolution than the CoG-algorithm, see Section 6.1.2 and Table 6.3.

In addition to that, the eta algorithm permits a rough approximation of the charge spread. From Figure 5.14(f) it can be estimated that the pixel edge region where charge sharing occurs is circa 9 ± 2 μm. This result will be compared with theoretical predictions and further measurements in Section 6.3.3.

In the EUTelCalculateEtaProcessor this common eta function has been implemented. In the following the eta-algorithm is used. In Section 6.1.2 the performance will be compared with the

---

[4]Cluster sizes will be analysed in detail in Section 6.3.

(a)

(b)

(c)

(d)
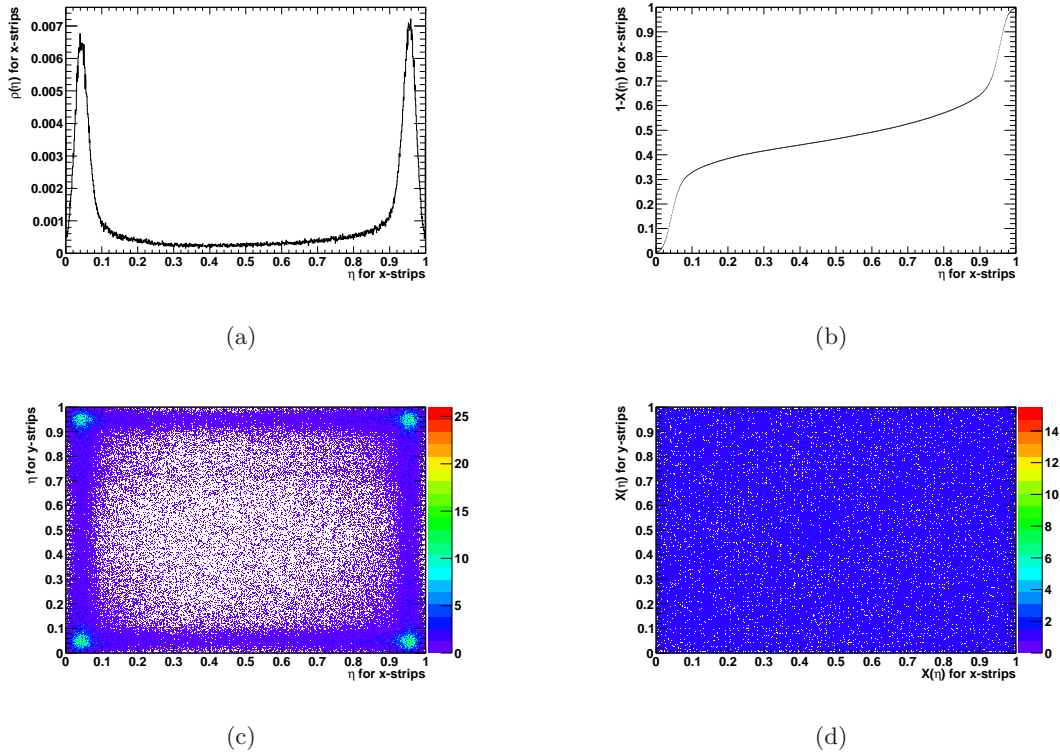
Figure 5.13.: (a) $\rho(\eta)$ for x-strips, (b) correction function $1-X(\eta)$, (c) two dimensional eta distribution, (d) hit distribution after correction (data: BatMod3, October 2006).

CoG-algorithm results.

The EUTelHitMakerProcessor calculates the hit position via CoG or eta-algorithm. These positions are finally transformed to a global coordinate system. For this, the local geometry of the telescope planes and the DUT is uploaded from a central configuration file, which is called gearfile.

5.3.6. Alignment

On the one hand the telescope planes and the DUT are manually mounted with a limited precision of circa ± 1 mm; on the other hand position resolutions in the order of μm should be studied. Therefore the exact positions of the devices must be determined from the data. This procedure is called the alignment, which is organised in a double stage process.
In a first iteration the telescope planes are aligned: the outer two modules are fixed whereas the x and y position and the rotation around the beam axis (z-axis) of the middle telescope plane are optimised. The DUT is excluded in this step.
In a second iteration all telescope planes are fixed and the x and y position and z-rotation of the DUT is optimised.
The complete alignment is accomplished with the EUTelMille processor. It prepares the data for the actual alignment program: MillipedeII [39]. Here the track data is grouped into local
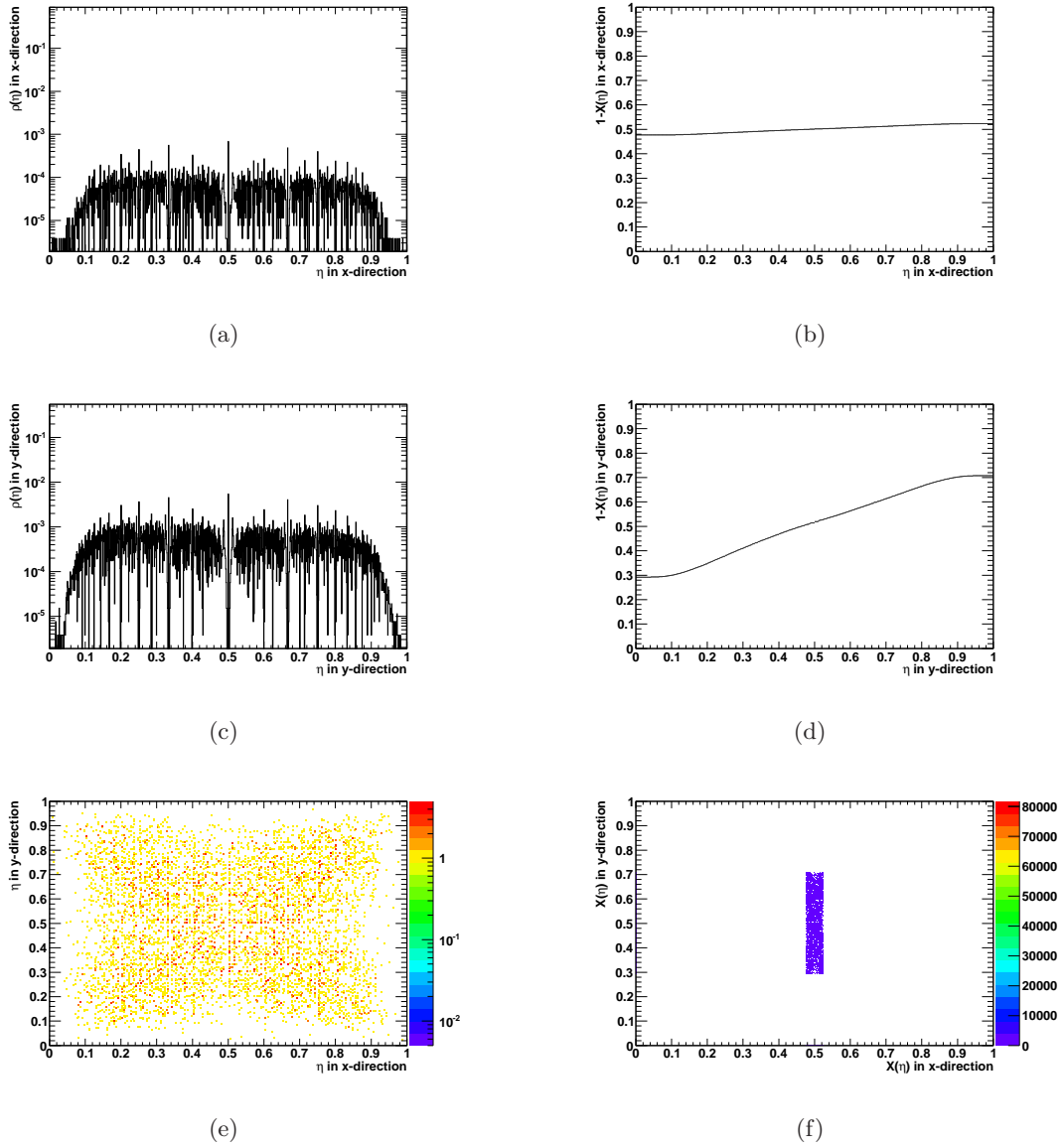
Figure 5.14.: DUT, October 2006: (a) $\rho(\eta)$ in x-direction, (b) correction function $1-X(\eta)$ in x-direction, (c) $\rho(\eta)$ in y-direction, (d) correction function $1-X(\eta)$ in y-direction, (c) two dimensional eta distribution, (d) hit distribution after correction.

and global parameters. Local parameters correspond to the local hit positions in the telescope planes and the DUT. Global parameters describe the global position of these devices, and thus correspond to the alignment constants. The linear least squares problem for the global parameters is solved by a simultaneous fit of all parameters.

The alignment constants for the various testbeam periods are listed in Table A.2.

5.3.7. Fitter

As a fitting processor the EUTelTestFitter was chosen, which also takes multiple scattering into account. For the track fitting, which is performed separately in XZ and YZ planes, only the hit information of the telescope planes is used. The fitted track position in each telescope plane is found by solving a matrix equation resulting from a χ^2 minimum condition.

The following approximations are done: all telescope planes are parallel orientated to each other, the incoming beam is perpendicular to the telescope planes, the incoming beam has a small angular spread, particle scattering angles in subsequent telescope layers are small, thicknesses of all material layers are very small compared to the distances between planes, particle energy losses in telescope layers can be neglected.

6. Testbeam Results

In this Chapter all testbeam results of CD181 will be presented and discussed. A special focus is placed on the analysis of radiation hardness by comparing measurements at different radiation fluence exposures.

Structure of this Chapter
The testbeam results presented in Section 6.1 - 6.5 require some background information which is introduced initially (Section 6.0). Next to some fundamental definitions the used testbeam data sets are summarised. In order to study homogeneously illuminated regions of the sensor, masks have to be applied. They are briefly motivated.
As a central quantity of a testbeam analysis the spatial resolution is determined via residual distributions in the beginning (Section 6.1). The unexpected accumulation of split-clusters is studied afterwards (Section 6.2). Their discovery solves known and until then not understood characteristics in the charge spectra as well as abnormal dynamics in the cluster sizes and cluster multiplicities. Analysing cluster sizes and spatial cluster distributions charge spread and thus charge sharing between neighbouring pixels are discussed in the third Section (Section 6.3). In addition, detection efficiency and noise are defined and determined (Section 6.4). In the last Section (Section 6.5) charge spectra and their dynamics are studied. Finally the damage coefficient is calculated which is the key quantity for the radiation hardness of the sensor material. Previously a new and more precise treatment of the ToT-charge calibration data is introduced.

In the subsequent Chapter 7, all results are summarised and compared with reference data. Some unexpected phenomena are interpreted by a rather unexplored model of polarisation which is caused by material defects.

6.0. Definitions

6.0.1. Basic Definitions

For all further discussions some basic definitions are essential:
Residual: A residual is defined as the distance between the reconstructed hit position in the DUT and the intersection point of the fitted trajectory and the DUT. Reconstructing the track with the space points of the telescope planes, but not the hit in the DUT itself, the residual is called unbiased.
Matched Hit: The DUT hit with the smallest residual, which fulfils the tolerance ranges x-residual < 400 μm and y-residual < 150 μm[1], is called a matched hit.
Matched Event: An event will be denominated as matched if a matched hit exists in the DUT.

---

[1]These cuts are also used in [34] and in the analysis software *tbmon* which is used in the 3D-pixel community as well as in the future diamond pixel community.

testbeam period:	HV: [V]	matched events:	fluence: [p cm^{-2}]
October 2006	25	14857	0
October 2006	50	8163	0
October 2006	100	178806	0
October 2006	200	52516	0
October 2006	300	75077	0
October 2006	400	223141	0
October 2006	500	15576	0
August 2007	400	5631	8.46×10^{13}
August 2007	800	5352	8.46×10^{13}
November 2007	100	11063	6.87×10^{14}
November 2007	400	56763	6.87×10^{14}
November 2007	600	13781	6.87×10^{14}
November 2007	800	141669	6.87×10^{14}
November 2007	1000	43567	6.87×10^{14}
July 2008	800	53666	6.87×10^{14}

Table 6.1.: Summary of the studied testbeam data. Information about the testbeam period, bias voltage, the number of matched events and the total fluence are listed.

6.0.2. Testbeam Data

Altogether the scCVD diamond tracking detector CD181 was tested in five different testbeam periods in the years 2006-2009. In October 2006 the single chip was studied in a first testbeam which was analysed by M. Mathes [34]. In a six hours irradiation at the CERN PS with 24 GeV/c protons and an intensity of $\sim 10^{13}$ p(rotons) cm^{-2}hr^{-1}, CD181 received a fluence of 8.46×10^{13} p cm^{-2} in June 2007. A second testbeam period of poor quality and statistics followed in August 2007 since the DUT was not placed in the centre of the beam. In September 2007 the diamond was irradiated a second and last time with 24 GeV/c protons and got a fluence of 6.02×10^{14} p cm^{-2} (in total: 6.87×10^{14} p cm^{-2}). A third testbeam period was accomplished in November 2007. In the following two years 2008 / 2009 two more testbeam periods were taken without further irradiation.

Due to an unexpected and significant performance degradation in 2009 (without further irradiation), the front-end and the complete metallisation were removed from the diamond. After some successful tests as a simple strip detector a new front-end-I3 was mounted, so that CD181 will be tested also in the future.

In Table 6.1 the analysed testbeam data is summarised[2]. The testbeam period, the bias voltage, the number of matched events and the total fluence are listed. A detailed overview including all run-numbers is attached in Table A.1.

6.0.3. Applied DUT Masks

For different reasons, some pixels are excluded from the analysis by masks:

---

[2]Available data which has not been studied: 1. In August 2007 runs at a bias voltage of 600 V are excluded as they only consist of 200 matched events due to the bad quality of the complete testbeam setup. 2. In July 2008 runs exist with different incidence angles at a bias voltage of 800 V which have not been analysed since EuTelescope cannot process angles yet. Data from June 2009 are worthless since there does not exist any correlation between the DUT and the telescope data even with systematic trigger shifts of ≤ 100 trigger IDs.

1. <u>Basic masks</u>: Since the applied trigger-scintillators do not cover the complete DUT, the outer regions of the DUT in general have a lower hit occupancy. Studying only homogeneously triggered regions of CD181, these pixels are excluded from the analysis. Furthermore some pixels do not show any hits as the front-end is not covered completely by the diamond, see especially the left sensor corner on Photo 4.1. A few insular pixels seem to be dead for unknown reasons as they do not hold any signal charge in any testbeam runs. To make sure that all these pixels and their effects on the nearest environment are not analysed, the two neighbouring pixels (100 μm) on both sides in y-direction are also excluded.

2. <u>Masks for special regions</u>: In November 2007 and July 2008, two adjacent regions with peculiar performance have been observed: In *special region I*, the hit occupancy is significantly increased whereas the hit occupancy in *special region II* is rather decreased. Furthermore these two special regions show various peculiar characteristics, see also Section 6.2.2, Figure 6.13. To analyse regions with rather uniform response, these two regions have been generously excluded.

(a) Hit map (data: October 2006, HV: 400 V)

(b) Hit map (data: August 2007, HV: 800 V)

(c) Hit map (data: November 2007, HV: 800 V)

(d) Hit map (data: July 2008, HV: 800 V)
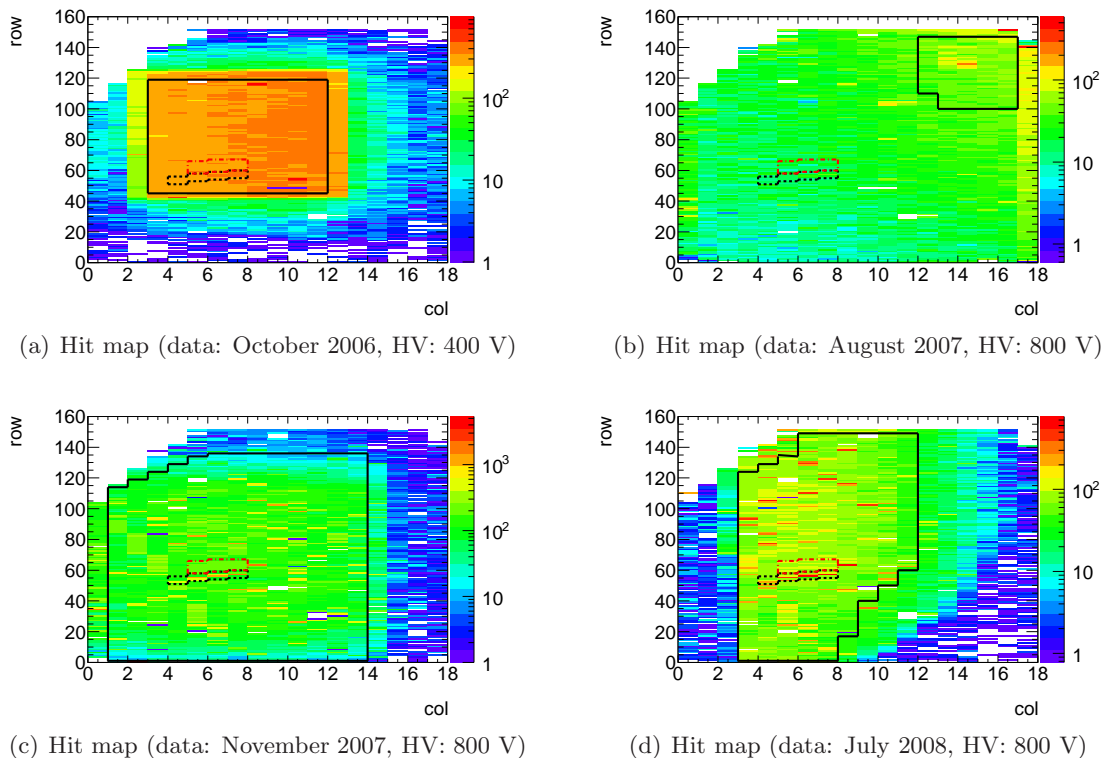
Figure 6.1.: Hit occupancy maps which show the CoG-pixels of all readout clusters are plotted for four different testbeam periods. The black boxes frame regions of accepted hit occupancy. The neighboured special regions I and II are indicated by a dotted, black box and by a dotted, red box.

In Figure 6.1 occupancy maps are plotted for four testbeam configurations: October 2006 at a bias voltage (HV) of 400 V and August 2007, November 2007 and July 2008 at a bias voltage

(a) Mask for October 2006

(b) Mask for August 2007

(c) Mask for November 2007

(d) Mask for July 2008
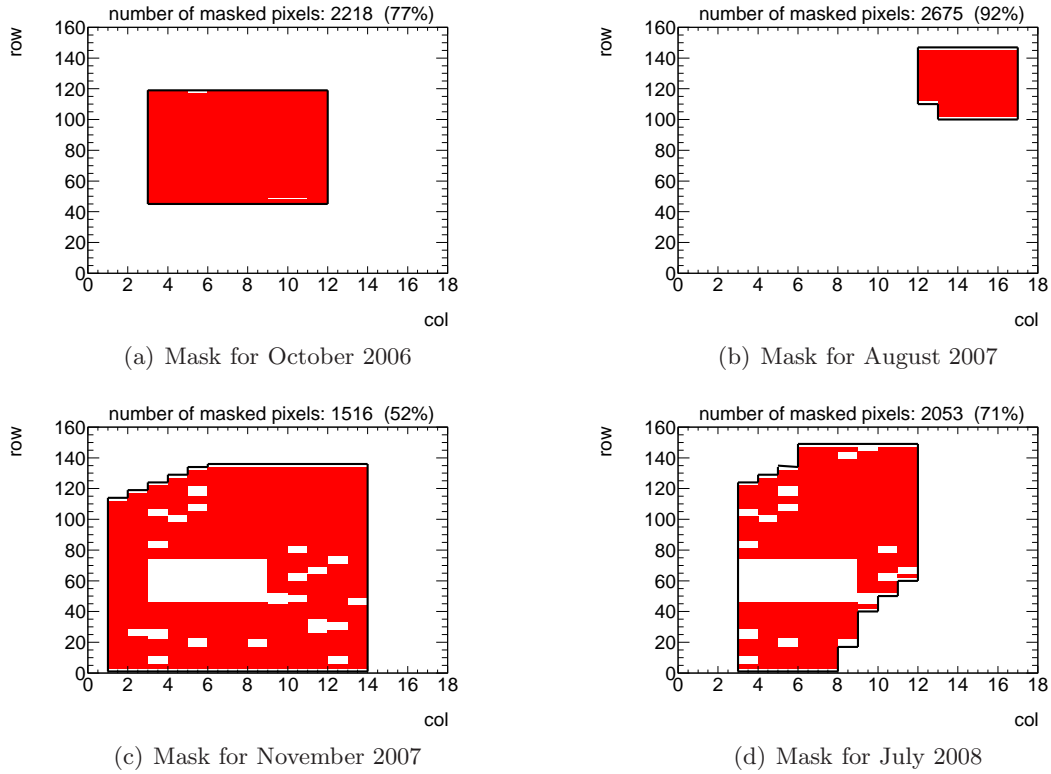
Figure 6.2.: Final masks for the different testbeams. Black boxes indicate regions of accepted hit occupancy. In (c) and (d) the special regions I and II are generously masked.

of 800 V. In these histograms pixels of all readout clusters are inserted if they hold the CoG position of the clusters (also called CoG-pixels). The regions with acceptable hit occupancy are framed by black boxes. The two special regions are indicated by black dotted boxes (special region I) and red dotted boxes (special region II).

Scintillators: In October 2006, the region which is covered by the scintillators is clearly visible whereas no scintillators are visible for August 2007. Here the DUT and the scintillators were deposited next to the beam. Only a small region in the top right sensor corner is accepted for further analysis. In July 2008 a third scintillator with a pinhole in the centre was used additionally. In comparison to the other two scintillators this scintillator operated in a veto mode, so that a circular region has been triggered. In Figure 6.1(d) a quarter of this circular region is observable.

In Figure 6.2 the final masks (basic masks + special region masks) are plotted for the various testbeam periods. As in August 2009 over 90% of all pixels have been excluded this testbeam period will not be analysed in detail. The special regions in November 2007 and July 2008 have been generously excluded.

6.1. Spatial Resolution

As mentioned before the unbiased residual discriminates between signal and noise hits in the DUT, where a signal hit corresponds to a matched hit and a noise hit to an unmatched hit. Next to this fundamental function the width of the unbiased residual distribution σ_{meas} defines the spatial resolution of the DUT. It is composed of the intrinsic DUT resolution σ_{DUT} and the interpolated track resolution σ_{tel} at the z-position of the DUT:

$$\sigma_{meas}^2 = \sigma_{DUT}^2 + \sigma_{tel}^2. \tag{6.1}$$

In the following two Sections the interpolated telescope resolution (Section 6.1.1) will be studied and afterwards the intrinsic DUT resolution (Section 6.1.2).

6.1.1. Telescope Resolution

The interpolated telescope resolution at the z-position of the DUT σ_{tel} can be determined with the knowledge of the intrinsic telescope plane resolutions σ_{plane} and the z-positions of the telescope planes z_i [40]. If the DUT is placed at $z = 0$ cm, and assuming that all telescope planes have the same intrinsic resolution, it follows:

$$\sigma_{tel}^2 = k \cdot \sigma_{plane}^2, \tag{6.2}$$

where k is a geometrical scaling factor:

$$k = \frac{\sum_{i=1}^{N} z_i^2}{N \cdot \sum_{i=1}^{N} z_i^2 - \left(\sum_{i=1}^{N} z_i\right)^2}, \tag{6.3}$$

and N is the number of telescope planes. The z-positions of the telescope planes and the DUT are summarised in Table A.3.

In the exact same manner the intrinsic telescope resolution σ_{plane} can be determined. Considering a telescope plane as DUT ($\sigma_{meas'}^2 = \sigma_{plane}^2 + \sigma_{tel'}^2$) and still assuming that the intrinsic telescope resolution is the same for all planes ($\sigma_{tel'}^2 = k' \cdot \sigma_{plane}^2$), it follows:

$$\sigma_{plane}^2 = \frac{\sigma_{meas'}^2}{1 + k'} \tag{6.4}$$

where $\sigma_{meas'}$ corresponds to the width of the unbiased residual distribution of a telescope plane at $z = 0$ cm. k' is the adjusted geometrical scaling factor.

Finally the interpolated telescope resolution at the z-position of the DUT is determined by the measurement of the unbiased residual distribution of a telescope plane:

$$\sigma_{tel}^2 = \frac{k}{1 + k'} \sigma_{meas'}^2. \tag{6.5}$$

Testing the hypothesis whether σ_{plane}^2 is equal for all telescope planes, Equation 6.5 is applied to the unbiased residual distributions of all three telescope planes separately. These distributions are plotted in Figure 6.3. Here the spatial resolutions $\sigma_{meas'}$ are defined as the RMS values of the residual distributions. The subsequent interpolated telescope resolutions σ_{tel} for all testbeam periods are summarised in Table 6.2. The significantly smaller interpolated track resolution of the unpaired plane[3] is not understood. The predicted telescope resolutions determined by

RMS: 14.969+/-0.019 μm
σ_plane: 9.872+/-0.012 μm
σ_telescope: 7.698+/-0.01 μm
k': 1.299
zPos: 0 mm

x-residual of BatMod6 [mm]

(a)

RMS: 14.727+/-0.019 μm
σ_plane: 9.712+/-0.012 μm
σ_telescope: 7.573+/-0.009 μm
k': 1.299
zPos: 0 mm

y-residual of BatMod6 [mm]

(b)

RMS: 13.222+/-0.017 μm
σ_plane: 9.872+/-0.012 μm
σ_telescope: 7.698+/-0.01 μm
k': 0.793
zPos: 31.176 mm

x-residual of BatMod1 [mm]

(c)

RMS: 13.008+/-0.016 μm
σ_plane: 9.712+/-0.012 μm
σ_telescope: 7.573+/-0.009 μm
k': 0.793
zPos: 31.176 mm

y-residual of BatMod1 [mm]

(d)

RMS: 102.619+/-0.135 μm
σ_plane: 8.94+/-0.011 μm
σ_telescope: 6.971+/-0.009 μm
k': 130.747
zPos: 267.176 mm

x-residual of BatMod3 [mm]

(e)

RMS: 104.563+/-0.137 μm
σ_plane: 9.109+/-0.011 μm
σ_telescope: 7.103+/-0.009 μm
k': 130.747
zPos: 267.176 mm

y-residual of BatMod3 [mm]

(f)

Figure 6.3.: Unbiased residual distributions of the telescope planes. The DUT is excluded (data: October 2006).

the paired planes diversify from 6.80 to 7.99 μm. To prevent the underestimation of the intrin-

---

[3] As in all testbeam periods only three telescope planes are used two (paired) planes are placed on one side of the DUT and the third (unpaired) plane on the other side of the DUT. The unpaired plane corresponds to BatMod3 in October 2006, August 2007, November 2007 and to BatMod6 in July 2008, see Table A.3.

testbeam period:	BatMod6		BatMod1		BatMod3	
	x:	y:	x:	y:	x:	y:
October 2006:	7.70	7.57	7.70	7.57	6.97	7.10
November 2007:	7.28	6.80	7.29	6.80	5.25	5.10
July 2008:	5.34	5.37	7.69	7.99	7.69	7.99

Table 6.2.: Interpolated telescope resolutions (σ_{tel}) at the z-position of the DUT in [μm].

sic DUT resolution: $\sigma_{DUT} = \sqrt{\sigma_{meas}^2 - \sigma_{tel}^2}$ the smallest interpolated telescope resolution of $\sigma_{tel} = 5.1\ \mu$m will be assumed in the following Sections.

Two more inaccuracies affect the measured resolution of the DUT and usually have to be considered:

1. **Multiple Scattering:** When the particle traverses the testbeam setup, multiple Coulomb interactions occur, which lead to small-angle scattering. An approximation for small angles Θ is given in [41]:

$$\Theta = \frac{13.6 MeV}{\beta cp} z \sqrt{x/X_0}\left[1 + 0.088 \log_{10}\left(x/X_0\right)\right] \qquad (6.6)$$

   where p, βc, and z correspond to the momentum, the velocity and the charge number of the beam particle and X_0 is the radiation length of the traversed material. As shown in [34] the maximal uncertainty caused by multiple scattering is $\approx 0.5\ \mu$m if the beam energy is bigger than 100 GeV and the telescope resolution is in the order of 8 μm.

2. **Alignment Error:** Already explained in Section 5.3.6 only the middle telescope plane is aligned while the positions of the outer two telescope planes are fixed during the telescope alignment procedure. The alignment errors are directly determined by Millipede and are listed in Table A.2. These errors strongly depend on the estimated plane resolutions inserted in the gear file. Since a broad error of 14.4 μm per strip has been assumed in advance, the errors of the alignment constants are generously estimated. In most cases the errors are smaller than 1 μm.

6.1.2. Intrinsic Resolution of the DUT

Next to the imprecision of the fit position due to the limited resolution of the telescope, multiple scattering and misalignment, the reconstructed hit position and thus the shape of the residual distribution in general depend on detector specific properties. The following quantities have an impact on the shape of the residual distribution: the weighting field, which is defined by the electric field configuration, and thus the pixel geometry as well as the charge spread due to diffusion and trapping, and finally the charge threshold. Various fit functions can be applied to reproduce the shape of the measured residual distribution:

1. In the first instance a Gaussian distribution is a proper approximation for the short pixel direction (50 μm), which is commonly used in the ATLAS pixel community.

2. Assuming a uniform distribution of charge collection and a Gaussian smeared telescope resolution, a convolution of a rectangle function and a Gaussian distribution (width: σ)

provides a proper residual model. This simple convolution can be expanded by an x-shift (x0) to be sensitive to DUT misalignment. In the studied advanced box fit an angle parameter (α) is also included, which allows an asymmetric residual distribution due to a possible asymmetric weighting field or an asymmetric track fitting. The advanced box fit is defined as:

$$\text{adv. box fit} = \frac{1}{2}\left(1 + \alpha(x - x0)\right) A \frac{\frac{1}{2}(1 + \text{Erf}(\frac{x+\text{width}-x0}{\sqrt{2}\sigma})) - \frac{1}{2}(1 + \text{Erf}(\frac{x-\text{width}-x0}{\sqrt{2}\sigma}))}{\text{width}} \quad (6.7)$$

where A is the area and *width* is the width of the rectangle function.

The width of the residual distribution, which is associated with the measured resolution σ_{meas}, can finally be characterised in three different ways:

1. In the first instance the RMS value of the residual distribution can be used.

2. A further estimator is the full width at half maximum (FWHM) of the advanced box fit.

3. In addition σ_{Gauss} is studied for the short pixel direction since it is commonly used in the ATLAS pixel community.

The RMS value as well as the FWHM are proper but different estimators for the width of a box-like distribution. By construction these quantities are not directly comparable, since the FWHM of a box fit is only sensitive to the positions of the box-shoulders, whereas the RMS value also considers the positions of the measurement points within the bulk region of the box distribution. To illustrate the difference between the RMS value and the FWHM an example box distribution is inserted in the Appendix, see Figure A.2. In the following analysis FWHM values will be listed, but only RMS (x-direction) and σ_{Gauss} (y-direction) values are analysed in detail.

Before the resolutions of the different testbeams will be discussed two special aspects are briefly studied: 1. The performances of the different hit-reconstruction algorithms (CoG-algorithm and eta-algorithm) are compared. 2. The theoretically predicted resolutions of a simple detector model are analysed.

Analysis of the Hit-Reconstruction Algorithms (CoG- and Eta-Algorithm)

Exemplary for the performances of the CoG- and eta-algorithm the residual distributions of these two hit-reconstruction algorithms are plotted in Figure 6.4 for the testbeam period October 2006 at a bias voltage of 400 V. The contributions of 1-hit-clusters and 2-hit-clusters are plotted in addition[4]. The eight peaks in the x-residual distribution and the asymmetric shape of the 1-hit-cluster y-residual distribution are analysed below. In this Subsection only the differences between the two algorithms are discussed.
By construction, the 1-hit-cluster distribution is identical for both algorithms. As expected the 2-hit-cluster distribution in x-direction is significantly narrower with the eta-algorithm than with the CoG-algorithm. This eta-effect is responsible for the central peak in the residual distribution of all cluster sizes. Also in y-direction the 2-hit-clusters have a narrower residual distribution if

---

[4]As in every further residual plot, a 2-hit-cluster in the x- (or y-) residual distribution is defined as two neighbouring readout pixels in x- (or y-) direction and exactly one readout pixel in y- (or x-) direction. So only straight, 1-dimensional clusters and no diagonal, L-shape or other 2-dimensional clusters are considered in these distributions. Analogue definitions exist for 3-, 4-, 5-hit clusters.
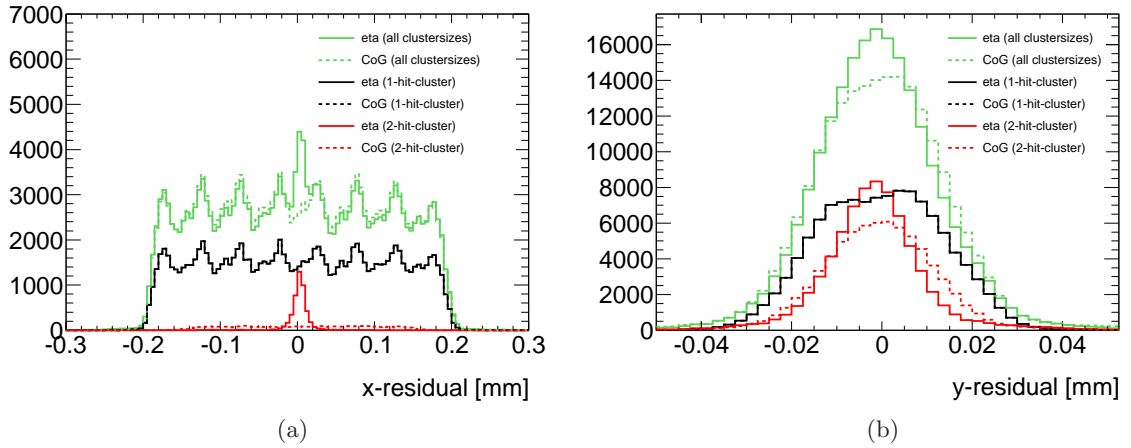
Figure 6.4.: Comparison between the eta- and CoG-algorithm (data: October 2006, HV: 400 V).

the eta-algorithm is applied. The relative residual shift in Figure 6.4(b) is not understood.
In Table 6.3 the widths of the residual distributions, calculated with the eta- and the CoG-algorithm, are listed for the different testbeam configurations. Here the resolution for the x-direction is simply characterised by the RMS value. In y-direction the resolution is analysed by

testbeam period, HV:	x-residuals: [μm]		y-residuals: [μm]	
	RMS$_{eta}$:	RMS$_{CoG}$:	$\sigma_{Gauss eta}$:	$\sigma_{Gauss CoG}$:
October 2006, 25 V	110.2 ± 0.7	109.3 ± 0.7	16.0 ± 0.2	16.3 ± 0.2
October 2006, 50 V	108.3 ± 0.9	106.9 ± 0.9	14.9 ± 0.2	15.8 ± 0.2
October 2006, 100 V	107.4 ± 0.2	107.8 ± 0.2	14.0 ± 0.1	14.5 ± 0.1
October 2006, 200 V	108.5 ± 0.4	109.1 ± 0.4	12.7 ± 0.1	13.4 ± 0.1
October 2006, 300 V	109.0 ± 0.3	109.2 ± 0.3	12.8 ± 0.1	13.5 ± 0.1
October 2006, 400 V	109.6 ± 0.2	109.9 ± 0.2	13.0 ± 0.1	13.7 ± 0.1
October 2006, 500 V	109.6 ± 0.7	110.2 ± 0.7	12.4 ± 0.1	12.9 ± 0.1
August 2007, 400 V	112.3 ± 1.2	109.6 ± 1.2	22.5 ± 0.4	23.3 ± 0.4
August 2007, 800 V	113.6 ± 1.3	111.2 ± 1.3	22.5 ± 0.4	23.5 ± 0.5
November 2007, 100 V	116.7 ± 0.9	116.0 ± 0.8	18.5 ± 0.2	18.6 ± 0.2
November 2007, 400 V	115.5 ± 0.4	111.0 ± 0.4	21.1 ± 0.2	24.0 ± 0.2
November 2007, 600 V	115.0 ± 0.8	108.6 ± 0.7	27.5 ± 0.4	33.8 ± 0.7
November 2007, 800 V	123.0 ± 0.3	115.1 ± 0.3	32.3 ± 0.2	50.6 ± 0.7
November 2007, 1000 V	122.7 ± 0.5	113.9 ± 0.5	35.1 ± 0.5	52.8 ± 1.3
July 2008, 800 V	115.2 ± 0.4	109.3 ± 0.4	22.7 ± 0.2	25.6 ± 0.2

Table 6.3.: Comparison between eta- and CoG-algorithm.

σ_{Gauss} which is commonly used by the ATLAS pixel community.
In the short pixel direction the eta-algorithm generally improves the resolution in comparison to the CoG-algorithm. For the unirradiated testbeam configurations in October 2006 with

saturated charge collection (100 V-500 V)[5] the resolutions do not improve significantly (circa 0.5 μm). For the irradiated testbeam configurations in November 2007 with saturated charge collection (400 V-1000 V) the eta-correction has a bigger effect. This might be due to the decrease of 1-hit-clusters: $50 - 60\%$ in October 2006 and only $20 - 30\%$ in November 2007, see Section 6.3.

Focusing on the resolution in the long pixel direction the CoG-algorithm performs similarly or even better than the eta-algorithm. This unexpected effect is probably caused by the non-negligible fraction of diagonal clusters in comparison to the direct neighbour pixels generating a cluster[6]. In this case the eta-algorithm is not the proper algorithm as only direct neighbour pixels are taken into account.

Comparison between the resolutions of 1-hit-clusters and theoretically predicted resolutions

Neglecting charge spread and therefore also charge sharing between two pixels and assuming a uniform hit distribution (probability density: $\rho(x) = 1/d$ for $|x| < d/2$), a theoretical resolution can be calculated:

$$\sigma = \sqrt{<x^2> - <x>^2} = \sqrt{\frac{1}{d} \int_{-d/2}^{d/2} x^2 dx - \left(\frac{1}{d}\int_{-d/2}^{d/2} x dx\right)^2} = \frac{d}{\sqrt{12}}. \qquad (6.8)$$

where d is the pixel pitch. For ATLAS pixels we expect $\sigma = 115.5$ μm in x-direction and

testbeam period, HV:	x-residual: [μm] RMS:	y-residual: [μm] σ_{Gauss}:
October 2006, 25 V	113.5 ± 1.0	14.5 ± 0.1
October 2006, 50 V	110.0 ± 1.4	13.2 ± 0.2
October 2006, 100 V	109.8 ± 0.4	13.8 ± 0.1
October 2006, 200 V	110.1 ± 0.5	13.3 ± 0.1
October 2006, 300 V	110.1 ± 0.5	13.1 ± 0.1
October 2006, 400 V	110.9 ± 0.3	13.3 ± 0.1
October 2006, 500 V	111.5 ± 0.9	12.4 ± 0.1
August 2007, 400 V	112.2 ± 1.8	20.8 ± 0.5
August 2007, 800 V	114.6 ± 2.0	20.9 ± 0.5
November 2007, 100 V	116.5 ± 0.9	17.2 ± 0.2
November 2007, 400 V	117.5 ± 0.7	16.8 ± 0.2
November 2007, 600 V	116.3 ± 1.6	18.0 ± 0.3
November 2007, 800 V	125.9 ± 0.6	21.1 ± 0.2
November 2007, 1000 V	125.9 ± 1.1	21.7 ± 0.3
July 2008, 800 V	113.9 ± 0.7	17.7 ± 0.2

Table 6.4.: Summary of all measured resolutions for 1-hit-clusters, which are compared with theoretically motivated values.

$\sigma = 14.4$ μm in y-direction. Clusters containing only one pixel (1-hit-clusters) approximately

---

[5]Saturation of the charge collection will be analysed in Section 6.5.2.

[6]In the short pixel direction the contribution of diagonal clusters is negligible in comparison to the contribution of direct neighbour pixels.

fulfil these assumptions. For these 1-hit-clusters the intrinsic resolution should be even smaller than $d/\sqrt{12}$, as in the pixel border regions their probability density $\rho(x)$ is less than $1/d$ due to charge sharing. In Table 6.4 the widths of 1-hit-cluster residual distributions are summarised. As explained before, the RMS value is quoted for the x-direction and σ_{Gauss} for the y-direction. Comparing theoretically predicted resolutions with the intrinsic DUT resolutions of 1-hit-clusters[7] the results of the first testbeam period (October 2006) are in good agreement whereas the measured resolutions for later testbeam periods differ significantly. To analyse the reasons for the resolution degradation in detail, the performance of the first testbeam period and the later testbeam periods will be studied separately.

General Analysis of the DUT resolution

As the central result of this Section all introduced estimators for the width of an unbiased residual distribution are listed in Table 6.5 for all testbeam configurations[8]. Due to the complexity

testbeam period, HV:	x-residuals: [μm]		y-residuals: [μm]		
	RMS:	FWHM$_{\text{box}}$/2 :	RMS:	FWHM$_{\text{box}}$/2 :	σ_{Gauss} :
October 2006, 25 V	110.2 ± 0.7	192.6	16.3 ± 0.1	18.9	16.0 ± 0.2
October 2006, 50 V	108.3 ± 0.9	190.7	15.7 ± 0.2	17.7	14.9 ± 0.2
October 2006, 100 V	107.4 ± 0.2	189.1	14.4 ± 0.1	16.5	14.0 ± 0.1
October 2006, 200 V	108.5 ± 0.4	190.1	13.2 ± 0.1	15.1	12.7 ± 0.1
October 2006, 300 V	109 ± 0.3	190.9	13.4 ± 0.1	15.1	12.8 ± 0.1
October 2006, 400 V	109.6 ± 0.2	191.5	13.5 ± 0.1	15.3	13.0 ± 0.1
October 2006, 500 V	109.6 ± 0.7	191	12.8 ± 0.1	14.6	12.4 ± 0.1
August 2007, 400 V	112.3 ± 1.2	185.8	33.1 ± 0.4	26.6	22.5 ± 0.4
August 2007, 800 V	113.6 ± 1.3	183.8	37.8 ± 0.5	26.9	22.5 ± 0.4
November 2007, 100 V	116.7 ± 0.9	188.7	33.5 ± 0.3	21.9	18.5 ± 0.2
November 2007, 400 V	115.5 ± 0.4	188.9	33.3 ± 0.2	24.9	21.1 ± 0.2
November 2007, 600 V	115 ± 0.8	185.1	38.4 ± 0.3	33.7	27.5 ± 0.4
November 2007, 800 V	123 ± 0.3	188.7	47.5 ± 0.2	38.3	32.3 ± 0.2
November 2007, 1000 V	122.7 ± 0.5	186.5	49.9 ± 0.2	42.0	35.1 ± 0.5
July 2008, 800 V	115.2 ± 0.4	187.3	34.3 ± 0.2	26.9	22.7 ± 0.2

Table 6.5.: Summary of all resolution estimators (RMS, FWHM and σ_{Gauss}) of all testbeam configurations.

of these results the unirradiated testbeam period will be studied first with a detailed focus on the shape of the residual distribution. Afterwards the residual trends of the irradiated testbeam periods will be analysed separately.

Testbeam period before irradiation (October 2006)
In Figure 6.5 the unbiased residual distributions in x- and y-direction are plotted for October 2006 at a bias voltage of 400 V. Similar to Figure 6.4 the residual distributions are subdivided in different cluster sizes.

---

[7]A telescope resolution of approximately 5.1 μm has to be subtracted quadratically from the measured resolutions, see Section 6.1.1.

[8]In the complete analysis about residual distributions and spatial resolutions, events with split-clusters, which will be introduced in the next Section 6.2, are excluded.
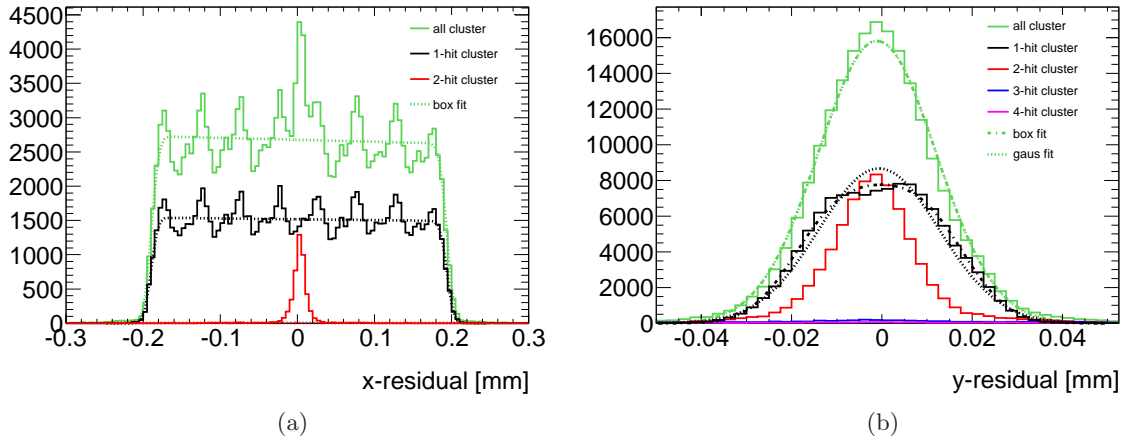
Figure 6.5.: Unbiased residual distributions in (a) x- and (b) y-direction (data: October 2006, HV: 400 V).

Noticeable and unexpected are the substructures, e.g. the eight peaks in x-direction and the sloped plateau in the 1-hit-cluster distribution in y-direction. Since the x-residual distributions
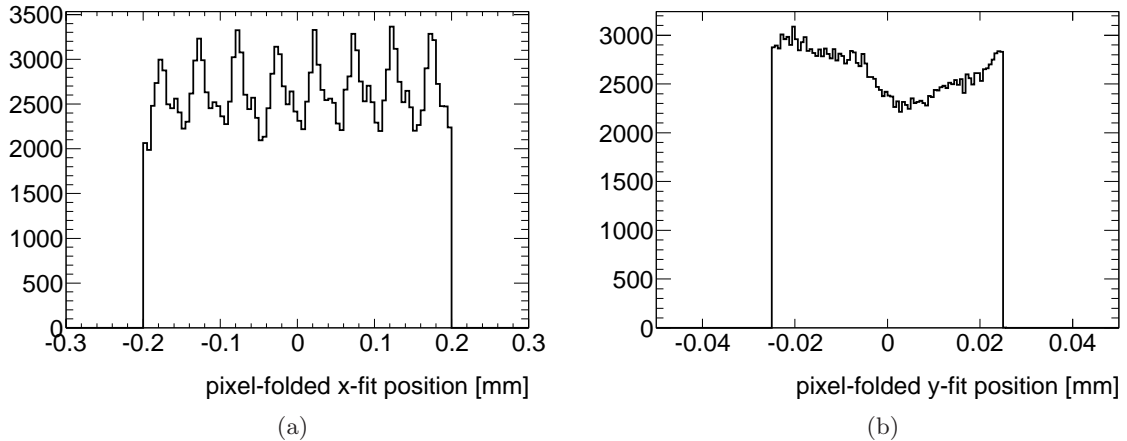
Figure 6.6.: Pixel-folded fit position in (a) x-direction and (b) y-direction at the z-position of the DUT (data: October 2006, HV: 400 V).

of the 1-hit-clusters, which are automatically reconstructed in the centre of the pixel, show the same substructures as the x-residual distribution of all cluster sizes, these peaks must be generated by a systematically inaccurate track reconstruction and not by the DUT hit-reconstruction. The periodicity of this inaccurate track reconstruction is only possible since the telescope pitch of 50 μm in x- and y-direction is a multiple of the DUT pixel pitches, and at the same time the telescope strips and the DUT pixels are approximately parallel orientated. Due to the similar pixel and strip geometry and orientation the fitted track position in the DUT can be plotted modulo the integral pixel position to analyse the periodically inaccurate track reconstruction.

These pixel-folded track positions are shown in Figure 6.6. The substructures in general and even the asymmetric shape of the individual peaks are recognised.

This systematically incorrect track reconstruction is probably caused by 1-hit-clusters in the telescope planes where no eta-correction can be applied, and the hit is reconstructed in the centre of the strip. These 1-hit-clusters have a significant impact on the wrong reconstruction if they occur in the unpaired telescope plane. A fourth plane which is placed next to the unpaired telescope plane would correct this effect, see residuals in [34].

Since the eta-correction only effects clusters with more than one readout pixel, the resolution of 2-hit-clusters is significantly better than the resolution of 1-hit-clusters. For example at 400 V the measured resolution can be expressed by σ_{Gauss} for the various cluster sizes: $\sigma_{Gauss} = 13.31 \pm 0.03$ μm for 1-hit-clusters, $\sigma_{Gauss} = 9.17 \pm 0.04$ μm for 2-hit-clusters.

Testbeam periods after irradiation (November 2007, July 2008)[9]

In this Section a special focus is placed on the unbiased residual distributions of the short pixel direction at different fluences. As before σ_{Gauss} is associated with the measured spatial y-resolution since it is the commonly used estimator in the ATLAS pixel community. In Figure
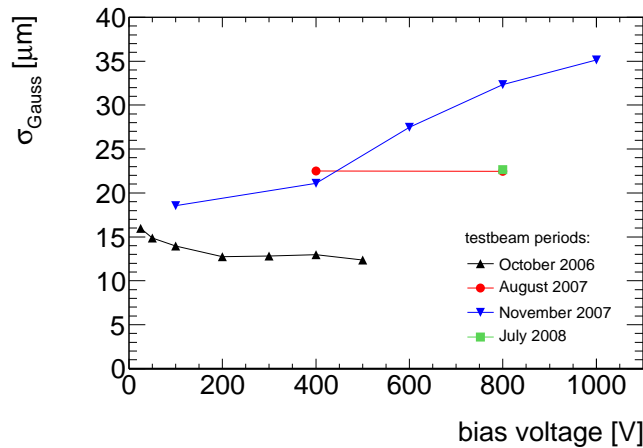
Figure 6.7.: σ_{Gauss} of the short pixel side is plotted as a function of the bias voltage for the different testbeam periods. Statistical errors are inserted.

6.7 σ_{Gauss} is plotted as a function of the bias voltage for all testbeam periods. Statistical errors are inserted in the plot; due to the scaling, they are not visible.

For the irradiated testbeam periods the y-residuals strongly depend on the bias voltage and significantly exceed the theoretical upper limit of 14.4 μm. In contrast to the testbeam period in October 2006, the smallest y-resolutions occur at the lowest bias voltage. In first instance a model can be considered where the resolution decreases with increasing bias voltage: if the electric field strength increases, the charge spread decreases since the signal charges are collected faster and the impact of diffusion is diminished. In general, more signal charge is collected on the actual readout pixels, which causes a more precise hit reconstruction. This model only works for the unirradiated testbeam period. For example the y-residual at a bias voltage of 400 V is

---

[9]The determined resolutions of the testbeam period August 2007 will not be studied in detail because of low statistics and a bad testbeam setup, see Table 6.1 and Section 6.0.2.

8.1 μm bigger in November 2007 than in October 2006. For higher bias voltage the residuals even worsen in November 2007.

Comparing October 2006 and November 2007, two fundamental aspects can cause the general degradation of the residuals:

1. The track reconstruction including alignment and telescope resolution became worse.

2. The intrinsic resolution of the DUT became worse by radiation damage (or other damage).

The first reason can be invalidated by comparing the summed squared biased residuals of the telescope planes determined by the used track fit. This quantity corresponds to the x-/y-χ^2 of the track fit but does not specify the error ($\sigma = 1$). In Figure 6.8(a) the normalised distributions of the summed squared biased residuals of the telescope planes are plotted. As this quantity
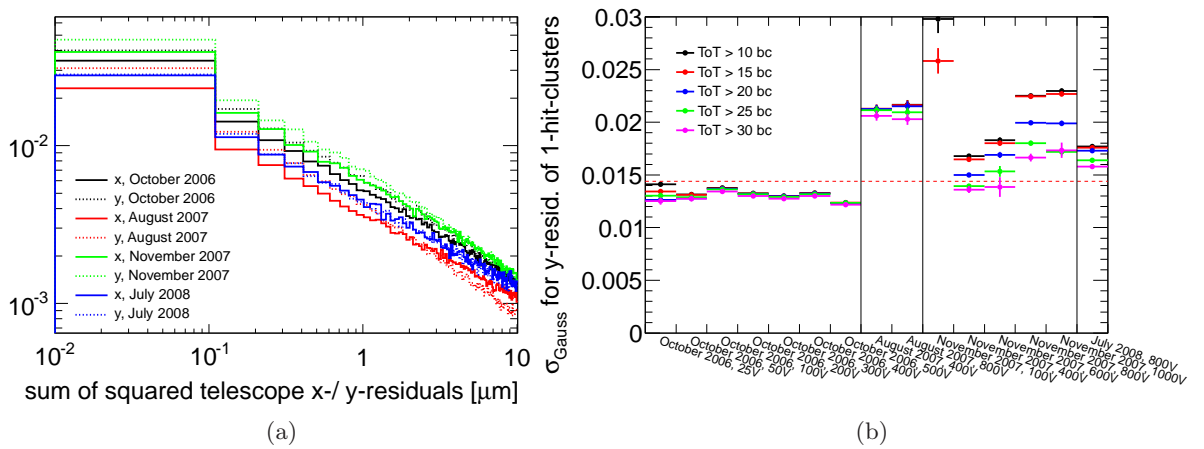
Figure 6.8.: (a) Normalised distributions of the summed squared biased x- / y-residuals of the telescope planes, (b) σ_{Gauss} for y-residuals of 1-hit-clusters as a function of the testbeam configuration for different ToT-cuts.

is smaller for November 2007 than for October 2006 the track reconstruction has even been improved.

So the DUT hit reconstruction itself has to be responsible for the degradation of the y-residuals. For the testbeam period November 2007 and July 2008 the detailed y-residuals are plotted in Figure A.1 in the same way as already shown for October 2006 (HV: 400 V) in Figure 6.5. At a bias voltage of at least 600 V the residual distributions of 2-hit-clusters contain a substructure with two peaks which are caused by an unexpected charge sharing. This surprising effect generates bigger residuals for 2-hit-clusters than for 1-hit-clusters. To illustrate the substructure, the residual distributions of the testbeam configuration November 2007 at a bias voltage of 800 V are plotted in Figure 6.9.

It is also remarkable that for the irradiated testbeam configurations the resolution strongly depends on the amount of collected charge. Excluding the exotic distributions of the 2-hit-cluster residuals, only the 1-hit-cluster resolutions (σ_{Gauss}) are plotted in Figure 6.8(b) for the different testbeam configurations. Here various minimal ToT cuts are applied. It is illustrated that after irradiation resolution improves significantly with higher collected charge. This observeration strengthens the hypothesis that the resolution degrades with charge trapping or recombination.
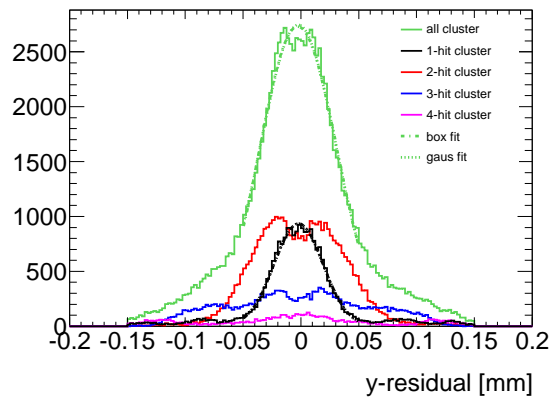
Figure 6.9.: Unbiased y-residual distributions (data: November 2007, HV: 800 V).

The possible mechanism (polarisation) will be explained in Section 7.2.1.

Curiously enough, the residual distributions in July 2008 are narrower than in November 2007 at the same bias voltage of 800 V and at the same fluence (see again Table 6.5). As in November 2007 the different testbeam configurations were recorded in the order of increasing bias voltage, the simultaneous broadening of the residuals might be a dynamic effect correlated to the much longer operating time.

Dynamics of the Residual Distributions

Analysing the resolution dynamics in Figure 6.10, the RMS values of the y-residual distributions are plotted as a function of the run-number for testbeam configurations with a significant amount of different runs. The run-number is used since the exact time is not known for October 2006, August 2007 and November 2007. For the unirradiated testbeam configuration (October 2006, 400 V) the resolution is constant over time. For the irradiated testbeam periods the resolutions worsen with operating time. A saturation of this effect is visible. The fluctuations of these values increase with decreasing statistics; in October 2006 a run contains roughly 25000 events whereas in July 2008 a run contains 5000 events.

Summary

As many different aspects concerning the unbiased residual distributions have been discussed the most important results are briefly summarised.

For the unirradiated testbeam period measured resolutions of circa 110 μm in x-direction and circa $12 - 14$ μm in y-direction have been measured which agree with the theoretically predicted values. The reason for the unexpected periodical substructures in the residual distributions is solved by a periodically incorrect track reconstruction due to an insufficient telescope setup of only three detector planes.

For the irradiated testbeam periods the measured resolutions degrade significantly ($115 - 125$ μm in x-direction and $18 - 35$ μm in y-direction). In addition the irradiated testbeam periods show unexpected behaviour in the 2-hit-cluster distribution (2-peak structure), in dependence of the bias voltage and in dependence of the operation time (increasing and saturating resolutions).

Some of these effects will be discussed again in Chapter 7, together with the phenomena which

(a) October 2006, HV: 400 V.

(b) November 2007, HV: 400 V.

(c) November 2007, HV: 800 V.

(d) July 2008, HV: 800 V.
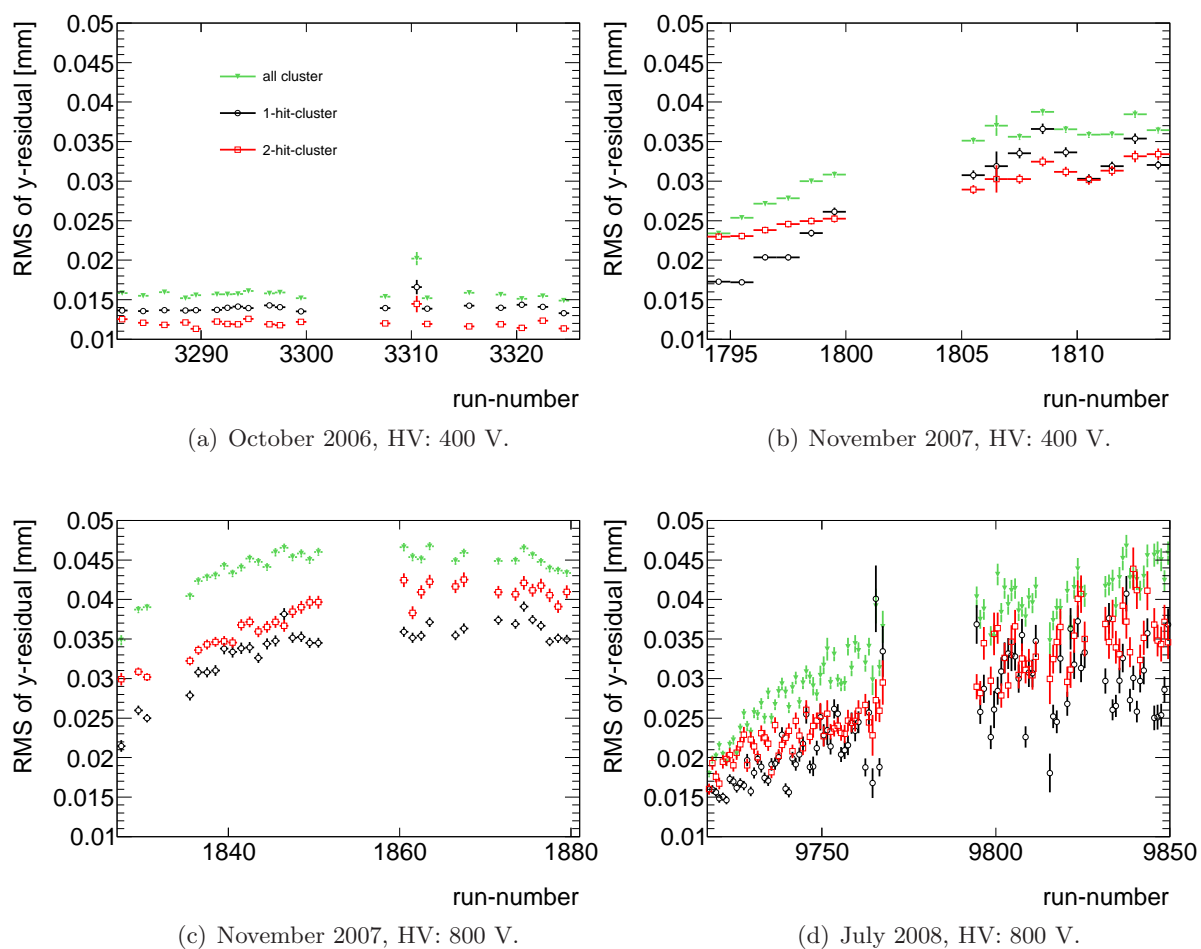
Figure 6.10.: Y-residual trends of various testbeam configurations: The RMS values of the y-residuals are plotted as a function of the run-number.

will be introduced in the next Sections.

6.2. Split-Cluster

6.2.1. Motivation and Definitions

Starting point for an extensive split-cluster analysis was the study of events with more than one readout cluster in the DUT. In this context the cluster distance between the reconstructed hit positions of the matched cluster and the cluster, which is closest to the matched cluster, was analysed. The normalised distribution of these so called minimal distances is plotted in Figure 6.11(a) together with a simulated distribution shown in red.

<u>Simulated Distribution</u>: In the simulation the positions of two homogeneously distributed clusters, a matched cluster and a second cluster, have been generated. Assuming two uncorrelated clusters, their positions are uniformly distributed over a typical ATLAS single chip pixel layout. Pixels which do not show any hits in the data set, as for example the uncovered top left corner of the front-end, are also excluded from simulation. In this Section the masks for the special regions are not applied to the data and the simulation since a connected pixel region is essential for this analysis.

In Figure 6.11(b) the lower range of these minimal distance distributions is zoomed into. In
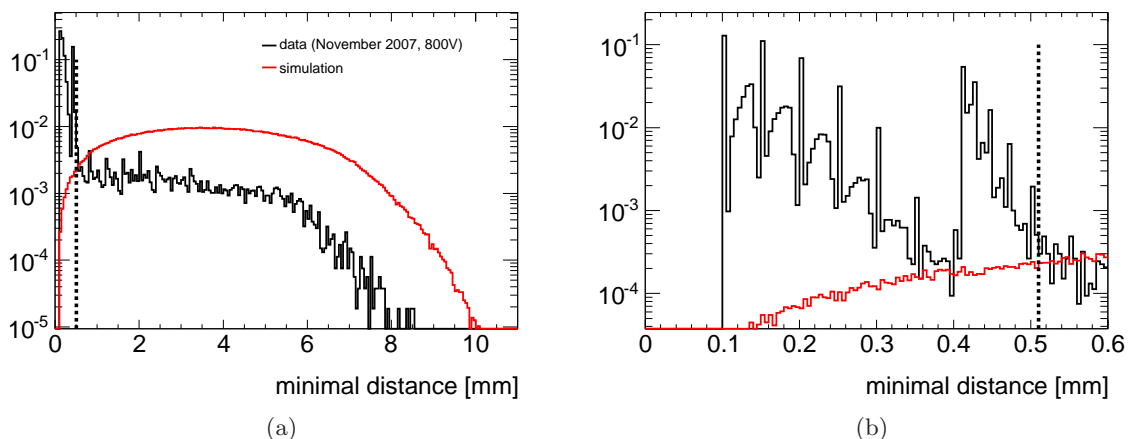
Figure 6.11.: (a) Measured and simulated normalised distributions of the distance between the hit position of the matched cluster and the nearest hit, (b) magnification of these distributions (data: November 2007, HV: 800 V).

this range an enormous discrepancy between data and simulation exists. Due to the cluster definition, where all neighboured and diagonal readout pixels are combined to one cluster, there are no entries for a minimal distance smaller than 100 μm. In contrast to the simulation, the position of the second cluster is highly concentrated around the position of the matched cluster. For this reason clusters with a minimal distance of less than a certain cut value will be tested in the following if they can be interpreted as a split-cluster. A cut value of 510 μm is chosen due to the significant discrepancy between data and simulation below this value.

In Figure 6.12 a split-cluster candidate is illustrated. The matched cluster which in this context is called a matched-partner-cluster is shown in green. The blue cross indicates the fitted track position. The second cluster which will be called split-partner-cluster is plotted in red. Finally a black line connects the reconstructed hit positions indicating the minimal distance. A
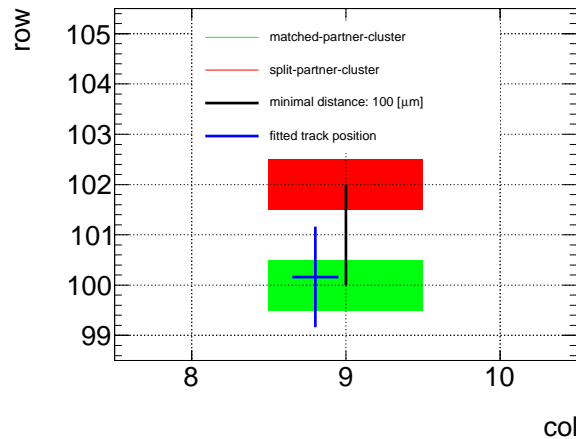
Figure 6.12.: Split-cluster example: A green pixel indicates the matched-partner-cluster, a red pixel corresponds to the split-partner-cluster. The blue cross denotes the fitted track position and the black line the distance between the reconstructed hit positions.

matched-partner-cluster and a split-partner-cluster together define a split-cluster.

In the following possible reasons for split-clusters are discussed. Finally some known problems are introduced which will be solved by the adoption of split-clusters.

6.2.2. Possible Reasons for Split-Clusters

In Figure 6.13 the spatial distribution of split-clusters is analysed. In Figure (a) and (b) the hit-positions of the matched-partner-clusters and the split-partner-clusters are plotted. Analogue to Figure 6.1 a black box indicates the basic mask and a black- and a red-dotted box illustrate special region I and II. These boxes only denote these regions since no masks have been applied in this Section.

Next to the observation that split-clusters occur over the whole sensor, it is conspicuous that in special region II there is a high concentration of matched-partner-clusters whereas in the neighbouring special region I there is a high concentration of split-partner-clusters. This might indicate an elongated defect in the sensor material. As a reference plot the hit map of all matched clusters which do not belong to split-clusters is shown in Figure 6.13(c).

Finally, a map of all *missed* pixels is plotted in Figure 6.13(d). Pixels between the matched-partner-cluster and the split-partner-cluster are called *missed* if both clusters have a cluster size of one in x-direction and are located in the same pixel column. An example for a missed pixel is pixel $(9, 101)$ in Figure 6.12. In map 6.13(d) it is shown that missed pixels and thus split-clusters are distributed over the whole sensor. A gradient with increasing concentration on the bottom side can be observed, which is not understood. In addition, a high concentration of missed pixels exists between the two special regions, which is in agreement with the observations in Figure 6.13 (a) and (b).

Two models for the origin of split-clusters are considered:
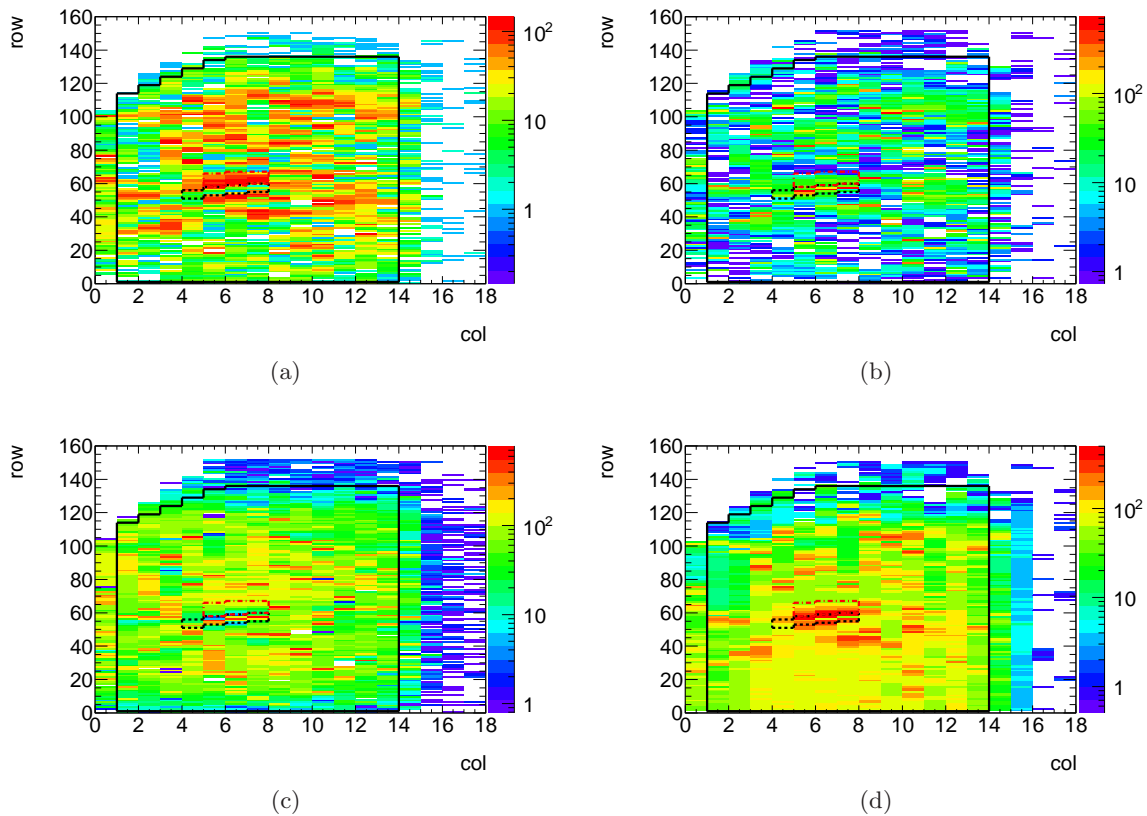
Figure 6.13.: (a) Hit map of matched-partner-clusters, (b) hit map of split-partner-clusters, (c) hit map of all matched clusters which are not matched-partner-clusters (as reference), (d) map of missed pixels (data: November 2007, HV: 800 V).

1. **δ-electrons:** These are electrons, generated by the beam particles via ionisation, which carry a significant fraction of energy to perform their own ionisation. In that way energy can be deposited away from the particle track. In a split-cluster the matched-partner-cluster would correspond to the region of the beam particle passage; the split-partner-cluster would belong to the path of the δ-electron. Between these two regions some pixels would fail the charge threshold.

2. **charge trapping:** As it will be explained in Section 6.3.3, charge spread is expanded by trapping. In this case the collected charge is spread over more pixels, and the collected charge per pixel is reduced, so that some pixels might fail their charge threshold.

The majority of observations which will be discussed in the following disproves the δ-electron hypothesis and strengthens the trapping hypothesis.

In Figure 6.14(a) the fraction of split-clusters per testbeam configuration is shown. In the first testbeam period split-clusters account for $1-2$ % in the saturated charge collection configurations (100 V-500 V). The slight increase of the split-cluster fraction at a low bias voltage of 25 V and 50 V might be caused by a wider charge spread since a significant amount of charge is probably trapped. During the irradiated testbeam periods the fraction of split-clusters increases with higher bias voltage but also depends on the operational time. In November 2007, for example
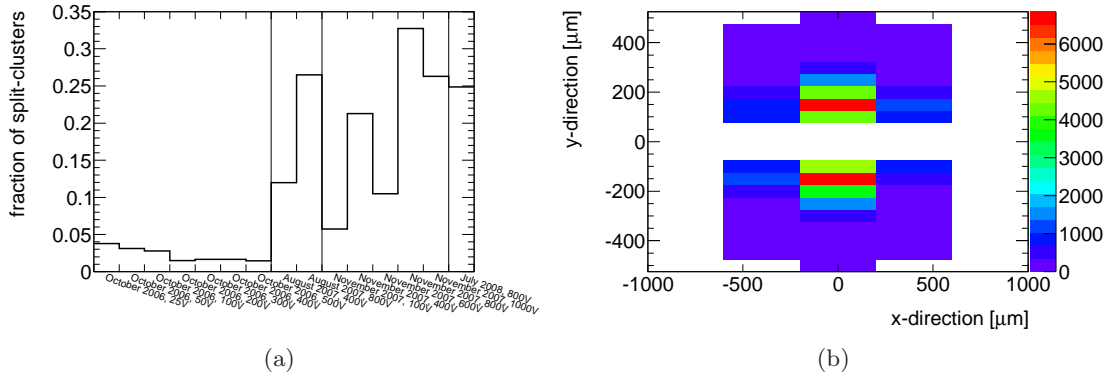
Figure 6.14.: (a) Fraction of split-clusters as a function of the various testbeam configurations, (b) 2-dimensional distribution of the minimal distance (data: November 2007, HV: 800 V).

the fraction of split-clusters is smaller in the small testbeam configurations at 100 V and 600 V than in the capacious testbeam configurations at 400 V and 800 V. The correlations between the amount of split-clusters, the fluence and operating time strengthen the trapping-hypothesis especially in combination with the dynamics of polarisation, which will be introduced in Section 7.2.1.

In November 2007 at a bias voltage of 800 V, up to 33% of all events include split-clusters, see Figure 6.14(a), which cannot be explained by δ-electrons.

In Figure 6.14(b) the distribution of the distance between the hit-position of the matched-partner-cluster and the split-partner-cluster is plotted in two dimensions. Most of the clusters have a distance of $125 - 175$ μm which will be compared with the practical range[10] of δ-electrons. In [42, 43] an empirical formula is given which describes the practical range normalised by the material density as a function of the energy of the δ-electron:

$$r = A \cdot E \left[1 - \frac{B}{1 + C \cdot E} \right] \tag{6.9}$$

where $A = 5.37 \times 10^{-4}$ $g^{-1}cm^{-2}keV^{-1}$, $B = 0.9815$, and $C = 3.1230 \times 10^{-3}$ keV^{-1}. In Figure 6.15 the practical range of electrons in diamond is plotted as a function of the electron energy. Testing the δ-electron hypothesis the energy of the delta electrons is determined via the ToT-distribution of the split-cluster-partners plotted in Figure 6.16(b). The MPV of 13-15 bc corresponds to a charge of 3000-4000 electrons. Assuming that each electron/hole pair is created at an energy of 13.1 eV, the charge corresponds to an energy of $39 - 52$ keV or a practical range of only $7 - 12$ μm. Comparing this rough estimation with the measured minimal distance in Figure 6.14(b), the δ-electron hypothesis is weakened.

---

[10]The practical range is defined as the straight penetration depth (straight distance between the point of origin and the final point of trapping) instead of the real covered distance which is not straight due to multiple scattering.
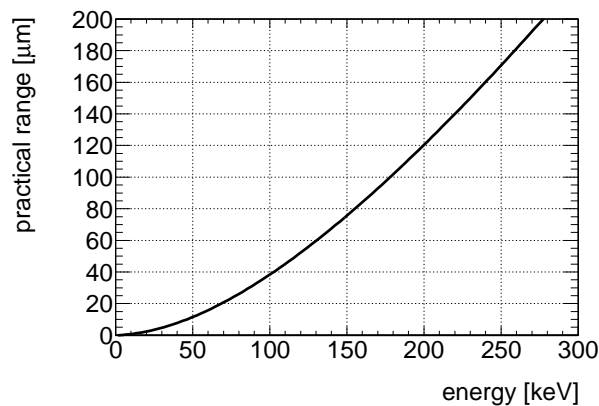
Figure 6.15.: Practical range of electrons in diamond.

6.2.3. Split-Clusters - The Solution of Old Problems

The adoption of split-clusters solves some peculiar characteristics concerning the shape of the ToT-spectrum and several trends in the ToT-spectra, cluster size and cluster multiplicity. Some of these problems have been well known before. In the next four Subsections those peculiar characteristics are introduced and analysed.

Shape of the ToT-Spectrum

As shown in Figure 6.16(a) the ToT-spectrum of the matched-partner-clusters already peaks at about 9 bc whereas in Figure 6.16(b) the spectrum of the split-partner-cluster peaks at roughly

(a)

(b)

(c)
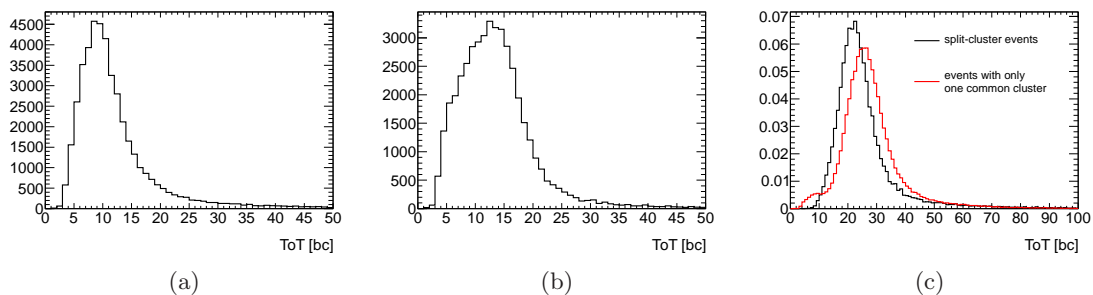
Figure 6.16.: (a) ToT-distribution of matched-partner-clusters, (b) ToT-distribution of split-partner-clusters, (c) merged ToT-distribution of split-clusters and as a reference in red: ToT-distribution of events with only one readout cluster in the DUT (data: November 2007, HV: 800 V).

13 bc. Both values are surprisingly small since for a signal spectrum a ToT peak at roughly 27-29 bc is expected. Besides the distribution of the split-partner-clusters has an unphysical shape in the low charge range; here it significantly deviates from a Landau distribution. Adding both spectra to one ToT-spectrum of split-clusters, the distribution has a reasonable Landau shape and peaks at 21-23 bc, which is illustrated in Figure 6.16(c). As a reference, the ToT-

spectrum of events with only one readout cluster is plotted in red. The difference between the most probable values (MPVs) is 3-5 bc. This deviation corresponds to a charge of 1100-1900 electrons and can be interpreted as the unmeasured charge of the pixels between the two clusters which have not been over threshold.

Peak at Small ToT

Furthermore the split-cluster hypothesis explains an unexpected peak at low ToT in the ToT-spectrum, which is plotted in Figure 6.17 with (in red) and without (in black) split-cluster-correction. Applying no split-cluster-correction the matched-partner-cluster is interpreted as a common matched cluster; the split-partner-cluster is ignored. In this case a peak at low ToT is observed, which disappears if the split-partner-correction is applied. This peak has been known and studied in several analysis but until now has not been understood.
Illustrated as a dotted blue line in Figure 6.17 the peak is made up of 1-hit-clusters which belong to split-clusters. In contrast to the 1-hit-cluster distribution before the split-cluster-correction, the 1-hit-cluster distribution after the correction has no significant peak at small ToT.
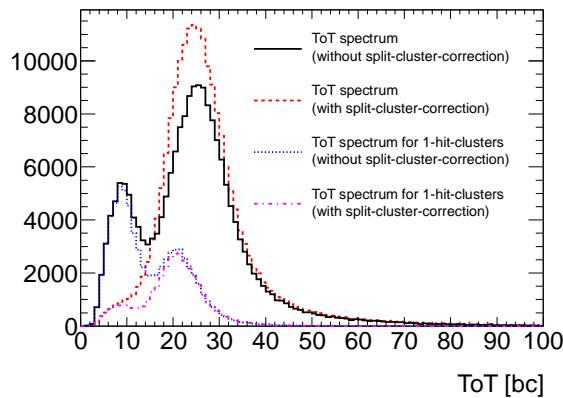
Figure 6.17.: ToT-spectra with and without split-cluster-correction, also the 1-hit-cluster ToT-spectra are plotted (data: November 2007, HV: 800 V).

Dynamics of Split-Clusters

Next to these unexpected characteristics the split-clusters follow a particular dynamic. In the beginning of the data taking roughly 2% of all events include split-clusters. With operating time the fraction of split-clusters increases but finally saturates at $27 - 29$ % as it is shown in Figure 6.18. Run-numbers which are not shown in the plot are not available.
This dynamic also has an effect on the dynamic of the ToT-spectrum which is illustrated in Figure 6.19. The low ToT peak is growing in the ToT-spectra without split-cluster-correction but not in the split-cluster-corrected spectra. In this Figure ToT-spectra with increasing run-numbers are illustrated.
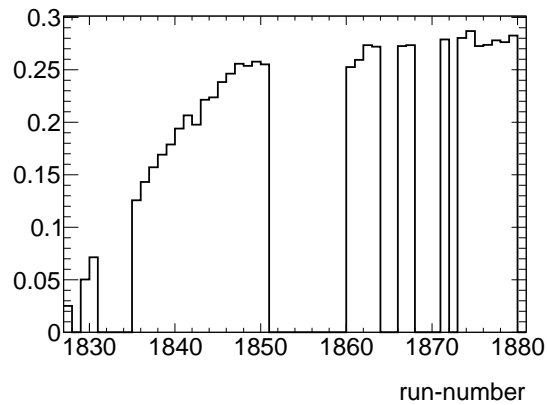
Figure 6.18.: Fraction of split-clusters as a function of the run-number (data: November 2007, HV: 800 V).
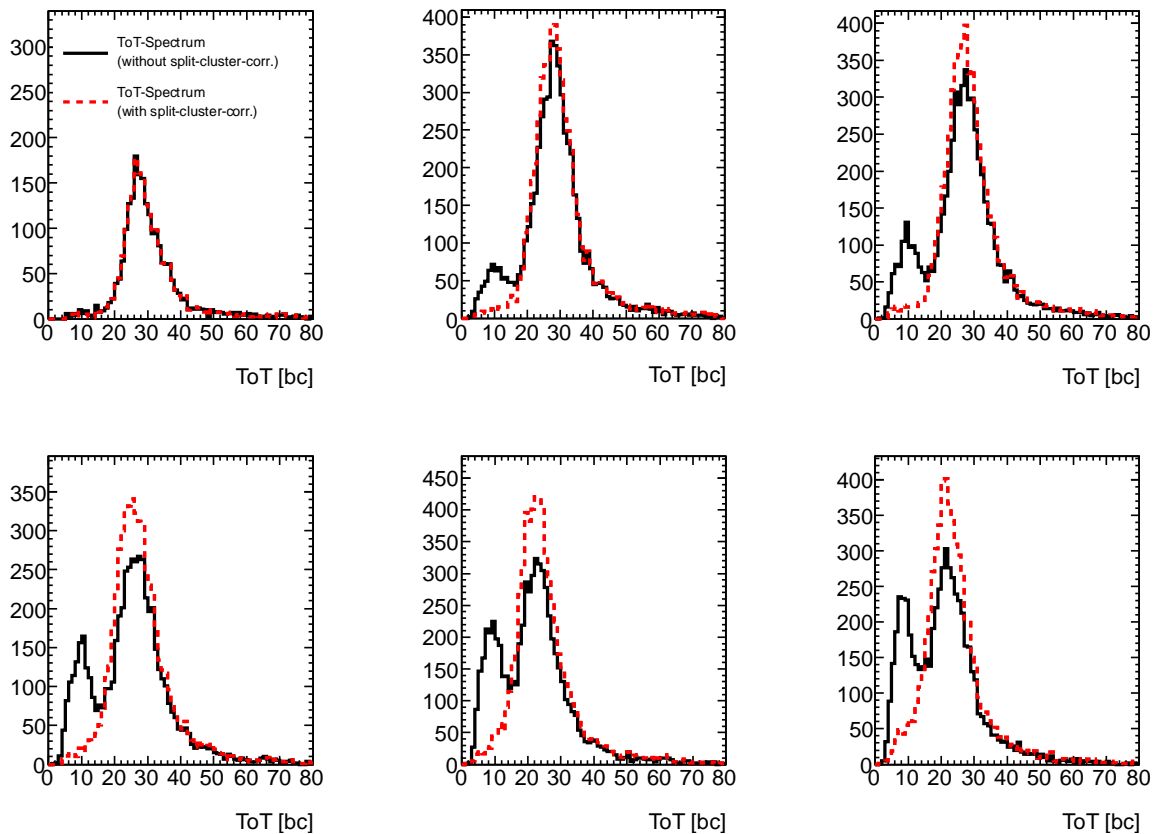
Figure 6.19.: ToT-spectra for different runs: 1827 (top left plot), 1835, 1839, 1845, 1863, 1879 (bottom right plot) (data: November 2007, HV: 800 V).

Cluster Size and Cluster Multiplicity

A detailed study about cluster sizes and cluster multiplicities is given in the next Section; here only the influence of split-clusters is analysed.

In Figure 6.20 cluster size distributions are plotted as a function of the run-numbers. In (a) no split-cluster-correction is applied, whereas in (b) split-clusters are corrected. Comparing plot (a)

(a) (b) (c)
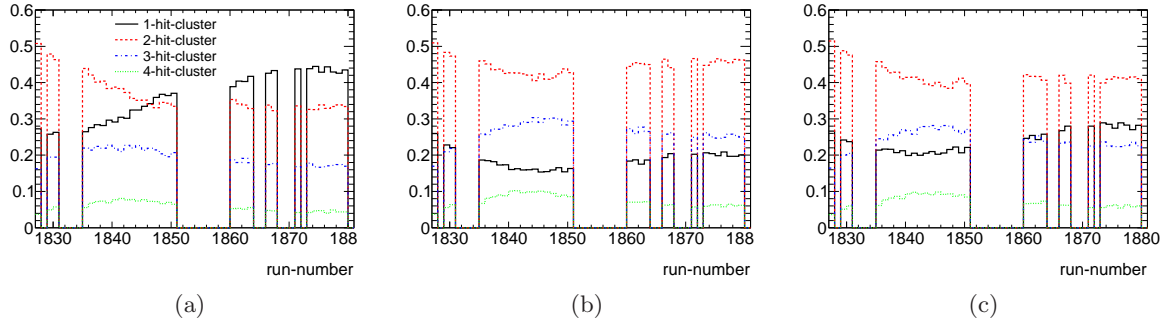
Figure 6.20.: Cluster size distributions as a function of run-numbers (a) without split-cluster-correction, (b) with split-cluster-correction, (c) with only one reconstructed cluster per event (data: November 2007, HV: 800 V).

and (b) with the reference plot in (c), where only events with exactly one reconstructed cluster are considered, in the first instance the reference plot agrees with the cluster size distribution after the split-cluster-correction.

In Figure 6.21 the cluster multiplicity distributions are plotted as a function of run-numbers without split-cluster-correction (a) and with split-cluster-correction (b). Apart from the last seven runs the cluster multiplicity is constant over time if the split-cluster-correction is applied. Since a constant cluster multiplicity is expected, the split-cluster hypothesis is corroborated, and at the same time the peculiar dynamics of the cluster multiplicity is explained.

(a) (b)
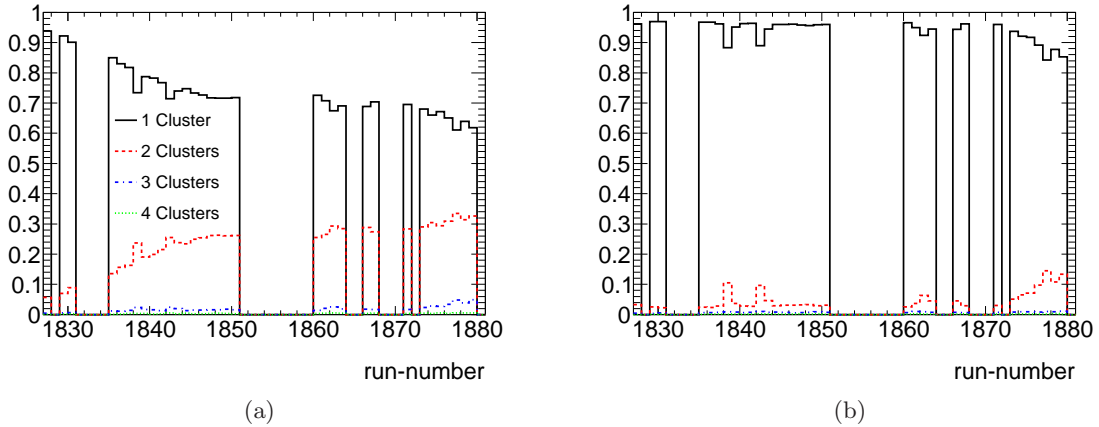
Figure 6.21.: Cluster multiplicity distributions as a function of run-numbers (a) without split-cluster-correction, (b) with split-cluster-correction (data: November 2007, HV: 800 V).

6.3. Cluster Size and Charge Sharing

In this Section cluster sizes and charge sharing are studied. Analogous to Section 6.1 matched clusters which pass the basic masks as well as the special region masks are analysed. In addition split-clusters are included, so that the matched-partner-cluster and split-partner-cluster are interpreted as one (split-)cluster, see last Section.

6.3.1. Cluster Size Overview

Cluster size is defined as the number of pixels over threshold which constitute a cluster. In Figure 6.22 the fractional cluster sizes of all testbeam configurations are plotted as a function of the bias voltage. Neglecting clusters with five or more pixels, the cluster size is normalised to the number of clusters with one, two, three or four pixels. Guiding the eyes measurement points
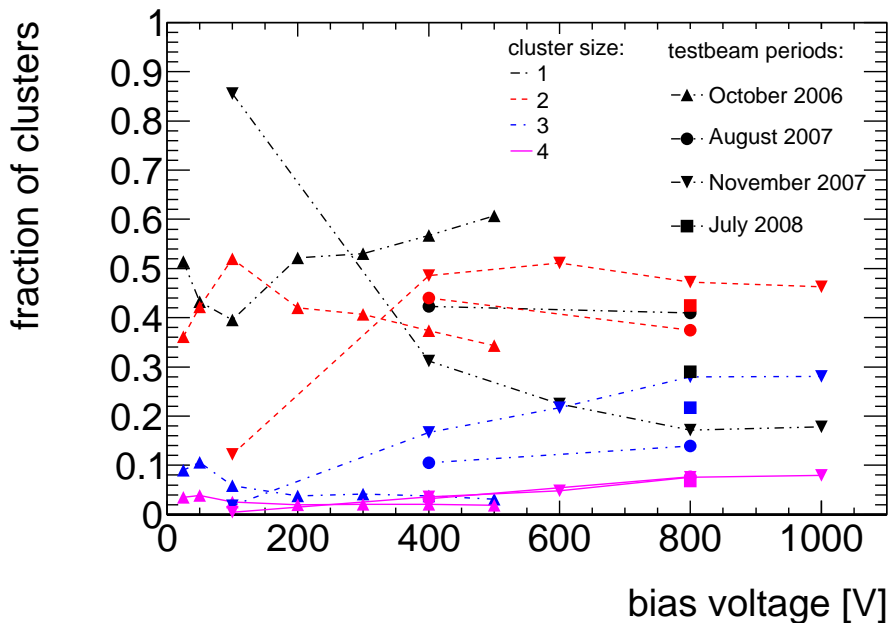
Figure 6.22.: Cluster size distribution of all testbeam configurations as a function of the bias voltage.

with the same cluster size from the same testbeam period are connected with lines.

First Testbeam Period: Focusing on the first testbeam period without irradiation (October 2006)[11] the testbeam configurations with saturated charge collection (100 V-500 V) fulfil physical expectations: as explained before the impact of diffusion decreases with increasing bias voltage resulting in a smaller charge spread. Consequently the fraction of 1-hit-clusters grows with the electric field. At 400 V the ratio between 1-hit and 2-hit-clusters is 57% : 37.5%. At 25 V and 50 V less charge is collected, and 1-hit-clusters dominate since it is not enough charge collected to produce bigger clusters.

Testbeam Periods After Irradiation: In contrast to the first testbeam period in the testbeam

---

[11]For this testbeam period cluster sizes have also been studied in [34]. Numbers slightly differ as in [34] no masks and no matching criteria have been applied and 4-hit-clusters have been excluded.

periods after irradiation the cluster size in general increases with bias voltage. The trend from 100 V to 400 V can be interpreted in the same way as the trend from 25 V to 50 V in October 2006 via unsaturated charge collection[12]. For higher voltages the common charge focusing effect which leads to smaller cluster sizes at higher electric fields does not occur or at least is covered by another physical effect. Polarisation might explain this effect, see Section 7.2.1. 2-hit-clusters dominate these testbeam configurations. In November 2007 for example approximately 48% of all hits are 2-hit-clusters at saturated charge collection (400 V-1000 V). At a bias voltage of at least 800 V even more 3-hit-clusters exist than 1-hit-clusters.

6.3.2. Charge Sharing

In Figure 6.23 the probability of charge sharing is analysed, which is defined as the ratio between the number of clusters with cluster sizes bigger than one and the number of all clusters. In this Figure the charge sharing probability is plotted as a function of the pixel-folded fit-position[13] for the testbeam configurations in October 2006 and November 2007 with the largest statistics. For

(a) October 2006, HV: 100 V

(b) October 2006, HV: 400 V

(c) November 2007, HV: 400 V

(d) November 2007, HV: 800 V
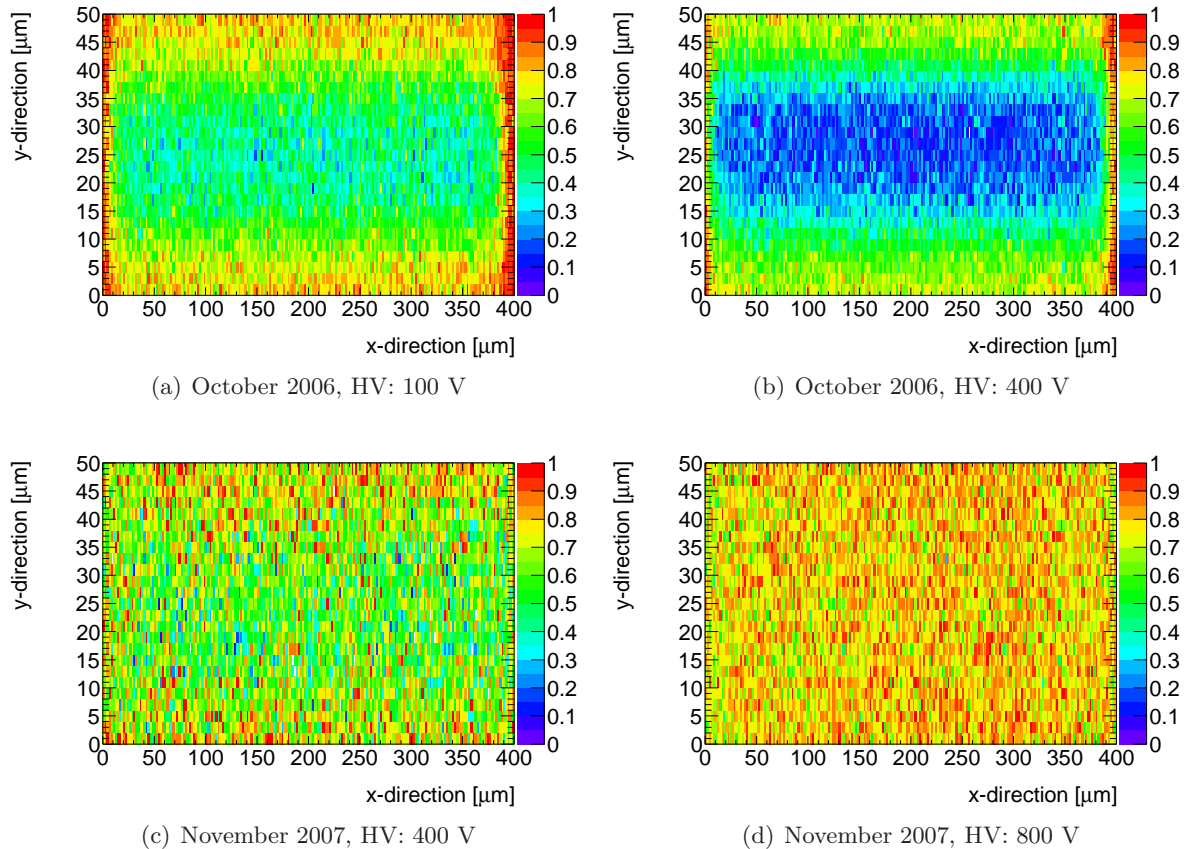
Figure 6.23.: Pixel-folded charge sharing probability for October 2006 and November 2007.

the unirradiated testbeam period it is illustrated that with higher bias voltage charge sharing at the pixel corners decreases because of less diffusion. It is observable that in the right pixel

---

[12]The unsaturated charge collection will be analysed in Section 6.5.2.

[13]Pixel-folded fit position is defined in Section 6.1.2 (see Figure 6.6).

corners charge-sharing is bigger than in the left pixel corners. This effect can be due to mis-alignment. In November 2007 charge sharing is marginally visible at 400 V. For higher electric fields no systematic pattern can be identified.

In Figure 6.24 the pixel-folded y-fit-position for 2-hit-clusters is illustrated. The testbeam configuration October 2006 (HV: 400 V) is used. Excluding charge sharing at the pixel corners,
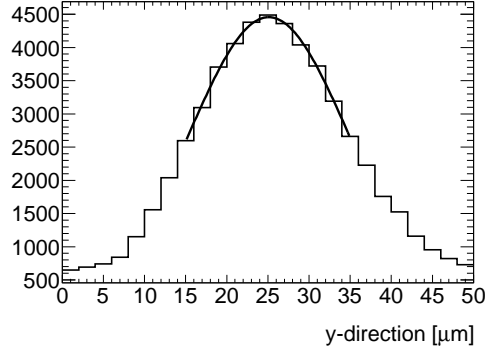
Figure 6.24.: Pixel-folded y-fit-position distribution for 2-hit-clusters; excluding the pixel corners only hits in the central pixel region in x-direction are used (50 μm < pixel-folded x-fit-position < 350 μm) (data: October 2006, HV: 400 V).

only hits are considered if the pixel-folded x-fit-position is bigger than 50 μm and smaller than 350 μm. To determine the region where charge sharing occurs, the 2-hit-cluster distribution is shifted 25 μm, so that the pixel centres are located at 0 μm and 50 μm. The distribution is fitted with a Gauss distribution. A width of $\sigma_{Gauss} = 9.69 \pm 0.14$ μm is determined. In the following the maximal charge spread caused by diffusion is calculated to determine the impact of diffusion on the size of the charge sharing region.

6.3.3. A Simple Estimation of the Maximal Charge Spread

In [43] the charge collection of a single electron/hole pair is simulated in an electric field, generated by a strip (or a long pixel) with a pitch of 50 μm. In the beginning the electron/hole pair is centred over the strip and drifts directly towards this strip neglecting diffusion at first. During the drift, charge is influenced at the neighbour strips. Finishing the drift phase the complete charge is collected at the strip and no charge is collected in the neighbour strips due to the small pixel effect mentioned in Section 3.2.3. If the charge is trapped during the drift phase, charge is collected at the strip as well as in the neighbour strips. This effect is caused by the complicated electric field. In the case of a completely undisturbed drift through the sensor material the spread of collected charge can therefore only occur via diffusion[14].

Assuming an initial point-shaped charge distribution after drift time t the charge density $n(x, y, t)$ will be Gaussian distributed via diffusion:

$$n(x, y, t) = \frac{n_0}{4\pi\sigma^2(t)} e^{-\frac{x^2+y^2}{2\sigma^2(t)}},$$ (6.10)

where σ^2 is given by:

$$\sigma^2 = 2Dt \quad \text{with a diffusion coefficient:} \quad D = \frac{kT\mu}{e}.$$ (6.11)

---

[14]In this simple model a point-shaped charge distribution is considered.

To maximise the charge spread the point-shaped charge distribution has to traverse the complete sensor. So only the drift of the electrons has to be considered since the pixels are positively charged. The generated holes are directly absorbed by the cathode and therefore are ignored in the model. σ^2/t is given by:

$$\frac{\sigma^2}{t} = \frac{2kT\mu_{el}}{e} \approx 90.95 \text{cm}^2/\text{s} = 9.095 \ \mu\text{m}^2 \ \text{ns}^{-1}. \tag{6.12}$$

Assuming perfect charge collection (no trapping, no recombination) the charge distribution needs

$$t \leq \frac{d}{\mu_e E} = \frac{d^2}{\mu_e U} = 2.17 \ \text{ns} \tag{6.13}$$

to cross the sensor if a bias voltage of 400 V is applied and the sensor has a thickness of 395 μm. Finally we get a maximal charge spread of: $\sigma \leq 4.44 \ \mu$m. This value significantly differs from the measured region in the pixel where charge sharing occurs ($\sigma_{Gauss} = 9.69 \pm 0.14 \ \mu$m). Charge loss via trapping and recombination or a particle track, which is not perpendicular to the sensor surface, might explain the deviation. Also the inhomogeneous electric field at the edge of the pixel metallisation[15] has an effect on the charge sharing.

The Gaussian fitted value matches with the result from the eta-algorithm (9$\pm$2 μm.), see Section 5.3.5.

---

[15]A normal pixel (400 μm $\times$ 50 μm) has a metallisation of 380 μm $\times$ 30 μm.

6.4. Detection Efficiency and Noise

Hit efficiency is defined as the ratio between the number of reconstructed hits in the DUT k, which are matched, and the number of reconstructed tracks n:

$$\epsilon = \frac{k}{n}. \tag{6.14}$$

In this analysis tracks will be considered only if they pass the masked regions of the DUT. As it has been defined in Section 6.1, a hit in the DUT is matched to a track if the x-residual is smaller than 400 μm and the y-residual is smaller than 150 μm.

6.4.1. Error Treatment

At an efficiency of nearly 100% the statistical uncertainty has to be treated in a special way. Considering the detection of a particle passage as a binomial process the probability that k hits are detected with a known (*true*) efficiency of ϵ and n performed particle passages is given by:

$$P(k; \epsilon, n) = \binom{n}{k} \epsilon^k (1 - \epsilon)^{n-k} \tag{6.15}$$

with the mean value of $< k >= \epsilon n$ and a variance of $V(k) = \sigma_k^2 = n\epsilon(1 - \epsilon)$. For the estimator $\hat{\epsilon} = k/n$, which is measured, the variance is given by simple error propagation of σ_k:

$$V(\hat{\epsilon}) = \frac{\sigma_k^2}{n^2} = \frac{k(n-k)}{n^3}. \tag{6.16}$$

In the limiting case when $k \to 0$ or $k \to n$ the statistical uncertainty approaches an "unphysical" zero. In that way efficiencies approaching 100% automatically have a vanishing error.
Avoiding this unwanted effect instead of using $P(k; \epsilon, n)$ and the simple error propagation of $\hat{\epsilon}$, the probability function of $\epsilon : P(\epsilon; k, n)$ has to be studied. The calculation via Bayes Theorem is described in detail in [44]. With an efficiency probability density of

$$P(\epsilon; k, n) = (n + 1) \binom{n}{k} \epsilon^k (1 - \epsilon)^{n-k} \tag{6.17}$$

it follows:

$$< \epsilon > = \frac{n + 1}{k + 1} \tag{6.18}$$

$$V(\epsilon) = \frac{k + 1}{n + 2} \left(\frac{k + 2}{n + 3} - \frac{k + 1}{n + 2} \right). \tag{6.19}$$

6.4.2. Efficiency

In Figure 6.25 the detection efficiencies and the related errors of all testbeam configurations are summarised. Exact values are listed in Table A.4.
In the first testbeam period efficiencies of $99.7\% - 99.8\%$ are reached for the testbeam configurations with saturated charge collection (100 V-400 V). For unknown reasons the efficiency decreases at $500V$ to 98.4%.
As in the previous Sections, the results for August 2007 are listed but not interpreted because of the bad testbeam setup and the low statistics.
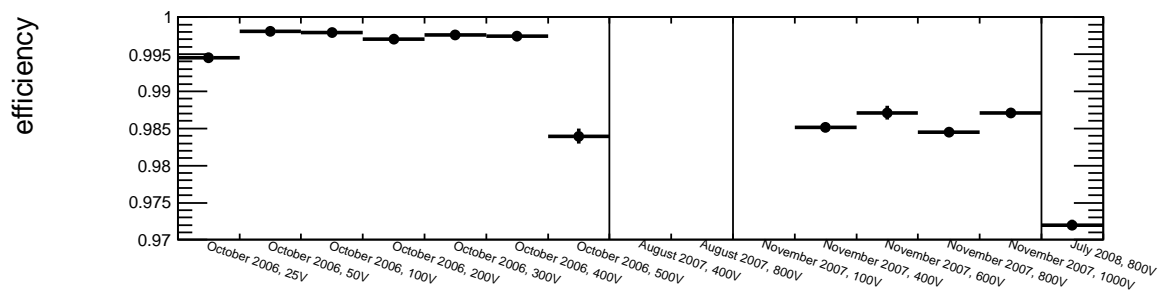
Figure 6.25.: Efficiencies of all testbeam configurations with appropriate errors. Values outside of the chosen range are listed in Table A.4.

In November 2007 the configurations with saturated charge collection have a mean efficiency of 98.5%. Unexpectedly the efficiency decreases in July 2008 in comparison to November 2007.

In Figure 6.26 efficiency maps of three example testbeam configurations are plotted. Inefficient pixels seem to exist in *clusters* due to a number of possible effects concerning the readout electronics, the metallisation or the sensor material (e.g.: merged bumps, clusters of noisy pixels).

(a) October 2006, HV: 400 V.

(b) November 2007, HV: 800 V.

(c) July 2008, HV: 800 V.
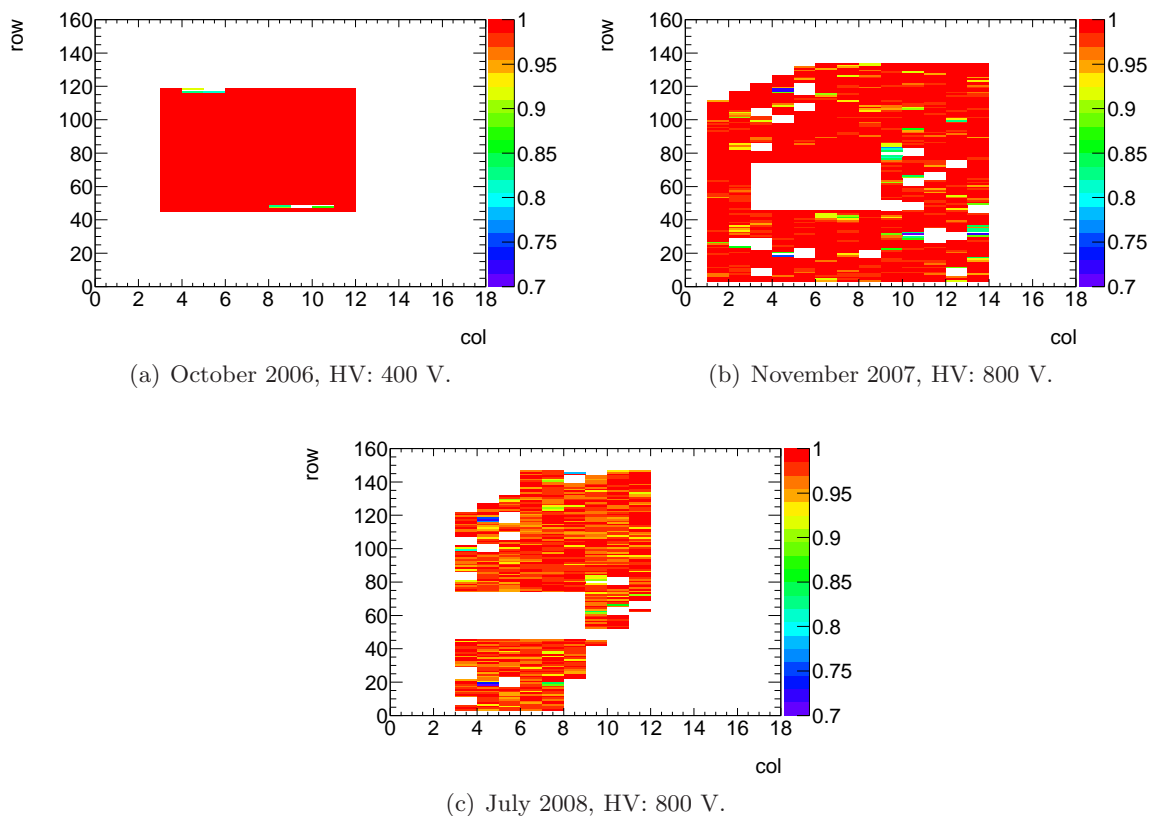
Figure 6.26.: Efficiency maps.

6.4.3. Noise

Noise is defined as the ratio between events with no matched hit or events with more than one reconstructed hit and events with a reconstructed track. Again the common masks are applied and the split-cluster-correction is taken into account.

In Figure 6.27 noise information of all testbeam configurations is summarised. Again the exact values are listed in Table A.5. In the first testbeam period roughly 4% of all events are noisy.
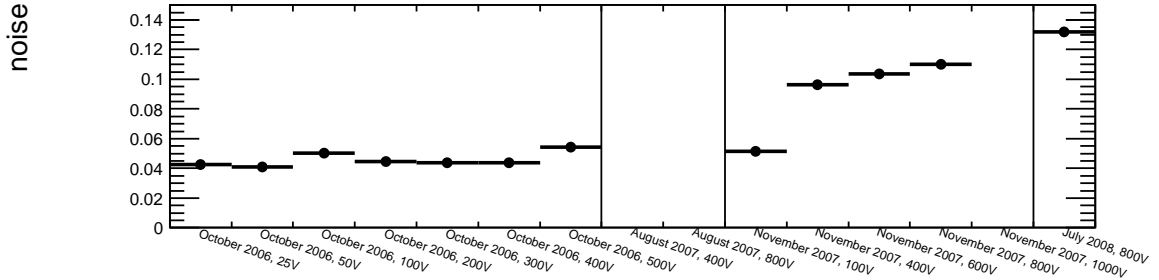
Figure 6.27.: Noise of all testbeam configurations with appropriate errors. Values outside of the chosen range are listed in Table A.5.

This fraction increases in November 2007 from 5% at 100 V to 19.4% at 1000 V probably due to an increased leakage current.

In Figure 6.28 the noise maps of three example testbeam configurations are plotted. Here the ratio:

$$\frac{\text{number of noise hits at their seed-pixel position}}{\text{number of matched hits at their pixel fit-position}}$$

is shown for each pixel. In comparison with the number of matched hits the number of noise hits significantly increases in the "outer" regions of the sensor. Again this characteristic can be explained by the leakage current, which especially accumulates at the sensor edge due to a higher concentration of crystal defects.

In Figure 6.29 the cluster size distribution of all noise hits is plotted as a function of the testbeam configuration. In contrast to the naive assumption that noise clusters are rather small, 1-hit-clusters of the first testbeam period constitute only $15-30\%$ of all noise clusters. In this testbeam period the amount of big noise clusters (> 3 pixels) is especially large ($> 30\%$).

6.4.4. Cluster Multiplicity

In this context also the cluster multiplicity is analysed. Exclusively focusing on signal events, which in any case contain a matched hit, the cluster multiplicity in the DUT is defined as the number of reconstructed clusters per event. In Figure 6.30 cluster multiplicity distributions are plotted for all testbeam configurations.

Analysing the first testbeam period, in 98% of all events only one cluster is reconstructed, which by construction is a matched cluster. In the third testbeam period this fraction decreases when the bias voltage exceeds 600 V. So in November 2007 the fraction of events with two reconstructed clusters increases up to 5% (9%) for runs at a bias voltage of 800 V (1000 V). This significant increase of noise events is not well understood.

At the same bias voltage and at the same fluence the fraction of events with two clusters (3.5%)
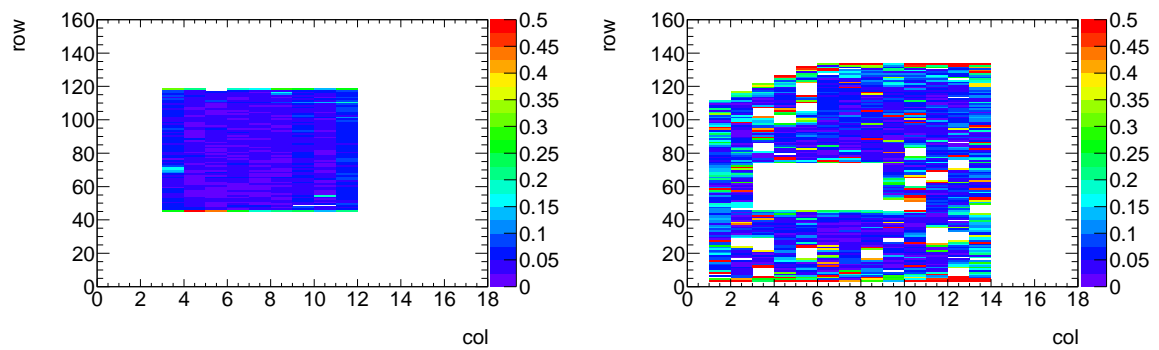
(a) October 2006, HV: 400 V.

(b) November 2007, HV: 800 V.
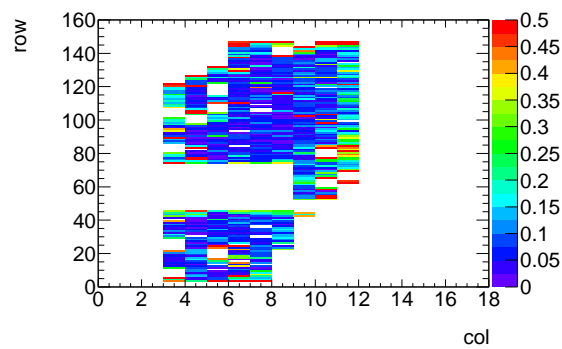
(c) July 2008, HV: 800 V.

Figure 6.28.: Noise maps.

in July 2008 differs significantly from the fraction in November 2007 (5%). This noise might be explained by some dynamic effect like polarisation, see Section 7.2.1.
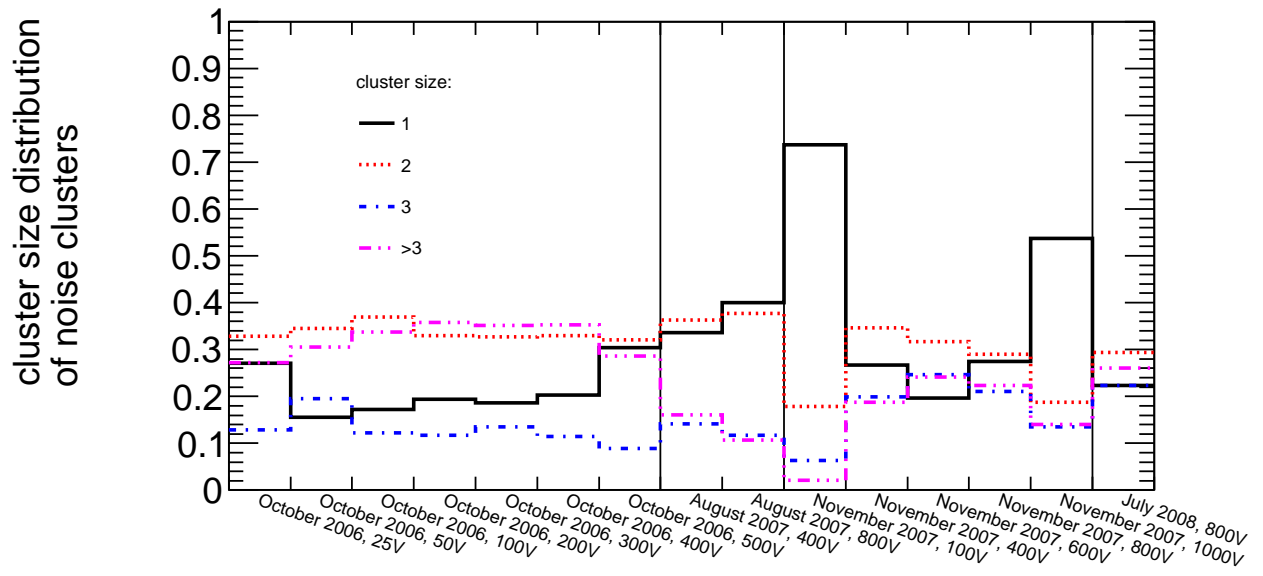
Figure 6.29.: Cluster size distributions for noise clusters as a function of the testbeam configuration.
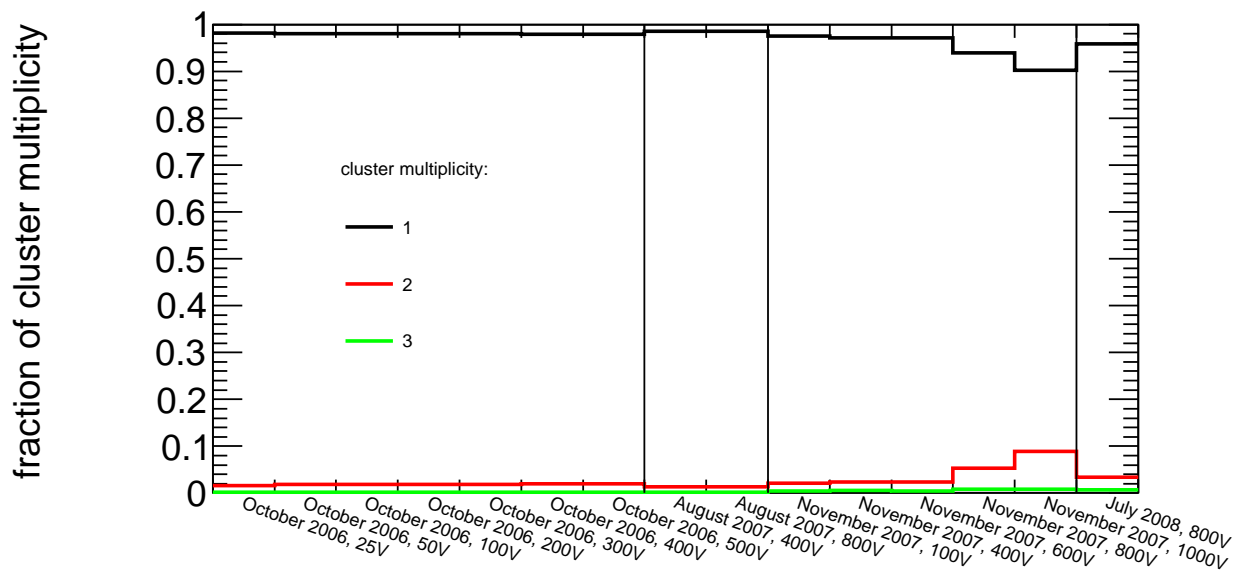
Figure 6.30.: Cluster multiplicities for all testbeam configurations.

6.5. Charge Spectra and Charge Collection Distance

The central quantity for the characterisation of radiation hardness is the damage coefficient k which was introduced in Section 3.3.3. It is defined by the charge collection distance (CCD) at different fluences and is determined in the end of this Section. Measuring CCD with an ATLAS pixel module, a precise knowledge of the ToT-charge-calibration is essential. In the beginning of this Section a new fit method for the calibration data is presented, which is more precise in the low charge range than the old (and new) ATLAS calibration curves. Afterwards the charge spectra of all testbeam configurations are analysed. A special focus is placed on their dynamics with respect to the operating time.

6.5.1. ToT Charge Calibration

As mentioned in Section 4.3.2 it is possible to inject various well defined charges in each pixel to calibrate their specific ToTs.

<u>ATLAS calibration method</u>: In a standard ATLAS procedure these calibration curves are fitted with an invertible, three parameter function. For the ATLAS pixel detector two fit functions have been studied:

$$\text{ToT}(Q) \quad = \quad \text{par0} + \frac{\text{par1}}{Q + \text{par2}} \quad \text{(old fit function)} \tag{6.20}$$

$$\text{and} \;\; \text{ToT}(Q) \quad = \quad \text{par0} \cdot \frac{Q + \text{par1}}{Q + \text{par2}} \quad \text{(new fit function).} \tag{6.21}$$

The old fit function (Eq. 6.20) has mainly been used in the development process of the detector. The new fit function (Eq. 6.21) is actually used today. To reduce the size of the calibration data the pixel fit functions are averaged and two calibration functions per front-end are determined: at ATLAS fit parameters for normal-long, interganged and non-ganged pixels[16] are combined to
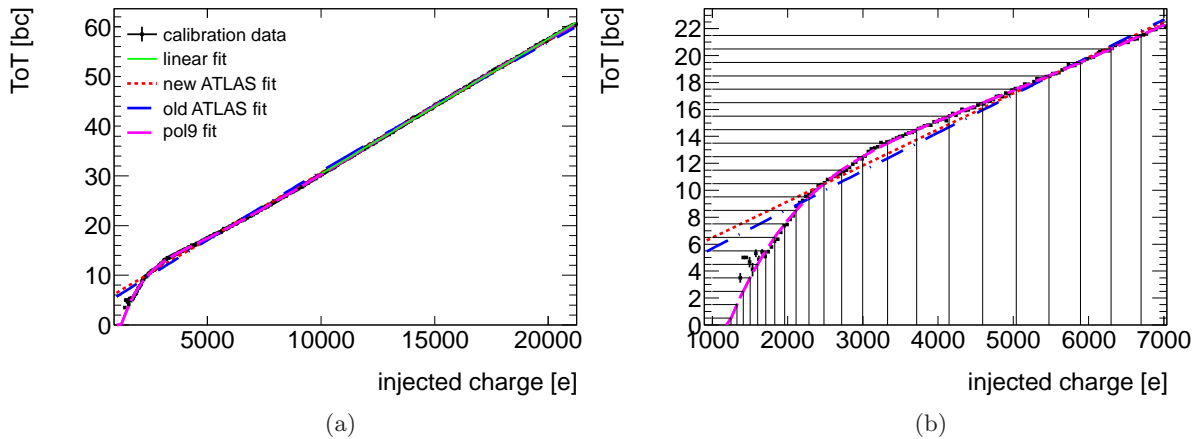
Figure 6.31.: An example calibration curve and its fit functions are plotted at different charge ranges: (a) complete calibration range; (b) magnification for small charges. In (b) the mapping between ToT values and charge intervals is illustrated.

---

[16]Pixel types have been defined in Section 4.3.1.

one fit function, and ganged-long and ganged pixels are treated in a separate fit function.
In Figure 6.31 an example calibration curve for one pixel is plotted with the corresponding fit functions. In general the calibration curves show a nearly linear behaviour for charges with more than 7000 electrons. In the low charge range the calibration data is not well described by the standard fits due to a bump with negative curvature[17].
New calibration method: To obtain a more precise calibration in the low charge range the data is fitted by a polynomial of ninth order, which is also plotted in Figure 6.31. Instead of inverting
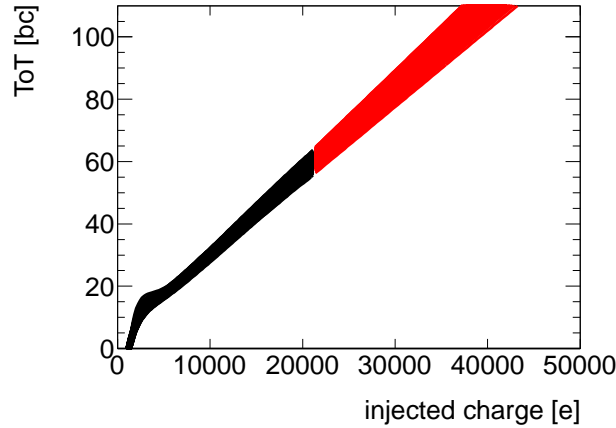
Figure 6.32.: Polynomial fits (black lines) and linear fits (red lines) of all pixels of CD181.

the fit function, a look-up table for each pixel is produced. In the charge range of the calibration data set, this look-up table allocates each ToT value to a charge interval determined by the polynomial fit. The intervals are illustrated in Figure 6.31(b). For the calibration of ToT values, which exceed the charge range of the calibration data set, a linear fit is used. To exclude the low charge bump in this fit, the fit range starts at 10000 electrons.
In Figure 6.32 the polynomial fits of all pixels and the linear extrapolations are plotted for all pixels of CD181. Due to significant variations between the fits, which are also demonstrated in Figure 6.34, the look-up tables of each pixel cannot be averaged. In the following a specific look-up table is used for each pixel.
In Figure 6.33 the performance of the various fits are illustrated via charge residuals. A charge-residual is defined as the difference between the injected charge and the charge, which is determined by the fit and the measured ToT. Some diagonal structures can be recognised in the charge residuals. They can be explained by the predefined amount of injected charge (Vcal-DAC, see Section 4.3.2) and the quantised ToT measurement. As expected, the polynomial fit has the smallest charge residuals over the whole charge range and consequently the best performance.
For the different testbeam periods four different ToT-charge-calibration data sets are available, which have been produced at that time. The data sets are summarised in Table 6.6. In October 2006 CD181 was calibrated with both capacities (C_{low} and C_{high}), see Section 4.3.2. In the following the calibration data generated with C_{high} is ignored as all other calibration data has been generated with C_{low}. Since the relation between calibration data and testbeam period is not documented, the data sets have been chronologically allocated. Motivated by this lack of

---

[17]The reason for this bump is unknown. It cannot be generated by the effect of timewalk, which would cause a bump with positive curvature, as a time-interval is lost for small charges, see Section 4.3.2.
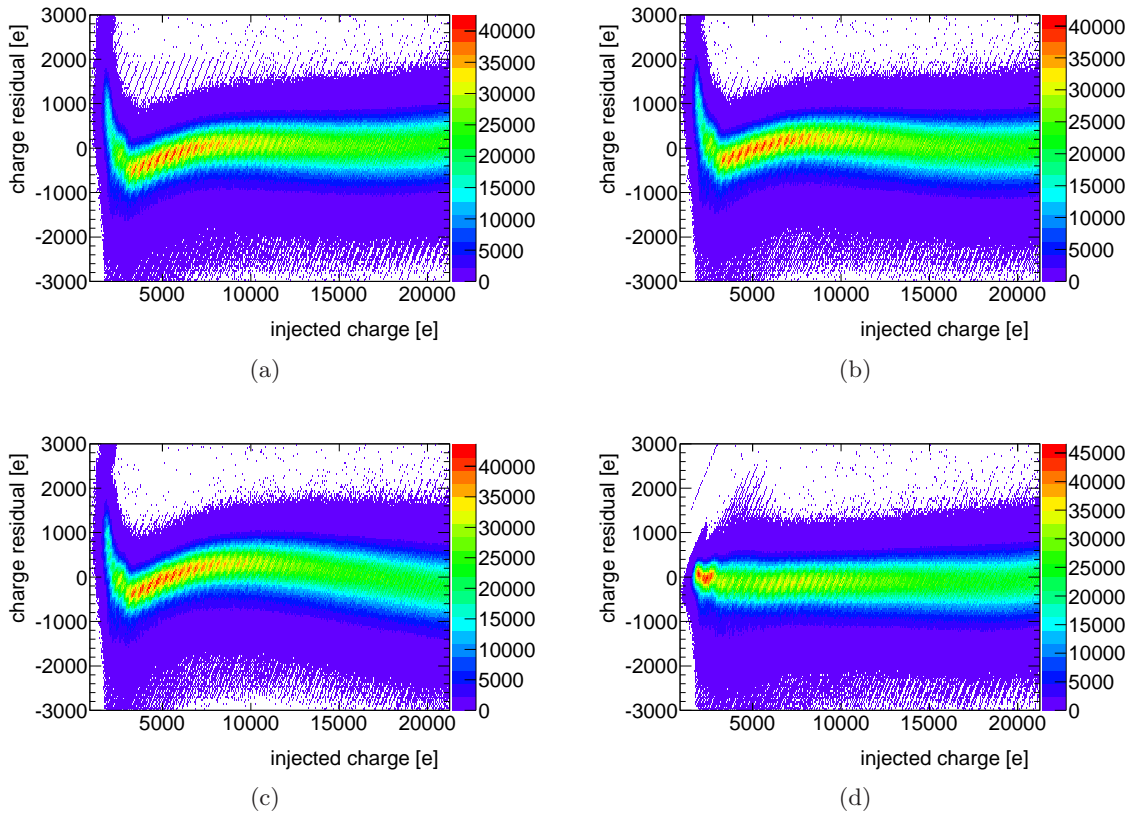
Figure 6.33.: Charge residuals (definition: injected charge - fitted charge(measured ToT)) for different fit functions: (a) linear function, (b) new ATLAS function, (c) old ATLAS function, (d) ninth-degree polynomial fit
(data: 2007_09_01_tune_Merged.tot).

knowledge, the deviations between the calibration data sets are studied in Figure 6.34. Here the mean charge of all pixel calibration curves is plotted against the ToT. The inserted errors correspond to the RMS.

In the physically relevant charge range (8000-13000 electrons), which is illustrated in Figure 6.34(b), the calibration curves differ up to 500 electrons.

In Figure 6.35 the charge interval which corresponds to a certain ToT value is plotted against

file name:	min. charge:	max. charge:	Vcal stepsize:	$C_{low}/$ C_{high}	used for testbeam period:
20061023_1700e_TOTtune_1_0.tot	1250e	18700e	2	low	October 2006
20061023_1700e_TOTtune_3_0.tot	6810e	105000e	2	high	-
20070313_TOTCAL_1700_MergedII.tot	1870e	38500e	1	low	August 2007
2007_09_01_tune_Merged.tot	920e	21230e	1	low	November 2007 and July 2008

Table 6.6.: Analysed ToT-charge-calibration data.

(a)   (b)
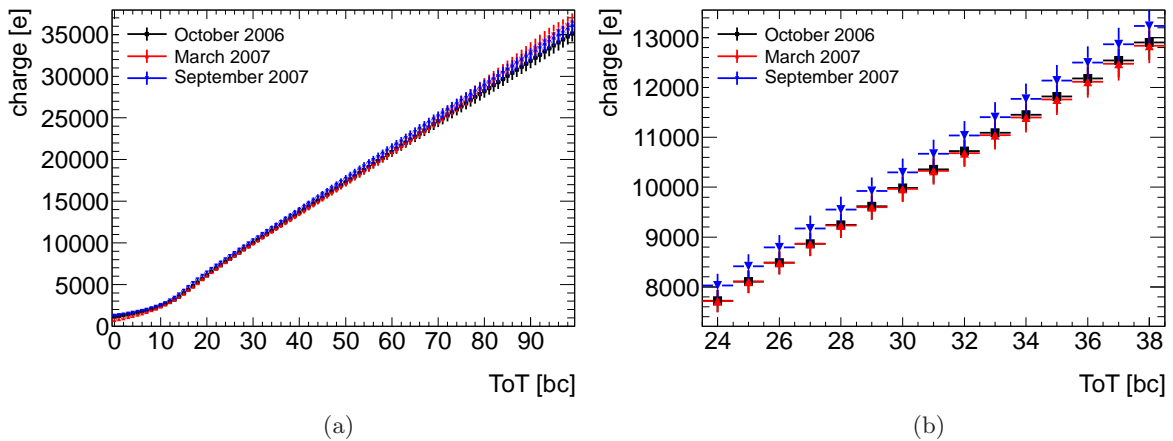
Figure 6.34.: (a) Mean charge (averaged over look-up tables of all pixels) of different calibration data sets plotted as a function of ToT; (b) magnification of the physically relevant range in (a).

the ToT. From a specific ToT value on the intervals are constant as the linear fit is used. The maximal mean interval size is 457 ± 19 electrons. Again the RMS is plotted as error.

Regarding below mean values or MPVs of the charge spectra the errors in Figure 6.34 have to be considered as statistical errors and the interval size shown in Figure 6.35 contributes to the systematical error.

For the testbeam period July 2008 it is impossible to assign appropriate charge spectra as no calibration data has been recorded in 2008. Therefore the calibration data of September 2007 will be also allocated to the testbeam period July 2008.
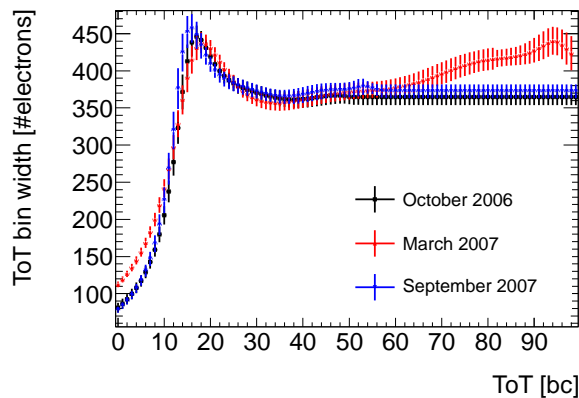
Figure 6.35.: Mean charge intervals (averaged over look-up tables of all pixels) of different calibration data sets plotted as a function of ToT.
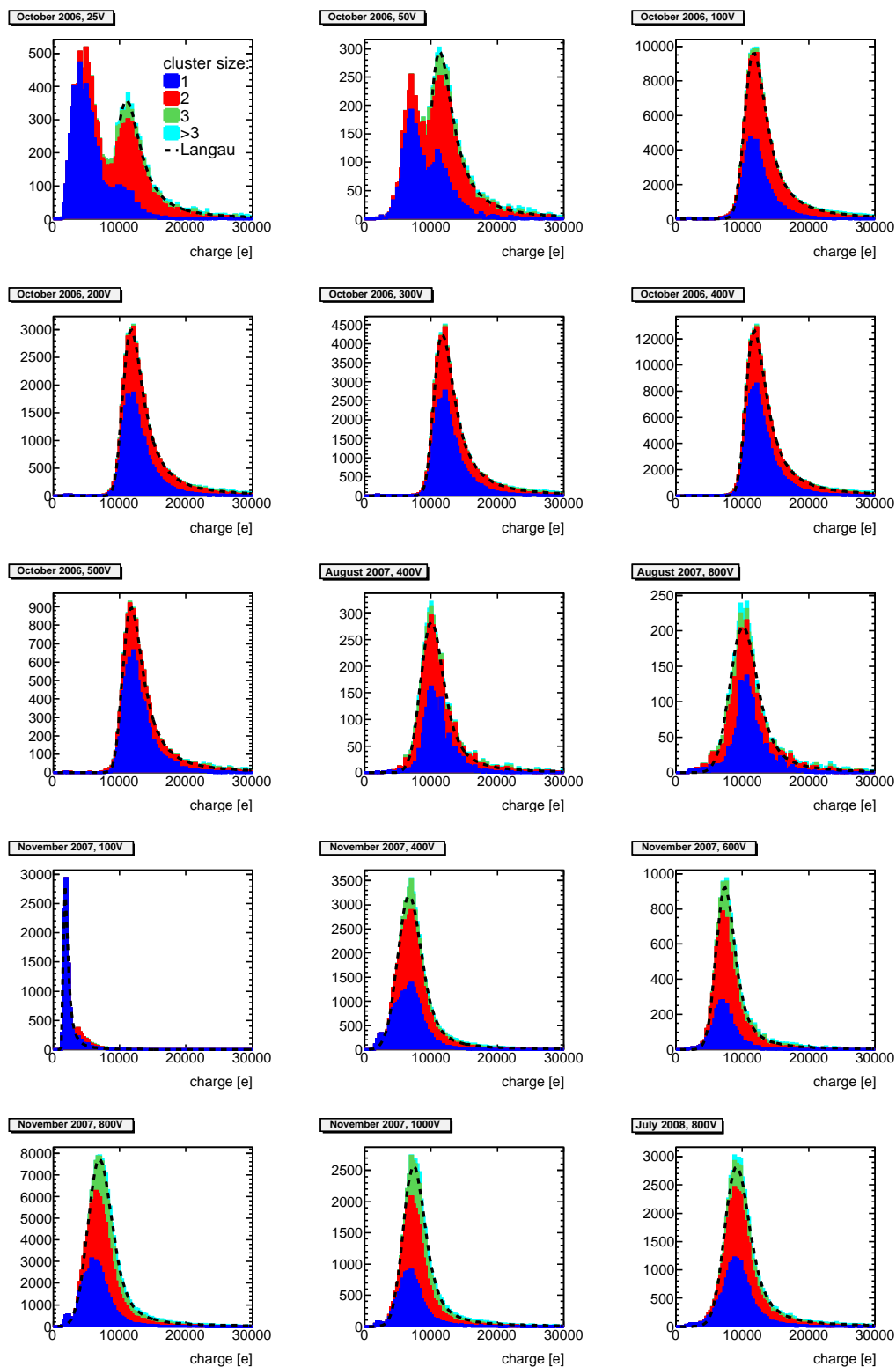
Figure 6.36.: Charge spectra of all testbeam configurations. The contributions of different cluster sizes are stacked.

6.5.2. Charge Spectra

To characterise the charge spectrum two straggling functions have been studied: a conventional Landau function and a convolution of a Landau function and a Gaussian distribution, also called *Langau*. Both straggling functions have been introduced in Section 3.2.2. Since the Langau function is the better model in terms of χ^2, only this straggling function is analysed in this Section. A complete overview of all charge spectra at different bias voltages and fluences is given in Figure 6.36. Here again the split-cluster-correction and all introduced masks (basic masks + special regions masks) are applied.

It is noticeable that the testbeam configurations at low bias voltage differ significantly from the other configurations: in October 2006 two peaks exist at a bias voltage of 25 V and 50 V instead of one charge peak. In some events of these testbeam configurations charge is partially absorbed. Since at low bias voltage diffusion has a larger impact on the signal formation, the charge is widely spread, so that some pixels are below threshold. In this case an additional low charge peak occurs. Another possible reason for the peak at low charges is recombination which increases at lower bias voltage. For the following analysis only the peak at high charges is fitted and thus is probably overestimated. Furthermore the testbeam configuration in November 2007 at a bias voltage of 100 V is exceptional. Here only a peak at low charges exists, which is not completely understood.

As the central quantity for the characterisation of a charge spectrum the most probable value (MPV) of the Langau fit is chosen. In Figure 6.37 the MPVs of the Langau fits are plotted
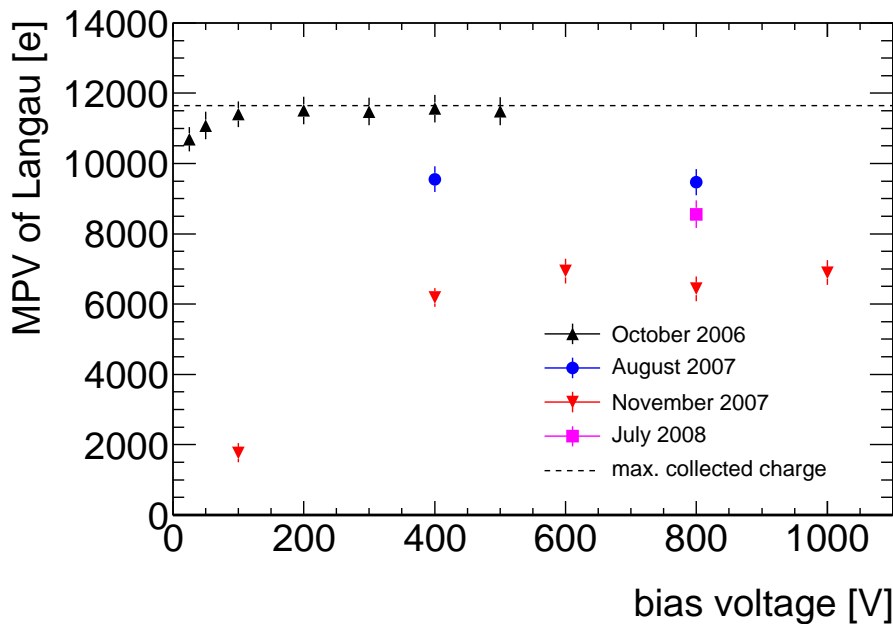
Figure 6.37.: MPV of Langau distribution as a function of the bias voltage for all testbeam configurations.

as a function of the bias voltage. The inserted errors include the statistical deviations of the various calibration curves (illustrated as error bars in Figure 6.34) as well as the systematic errors caused by the limited charge resolution (illustrated as ToT-interval sizes in Figure 6.35).

Prediction of a Maximal MPV: The dotted black line indicates the theoretical predicted value of the MPV if the sensor is not irradiated. A simple model is used to determine this value:

$$q_{max} = d_{Sensor} \cdot q_{MPV} = 395 \ \mu\text{m} \cdot 29.5 \ \text{electrons}/\mu\text{m} = 11653 \ \text{electrons} \tag{6.22}$$

where d_{Sensor} corresponds to the sensor thickness. $q_{MPV} = 29.5 \pm 2.5 \ \text{electrons}/\mu\text{m}$ is the most probable number of electron/hole pairs generated by a minimum ionising particle traversing 1 μm diamond. q_{MPV} is scaled from the measured charge spectra of all testbeam configurations using the literature value: $q_{MEAN} = 36 \ \text{electrons}/\mu\text{m}$. This mean value has been measured in [29] and is the standard value in RD42. The quoted error of 2.5 electrons/μm corresponds to the RMS of the q_{MPV} values which have been calculated for the various testbeam configurations.

Saturation of Charge Collection: Due to an insufficient bias voltage charges recombine. This effect decreases and finally saturates with increasing bias voltage. From Figure 6.37 the minimal bias voltage of saturated charge collection can be estimated for the first and third testbeam period. In October 2006 charge collection saturates at around 100 V whereas in November 2007 (after the second irradiation) charge collection saturates at around 400 V. The increase of the saturation threshold is caused by an increase of trapping centres due to radiation damage.

General Observations: For the testbeam configurations in October 2007 with saturated charge collection the MPVs of the charge spectra agree with the theoreticaly prediction.
As expected less charge is collected after irradiation, e.g. at 400 V charge collection decreases roughly 47% from 11500 electrons to 6100 electrons.
Surprisingly in July 2008 the collected charge is significantly higher than in November 2007. Perhaps the applied calibration data set is not correct.

Trend of the Charge Spectra

Before the charge collection distance is analysed, a peculiar feature of the charge spectra is introduced. In Figure 6.38 the MPVs of the Langau-Fits are plotted as a function of the run-number. In contrast to the unirradiated testbeam period the charge collection decreases with operating time for the testbeam configurations after irradiation. This effect can be interpreted by polarisation, see Section 7.2.1.
A quantitative description of the decrease is not possible as the correlation between run-number and real time is marginally documented. Only for July 2008 the real time has been found, see Figure 6.39. Due to the small size of the runs the error bars are significantly larger in July 2008 than for the other testbeam periods. Run-numbers which are not plotted are not available.

(a) October 2006, HV: 400 V.

(b) November 2007, HV: 400 V.

(c) November 2007, HV: 800 V.

(d) July 2008, HV: 800 V.
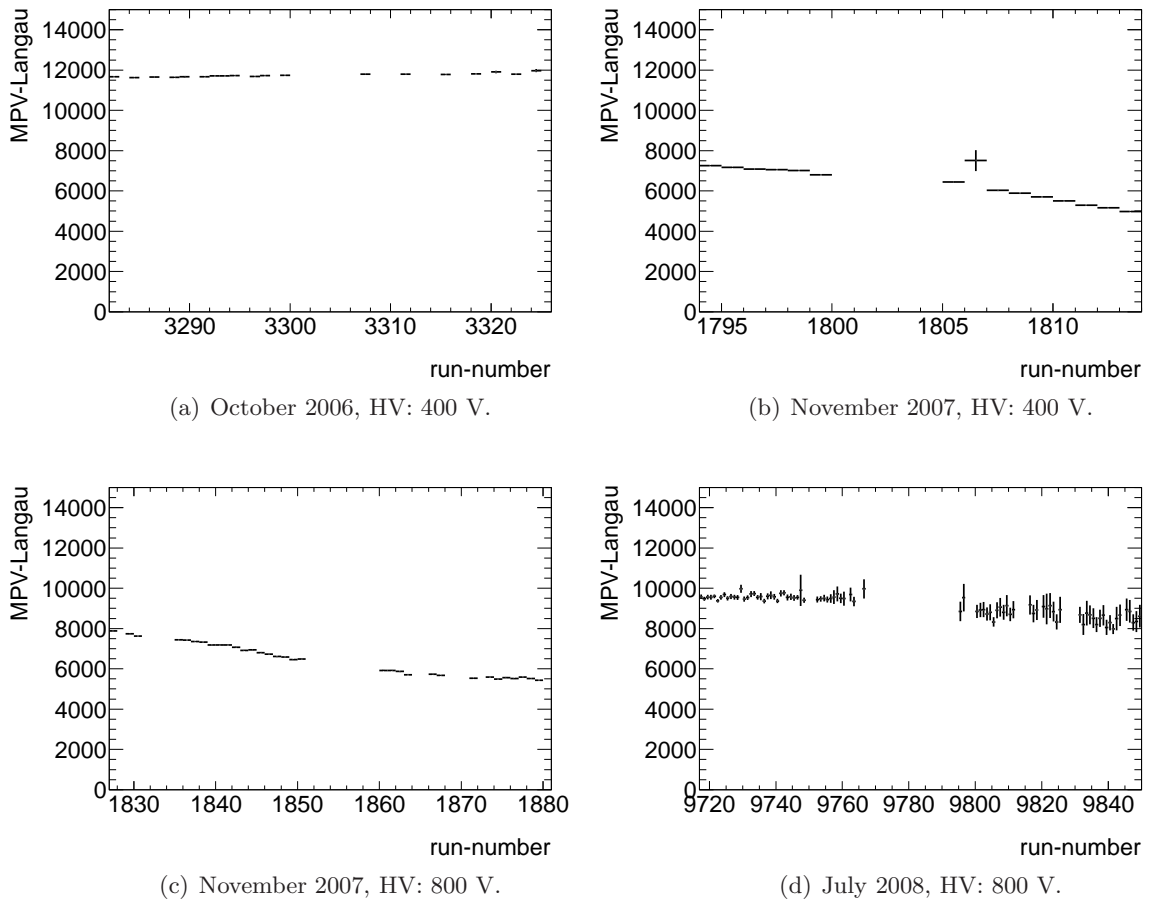
Figure 6.38.: MPV of the Langau-Fit as a function of the run-number for four different test-beam configurations.
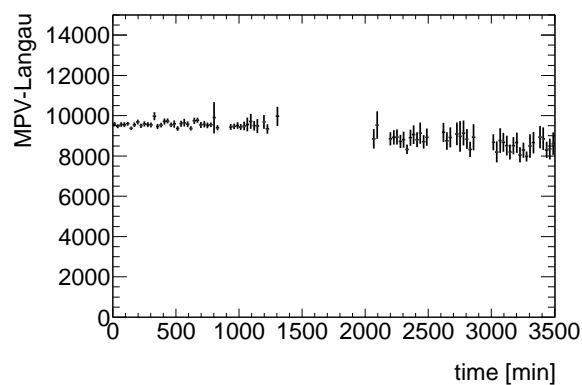
Figure 6.39.: MPV of the Langau-Fit as a function of the operating time for July 2008 at a bias voltage of 800 V.

testbeam period:	charge: [e]		CCD: [μm]	
	mean:	MPV-Langau:	mean:	MPV-Langau:
October 2006, 25 V	8867 ± 43	10689 ± 134	246 ± 10	350 ± 33
October 2006, 50 V	11425 ± 51	11078 ± 80	317 ± 11	363 ± 35
October 2006, 100 V	13670 ± 10	11402 ± 6	379 ± 11	373 ± 36
October 2006, 200 V	13783 ± 17	11508 ± 9	382 ± 11	377 ± 36
October 2006, 300 V	13759 ± 15	11477 ± 8	382 ± 11	376 ± 36
October 2006, 400 V	13856 ± 9	11564 ± 5	384 ± 11	379 ± 36
October 2006, 500 V	13739 ± 32	11486 ± 17	381 ± 11	376 ± 36
August 2007, 400 V	11441 ± 51	9552 ± 36	317 ± 11	313 ± 31
August 2007, 800 V	11340 ± 60	9466 ± 45	315 ± 11	310 ± 30
November 2007, 100 V	2801 ± 18	1766 ± 5	77 ± 8	57 ± 11
November 2007, 400 V	7731 ± 15	6186 ± 12	214 ± 8	202 ± 20
November 2007, 600 V	8610 ± 28	6940 ± 18	239 ± 10	227 ± 24
November 2007, 800 V	8028 ± 10	6433 ± 8	223 ± 10	210 ± 22
November 2007, 1000 V	8543 ± 17	6894 ± 12	237 ± 10	226 ± 24
July 2008, 800 V	10372 ± 16	8557 ± 12	288 ± 11	280 ± 28

Table 6.7.: Charge spectra summary of all testbeam configurations.

6.5.3. CCD and Damage Curve

In Section 3.3.2 the concept of charge collection distance (CCD) has been motivated. CCD can easily be calculated via

$$\text{CCD} = \frac{< Q >_{\text{Mean}}}{q_{\text{MEAN}}} \quad \text{or} \quad \text{CCD} = \frac{< Q >_{\text{MPV}}}{q_{\text{MPV}}} \tag{6.23}$$

where the denominator is the mean (or most probable) number of electron/hole pairs, generated by a minimum ionising particle traversing 1 μm in diamond. In Table 6.7 the characteristic quantities of the charge spectra and the corresponding CCDs are summarised for all testbeam configurations. Excluding the testbeam configurations with unsaturated charge collection, the CCD results - calculated via q_{MEAN} and q_{MPV} - agree within the error bars.
In the first testbeam period the CCD approximately corresponds with the thickness of the sensor (395 μm).
In Figure 6.40 the charge collection distance is plotted as a function of the fluence at a bias voltage of 400 V. The damage curve $\text{CCD} = \frac{\text{CCD}_0}{1+k\phi\text{CCD}_0}$ which has been motivated in Section 3.3.3 is fitted. With a fluence error of 20% a damage coefficient of

$$k = (4.7 \pm 0.6) \times 10^{-18} \text{ cm}^2\mu\text{m}^{-1} \tag{6.24}$$

is determined. The fit and the data poorly match for various reasons: as mentioned above the mapping between the ToT-charge-calibration data sets and the testbeam periods is barely documented. Furthermore the measurement from August 2007 at a fluence of 8.46×10^{13} p cm^{-2} has a particular uncertainty since the complete testbeam setup was of poor quality.
In [45] the damage coefficient is approximately quoted: $k \sim 10^{-18}$ cm$^2\mu$m^{-1}, which is also plotted in Figure 6.40.
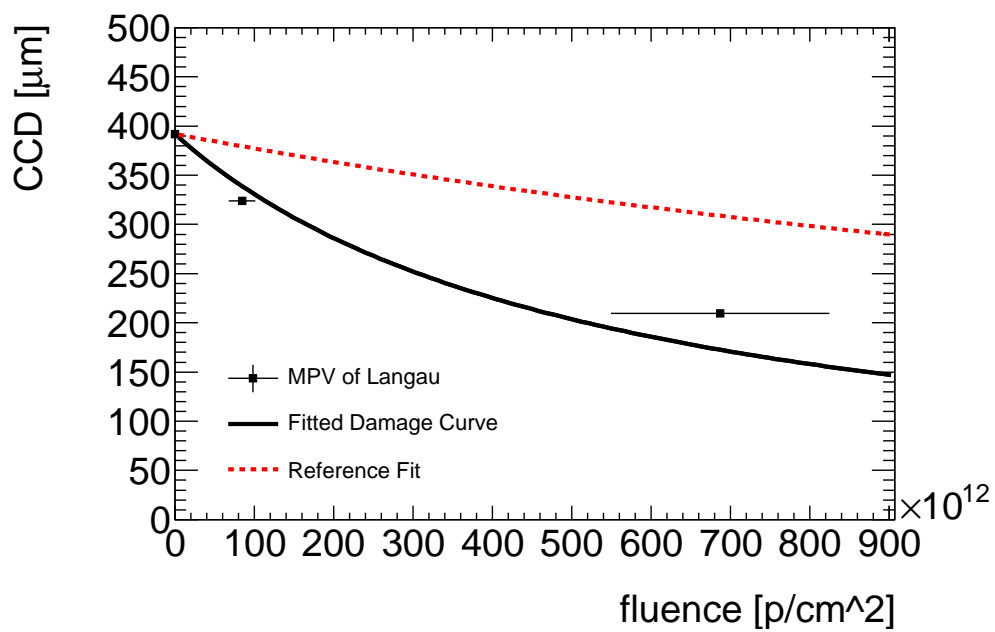
Figure 6.40.: Charge Collection Distance (CCD) and the related damage curve at a bias voltage of 400 V.

7. Summary and Interpretation of the Detector Performance

In this Chapter the detector performance of CD181 is summarised and interpreted. Results of the first testbeam period (without irradiation) are compared with the performance of pCVD diamond and silicon detectors. The testbeam results after irradiation are interpreted in the context of polarisation. In addition, the particular impact of the pixel metallisation is briefly discussed.

7.1. Detector Performance Before Irradiation

Resolution: In Table 7.1 the intrinsic resolution of the short pixel side[1] is compared with the intrinsic resolution of a pCVD diamond and a silicon sensor analysed in [43]. All three detectors operate with the same ATLAS front-end-I3. Focusing on the resolution of all clusters, the

cluster sizes:	CD181:	pCVD: [43]	Si: [43]
all:	12.0 ± 0.1	22.2 ± 0.2	13.6 ± 0.1
1-hit-clusters:	12.3 ± 0.1	18.5 ± 0.2	14.6 ± 0.1
2-hit-clusters:	7.6 ± 0.1	27.5 ± 0.4	4.6 ± 0.1

Table 7.1.: Comparison of the intrinsic resolution between scCVD diamond (σ_{Gauss} of testbeam period October 2006, 400 V), pCVD diamond and silicon.

resolution of scCVD diamond is significantly better than the resolution of pCVD diamond[2] and can compete with silicon.

In comparison to the 2-hit-cluster resolution of silicon, the 2-hit-cluster resolution of scCVD diamond is worse. This effect can probably be explained by charge trapping since the 2-hit-cluster resolution is even worse for pCVD diamonds or irradiated scCVD diamonds.

In [34] an intrinsic resolution of 8.9 ± 0.1 μm is quoted for CD181. This significantly better performance of CD181 is caused by a more precise telescope resolution using a fourth telescope plane and a more complex hit reconstruction: instead of one η-correction for the whole front-end, η-corrections are determined per front-end column. In the same thesis an intrinsic resolution of 23 μm is given for a pCVD module, which is comparable to the results in [43].

Efficiency: In Table 7.2 the detection efficiencies of CD181 and the results for pCVD diamond and silicon from [43] are summarised. Again scCVD diamond performs much better in comparison to pCVD diamond and has similar results as silicon.

---

[1] A telescope resolution of 5.1 μm is quadratically subtracted from the measured resolution, see Section 6.1.1.

[2] The reference data for pCVD diamond [43] was determined in 2001. Due to significant progress in the development of pCVD diamond (especially in terms of CCD) the current pCVD diamond prototypes probably have better resolutions and efficiencies, which have not been published yet.

	CD181:	pCVD: [43]	Si: [43]
detection efficiency:	99.7 ± 0.1	ca. 80	99.8

Table 7.2.: Comparison of detection efficiencies in [%].

CCD: CD181 has a CCD of 380 ± 11 μm at electric fields larger than $0.25V/\mu$m. With a sensor thickness of 395 μm the charge is almost completely collected.

7.2. Detector Performance After Irradiation

For an extensive interpretation of the testbeam results after irradiation the principle of polarisation and the impact of the pixel metallisation are discussed at first.

7.2.1. Polarisation via Local Lattice Defects

In a scCVD diamond homogeneously distributed local lattice defects exist, whose concentration increases with irradiation. These defects can serve as trapping centres, see Section 3.1.2. Consequently they are able to capture free charge carriers and to release them after a certain detrapping time.

If a charged particle crosses the diamond, electron/hole pairs will be produced uniformly along the track. Applying an electric field to the sensor, these charge carriers drift towards the electrodes and are partially trapped by the defects. Due to the opposite drift directions of electrons and holes their particular current densities and therefore also the trapping probabilities are inhomogeneously distributed. For this reason, a positive space charge region is generated in front of the cathode and a negative space charge region in front of the anode. Together they compose an electric field which is reverse to the external electric field. Due to the superposition of these two electric fields, the effective electric field in the bulk region is diminished and the free charge
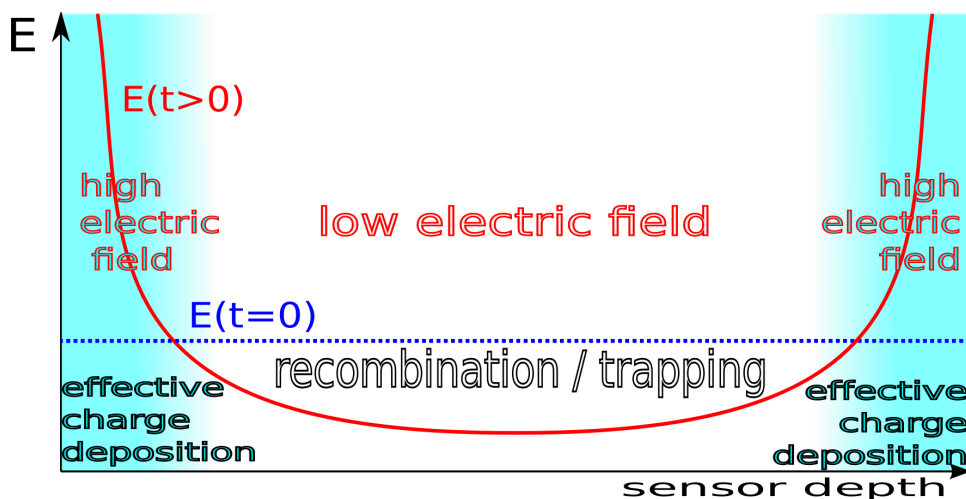
Figure 7.1.: Illustration of polarisation.

carriers basically recombine or are trapped as it is illustrated in Figure 7.1[3]. In the new electric field configuration charge collection occurs primarily by the excess of charge carriers near the electrodes.

The superposition of the external field and the reverse field is called polarisation. In Section 7.2.3 many of the unexpected phenomena, which occur after irradiation, can be understood by polarisation.

7.2.2. Pixel Metallisation

Space charge regions near the electrodes can also be generated by the impact of the pixel metallisation. In these processes the sensor surface is partially corroded.

The metallisation of old tracking detector prototypes (e.g. CD181) has been accomplished at the Ohio State University. The degradation of their pixel metallisation is observed after some operation time (> one year). To industrialise the process of metallisation the new detector prototypes are metallised and bump bonded at IZM[4]. Modifications in this process accelerate the process of degradation.

The impact of the pixel metallisation can only be studied by the complete exchange of the pixel metallisation and the analysis of the detector performance before and after the exchange. It has been discovered that the recovery of an acceptable detector performance is only possible after the mechanical treatment of the sensor surface. A chemical treatment is insufficient since it does not remove the surface defects.

The differences between the two metallisation processes are presently studied. The exact reason for the degradation of the pixel metallisation is not known yet.

7.2.3. Results After Irradiation

Resolution: In general the resolution worsens with larger fluences since the concentration of lattice defects and thus trapping centres increases. In contrast to the unirradiated testbeam period the resolution surprisingly degrades with increasing bias voltage. This effect can be interpreted by polarisation as the central region, which shows a diminished electric field, expands with increasing bias voltage. Simultaneously the trapping probability increases, which causes a broader charge spread and thus a worse resolution.

In addition, the worsening of the resolution with operating time, which only occurs at the irradiated testbeam periods, can be interpreted as a direct consequence of a growing polarisation field, which is saturated after a certain time. This effect is not observed in the unirradiated testbeam period as the impact of polarisation is small.

Cluster Size: Due to the same effect of polarisation, which leads to the degradation of the residuals, the cluster size increases with higher bias voltage. Subsequently the fraction of 1-hit-clusters at a fluence of 6.87×10^{14} p/cm^2 decreases from 31% at 400 V to 18% at 1000 V. This trend is not so distinctive at lower fluences (8.46×10^{13} p/cm^2) as the concentration of lattice defects is smaller.

CCD: Comparing the charge collection before and after irradiation the CCD is reduced by about 44%. After irradiation the CCD is significantly smaller than the sensor thickness. The

---

[3]The plot is motivated by a presentation from S. Schuwalow which was given at the Carat Workshop 2009 in Darmstadt, url: www-norhdia.gsi.de/CARAT01/CARAT01Talks/Schuwalow.pdf (access date: 29.11.2010).

[4]Fraunhofer-Institut für Zuverlässigkeit und Mikrointegration, Berlin

damage coefficient of $k = (4.7 \pm 0.6) \times 10^{-18}$ cm$^2\mu$m^{-1} is comparable with the damage coefficient of about 10^{-18} cm$^2\mu$m^{-1} in [45].

The decreasing CCD with increasing operation time can be interpreted in the same way as the degradation of the resolutions with increasing operation time via polarisation.

Efficiency: Caused by the decreased charge collection and the increase in cluster size the detection efficiency slightly decreases from 99.7% to 98.5% which is acceptable.

Noise: In the first (unirradiated) testbeam period 4% of all events are noisy. This fraction increases in the third testbeam period from 5% at 100 V to 19.4% at 1000 V. At the same time the cluster multiplicity increases with the bias voltage. These dynamics might be caused by an increase of the leakage current. Especially the increase of noise at the edges of the sensor strengthen this hypothesis.

Split-Cluster: The introduction of split-clusters resolves some known inconsistencies:

1. Considering the charge-spectra after irradiation the unexpected peak at low charges can be explained by matched 1-hit-clusters which belong to split-clusters.

2. Abnormal dynamics in cluster sizes as well as in cluster multiplicities can be solved by split-clusters.

Spatial resolution, CCD, and the fraction of split-clusters seem to underly the same dynamics, e.g. the fraction of split-clusters increases and saturates with operating time. This dynamic is caused by polarisation. In this way the hypothesis that split-clusters are caused by trapping is further strengthened.

8. Outlook

Some aspects require further analysis or should be improved in further testbeam studies:

- Testbeam Setup: As discussed in Section 6.1.2 a fourth telescope plane would improve the track reconstruction of the Bonn-ATLAS-Telescope and thus the residual distributions. The desynchronisation problem of the complete testbeam setup should be solved. Separate eta-functions for each readout column or at least for the four different pixel types should be studied. An extension of the alignment-code of EuTelescope would be appreciated; at the moment only shifts in transversal direction as well as a rotation around the z-axis are considered.
  As a first consequence the EUDET telescope, instead of the Bonn-ATLAS-Telescope, has been used in all testbeams since the beginning of 2010. An EuTelescope update is in preparation.

- ToT-calibration: ToT-calibrations should be performed during the testbeam period. All calibration data and further information should be documented in a standardised and understandable way. The study of the leakage current would be interesting especially as a function of operating time. All these aspects are considered in the current testbeam periods.
  The significant deviations between the ToT-calibration curves, accomplished with the two different capacities (C_{low} and C_{high}), have to be understood for a more consistent measurement of the CCD.

- Special Regions: The determined special regions should be analysed in more detail. The metallisation should be checked as well as the sensor surface.

- Polarisation: In this thesis several effects of polarisation have been illustrated. To quantify these effects the variations in the bias voltage are chronologically documented in the current testbeams.
  CCD measurements with a changing electric field ($\sim$10 sec) would be interesting as in this way the CCD can even be enlarged[1].
  To study the impact of recombination and trapping in the bulk region as well as the increased electric field near the electrodes an extensive simulation of polarisation would be helpful.

- Constants: In RD42 it is assumed that on average 36 electron/hole pairs are generated if a MIP traverses 1 μm diamond. It would be interesting to verify this important empiricaly value. To avoid a scaling from the mean to the MPV value it should also be measured for the MPV.

---

[1] This effect is motivated by presentations at the Carat Workshop 2009 at the GSI in Darmstadt,
url: www-norhdia.gsi.de/CARAT01/CARAT01Talks/Schuwalow.pdf (access date: 29.11.2010).

A. Appendix

Testbeam Numbers

testbeam period:	HV: [V]	run-numbers:
October 2006	25	3421
	50	3439, 3440
	100	3182, 3184 - 3186, 3188, 3443, 3447, 3449, 4000 - 4005, 4009 - 4017, 4023
	200	3180, 3190, 3422 - 3424, 3428, 3435, 3437
	300	3179, 3254, 3255, 3257 - 3274, 3276, 3277
	400	3281, 3282, 3284, 3286, 3288 - 3294, 3296, 3297, 3299, 3305, 3307, 3310, 3311, 3315, 3316, 3318, 3320, 3322, 3324, 3326, 3327
	500	3199 - 3203
August 2007	400	275, 282, 286, 510 - 559, 564 - 577, 582 - 589
	800	301 - 313, 325 - 342, 351 - 370, 375 - 378, 381, 383, 385, 386, 388, 390, 392, 393, 395, 397 - 409, 597, 599 - 614, 616, 617, 627 - 656, 658 - 669
November 2007	100	1784, 1789 - 1791
	400	1794 - 1799, 1805 - 1814
	600	1820, 1821, 1824, 1825
	800	1827, 1829, 1830, 1835 - 1850, 1859 - 1863, 1866, 1867, 1871, 1873 - 1879, 1881
	1000	1883, 1888 -1895, 1903, 1904, 1906 - 1908
July 2008	800	9717 - 9767, 9794 - 9796, 9798 - 9811, 9815 - 9818, 9820 - 9825, 9831 - 9843, 9845 - 9850

Table A.1.: Run-numbers of all testbeam periods.

testbeam period:	x-shift: $[mm]$	x-shift: $[mm]$	z-rotation: $[rad]$
October 2006	0.0560 ± 0.0005	-2.2343 ± 0.0008	-0.0014 ± 0.0002
August 2007	3.0343 ± 0.0006	0.0146 ± 0.0011	0.0050 ± 0.0001
November 2007	-2.7991 ± 0.0005	-0.0653 ± 0.0008	-0.0082 ± 0.0002
July 2008	-3.8040 ± 0.0029	-0.0136 ± 0.0030	-0.0078 ± 0.0006

Table A.2.: Alignment constants of the middle telescope plane for all testbeam periods.

testbeam period:	z-position: [mm]			
	BatMod6	BatMod1	BatMod3	DUT
October 2006	0	31.2	267.2	143.2
August 2007	0	41	555	200
November 2007	0	41	513	228
July 2008	0	519	559	412

Table A.3.: Z-positions of the telescope planes and the DUT for all testbeam periods.

Unbiased Y-Residual Distributions of the Irradiated Testbeam Configurations
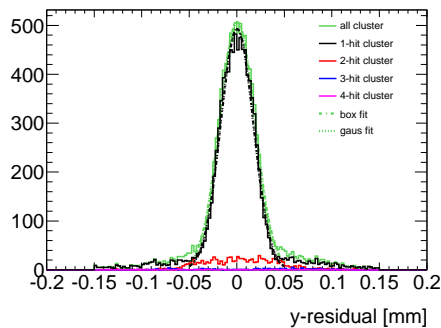
(a) November 2007, 100 V.
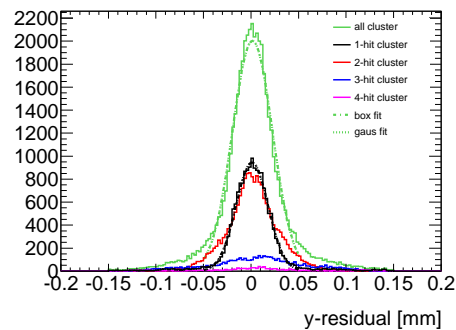
(b) November 2007, 400 V.
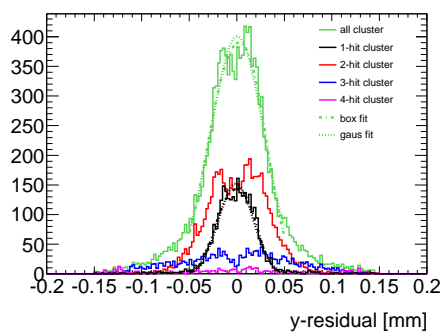
(c) November 2007, 600 V.
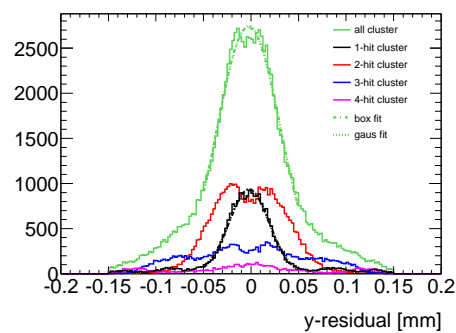
(d) November 2007, 800 V.
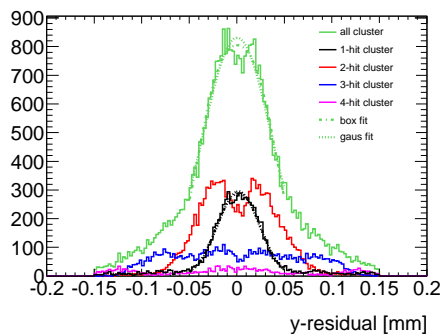
(e) November 2007, 1000 V.
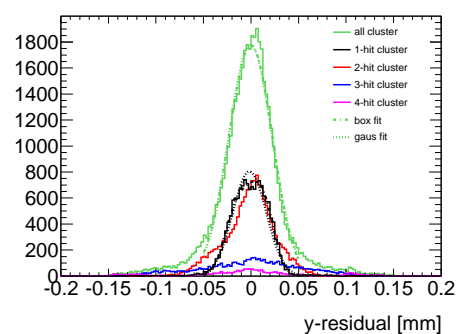
(f) July 2008, 800 V.

Figure A.1.: Unbiased y-residuals of all testbeam configurations in November 2007 and July 2008.

Example of a Box Fit
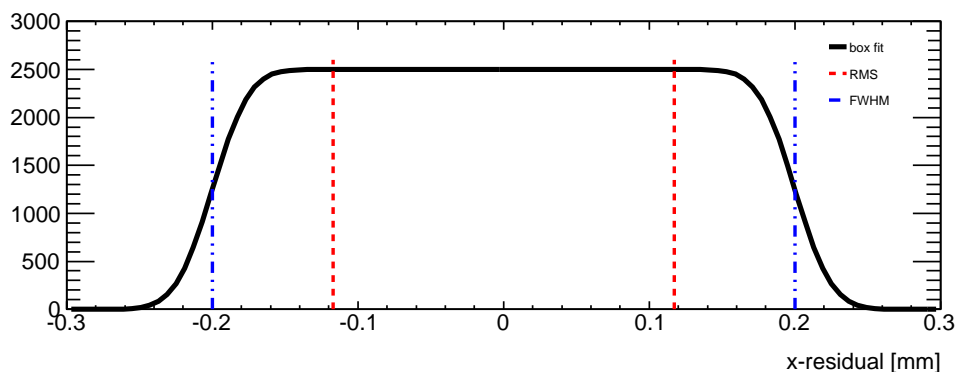
Figure A.2.: Example of a box fit. FWHM and RMS values are indicated by vertical lines.

Efficiency and Noise

testbeam period:	efficiency:
October 2006, 25 V	0.995 ± 0.001
October 2006, 50 V	0.998 ± 0.001
October 2006, 100 V	0.998 ± 0.001
October 2006, 200 V	0.997 ± 0.001
October 2006, 300 V	0.998 ± 0.001
October 2006, 400 V	0.997 ± 0.001
October 2006, 500 V	0.984 ± 0.002
August 2007, 400 V	0.856 ± 0.005
August 2007, 800 V	0.524 ± 0.005
November 2007, 100 V	0.771 ± 0.004
November 2007, 400 V	0.985 ± 0.001
November 2007, 600 V	0.987 ± 0.001
November 2007, 800 V	0.984 ± 0.001
November 2007, 1000 V	0.987 ± 0.001
July 2008, 800 V	0.972 ± 0.001

Table A.4.: Summary of efficiencies for all testbeam configurations.

testbeam period:	noise:
October 2006, 25 V	0.043 ± 0.002
October 2006, 50 V	0.041 ± 0.003
October 2006, 100 V	0.050 ± 0.001
October 2006, 200 V	0.045 ± 0.001
October 2006, 300 V	0.044 ± 0.001
October 2006, 400 V	0.044 ± 0.001
October 2006, 500 V	0.054 ± 0.002
August 2007, 400 V	0.214 ± 0.006
August 2007, 800 V	0.567 ± 0.005
November 2007, 100 V	0.052 ± 0.002
November 2007, 400 V	0.096 ± 0.002
November 2007, 600 V	0.104 ± 0.003
November 2007, 800 V	0.111 ± 0.001
November 2007, 1000 V	0.194 ± 0.002
July 2008, 800 V	0.132 ± 0.002

Table A.5.: Summary of noises for all testbeam configurations.

Bibliography

[1] S. Baranov et al., *Estimation of Radiation Background, Impact on Detectors, Activation and Shielding Optimization in ATLAS*, ATL-GEN-2005-001 (2005).

[2] *Review of Particle Physics (Particle Data Group)*, Journal of Physics G **37** (2010).

[3] S. Glashow, *Partial Symmetries of Weak Interactions*, Nuclear Physics **22** (1961) 579.

[4] S. Weinberg, *A Model of Leptons*, Physical Review Letters **19** (1967) 1264.

[5] A. Salam, *Weak and Electromagnetic Interactions (Elementary Particle Theory)*, edited by: N. Svartholm (Almquist and Wiksell, Stockholm, 1968) (1968) 367.

[6] W. Politzer, *Reliable Perturbative Results for Strong Interactions?*, Physical Review Letters **30** (1973) 1346.

[7] D. J. Gross and F. E. Wilczek, *Ultraviolet Behavior of Non-Abelian Gauge Theories*, Physical Review Letters **30** (1973) 1343.

[8] H. Fritzsch and M. Gell-Mann, *Current algebra: Quarks and what else?*, Proc. of XVI Int. Conf. on High Energy Physics, Chicago, eds. J.D. Jackson and A. Roberts **2** (1972) 135.

[9] P. W. Higgs, *Broken Symmetries and the Masses of Gauge Bosons*, Physical Review Letters **13** (1964) 508.

[10] I. Aitchison, *Supersymmetry in Particle Physics*, Cambridge University Press, 1st edn., (2007), ISBN 978-0-521-88023-7.

[11] S. Weinberg, *Cosmology*, Oxford University Press, 1st edn., (2008), ISBN 978-0-19-852682-7.

[12] *ATLAS Detector and Physics Performance Technical Design Report*, CERN-LHCC-99-014 and CERN-LHCC-99-015 (1999).

[13] *The ATLAS Experiment at the CERN Large Hadron Collider*, Journal of Instrumentation **3** (2008) S08003.

[14] J. Ellis, *Particle Physics at Future Colliders*, ArXiv e-prints (2002), `0210052v1`.

[15] D. Bortoletto, *The ATLAS and CMS Plans for the LHC Luminosity Upgrade*, ArXiv e-prints (2008), `0701199v1`.

[16] M. Capeans et al., *ATLAS Insertable B-Layer Technical Design Report*, CERN-LHCC-2010-013, ATLAS-TDR-019.

[17] P. Hansson et al., *3D Silicon Pixel Sensors: Recent Test Beam Results*, Nuclear Instruments and Methods in Physics Research Section A **321** (2010).

[18] V. Cindro et al., *The ATLAS Beam Conditions Monitor*, Journal of Instrumentation **3** (2008) P02004.

[19] L. Fernandez-Hernando et al., *Development of a CVD diamond Beam Condition Monitor for CMS at the Large Hadron Collider*, Nuclear Instruments and Methods in Physics Research A **552** (2005) 183.

[20] D. Meier, *CVD Diamond Sensors for Particle Detection and Tracking*, Ph.D. thesis, Heidelberg University, (1999).

[21] P. Drude, *Zur Elektronentheorie der Metalle*, Annalen der Physik **1** (1900) 566.

[22] P. Drude, *Zur Elektronentheorie der Metalle. II. Teil*, Annalen der Physik **3** (1900) 369.

[23] E. Borchi et al., *Radiation Damage in Silicon Detectors*, La Rivista del Nuovo Cimento **17** (1994) 1.

[24] J. Grosse-Knetter, *Vertex Measurement at a Hadron Collider - The ATLAS Pixel Detector*, Habilitation, Bonn University, (2007), ISSN-0172-8741.

[25] L. D. Landau, *On the Energy Loss of Fast Particles by Ionization*, Journal of Experimental Physics **8** (1944) 201.

[26] H. Bichsel, *A method to improve tracking and particle identification in TPCs and silicon detectors*, Nuclear Instruments and Methods in Physics Research A **562** (2006) 168.

[27] S. Ramo, *Currents Induced by Electron Motion*, Proceedings of the Institute of Radio Engineers **27** (1939) 584.

[28] V. Radeka, *Low-Noise Techniques in Detectors*, Annual Review of Nuclear and Particle Science **38** (1988) 217.

[29] S. Zhao, *Characterization of the Electronic Properties of Polycrystalline Diamond Films*, Ph.D. thesis, Ohio State University, (1994).

[30] M. Friedl et al., *CVD diamond detectors for ionizing radiation*, Nuclear Instruments and Methods in Physics Research A **435** (1999) 194.

[31] H. Kraner et al., *Fast Neutron Damage In Silicon Detectors*, Nuclear Instruments and Methods in Physics Research A **279** (1989) 266.

[32] W. Adam et al., *Radiation Tolerance of CVD Diamond Detectors for Pions and Protons*, Nuclear Instruments and Methods in Physics Research A **476** (2002) 686.

[33] W. Adam et al., *Pulse height distribution and radiation tolerance of CVD diamond detectors*, Nuclear Instruments and Methods in Physics Research A **447** (2000) 244.

[34] M. Mathes, *Development and Characterization of Diamond and 3D-Silicon Pixel Detectors with ATLAS-Pixel Readout Electronics*, Ph.D. thesis, Bonn University, (2008), ISSN-0172-8741.

[35] H. Liu et al., *Diamond Chemical Vapor Deposition: Nucleation and Early Growth*, Noyes Publication, 1st edn., (1995), ISBN 0-8155-1380-1.

[36] M. Barbero et al., *Development of Diamond Tracking Detectors for High Luminosity Experiments at the LHC*, Status Report RD42, CERN/LHCC 2007-002.

[37] J. Weingarten, *System Test and Noise Performance Studies at the ATLAS Pixel Detector*, Ph.D. thesis, Bonn University, (2007), CERN-THESIS-2008-033.

[38] J. Treis et al., *A modular PC based silicon microstripe beam telescope with high speed data acquisition*, Nuclear Instruments and Methods in Physics Research A **490** (2002) 112.

[39] V. Blobel, *Software alignment for tracking detectors*, Nuclear Instruments and Methods in Physics Research A **566** (2006) 5.

[40] A. Bulgheroni, *Results from EUDET telescope with high resolution planes*, EUDET-Report-2009-02.

[41] R. Lynch et al., *Approximations to multiple Coulomb scattering*, Nuclear Instruments and Methods in Physics Research B **58** (1991) 6.

[42] E. Kobetich et al., *Energy Deposition by Electrons and Delta Rays*, Physical Review **170** (1968) 391.

[43] M. Keil, *Pixeldetektoren aus Silizium und CVD-Diamant zum Teilchennachweis in ATLAS bei LHC*, Ph.D. thesis, Bonn University, (2001).

[44] T. Ullrich et al., *Treatment of Errors in Efficiency Calculations*, ArXiv e-prints (2007), `0701199v1`.

[45] M. Barbero et al., *Development of Diamond Tracking Detectors for High Luminosity Experiments at the LHC*, Status Report RD42, CERN/LHCC 2008-005.

Acknowledgements

In the first place I would like to thank Prof. Dr. Arnulf Quadt who fascinated me for the exciting field of particle physics and gave me the opportunity to participate in several projects at the ATLAS experiment. Special thanks also goes to PD Dr. Jörn Grosse-Knetter the co-corrector of this thesis. I am grateful for their support and their stimulating ideas.

Moreover, I am indebted to Dr. Jens Weingarten who supervised me in the last 12 months. His fundamental knowledge about detector physics and his great efforts in the current testbeam measurements benefit this thesis. Without his support, the thesis would not have been possible.

Many thanks also go to my colleagues of the 2nd Physical Institute, especially to Daniel Schiepel, who helped me in the first months with several computer issues, and Benjamin Schwenker, who supported me in the construction of the interface for EuTelescope. Special thanks also goes to Christian Geisler for the vivid and fruitful discussions; it was a great pleasure to discuss various detector performance issues with him.

Furthermore I would like to thank the testbeam group of the RD42 collaboration, especially members at CERN and Bonn. The participation on a real testbeam was an outstanding highlight of this thesis.

A special thanks goes to Beate Blunck who reviewed this thesis.

Last but not least I would like to thank my parents. Without their reliance and their endless support, these five great years in Göttingen would not have been possible.

Finally, I would like to thank Kristin, as you have supported me so much in the last months. Thank you! :-)